

© 2008 Julio Tomas Barreiro-Guerrero

HYPERENTANGLEMENT FOR QUANTUM INFORMATION

BY

JULIO TOMAS BARREIRO-GUERRERO

Físico, Universidad Nacional Autónoma de México, 2000
M. Sc., University of Illinois at Urbana-Champaign, 2003

DISSERTATION

Submitted in partial fulfillment of the requirements
for the degree of Doctor of Philosophy in Physics
in the Graduate College of the
University of Illinois at Urbana-Champaign, 2008

Urbana, Illinois

Doctoral Committee:

Professor Paul M. Goldbart, Chair
Professor Paul G. Kwiat, Adviser
Assistant Professor Nadya Mason
Professor Munir Nayfeh

Abstract

Entanglement, the most intriguing implication of quantum theory, embodies the most perfect correlations possible between two quantum systems. It underlies many important applications in quantum information processing, including quantum computing, quantum cryptography, dense coding, and teleportation. The power of these protocols is further enhanced with higher-order entanglement, realized in multi-particle and multi-dimensional systems. This thesis investigates the production and applications of pairs of photons simultaneously entangled in *every* degree of freedom, so-called “hyperentangled”.

Using pairs of photons produced in spontaneous parametric down-conversion, we produce hyperentanglement and verify it by observing a Bell-type inequality violation in each degree of freedom: polarization, spatial mode, and emission time. We produce and characterize maximally hyperentangled states and novel states simultaneously exhibiting both quantum and classical correlations. We also report the tomography of a 2x2x3x3 system, which was the largest photonic entangled system to be so characterized at the time it was reported.

Using hyperentanglement in spin (polarization) and orbital angular momentum as well as single-photon spin-orbit Bell-state analyzers, we demonstrate two quantum protocols. First, we demonstrate a dense-coding experiment with the largest reported channel capacity (1.630(6) bits), which breaks the conventional linear-optics threshold. In addition, we investigate optimal schemes for the discrimination of hyperentangled Bell states. Second, we remotely prepare and tomographically characterize single-photon two-qubit states, including spin-orbit entangled states, radially polarized, and mixed states.

Finally, we explore experimental schemes to create two novel states, “bound-entangled” and CGLMP states. The former are mixed states from which pure entanglement cannot be distilled; in particular, we consider the Smolin state, which is a mixture of hyperentangled states. The latter states present the puzzling property of violating a Bell-type inequality more strongly than would any maximally hyperentangled state.

To Mom and Dad.

Acknowledgments

This work was supported by Fulbright, CONACyT Mexico, Shirley Jones and Mavis Memorial Fellowships, the DTO/ARO-sponsored MURI Center for Photonic Quantum Information Systems, the DTO/IARPA-sponsored Advanced Quantum Communication grant, and the ADNI/S&T-IARPA. Thanks to my parents, Julieta and Tomas, my sister, Aline, my soulmate, Elizabeth Villa, a special teacher, Elisa Viso, and my adviser Paul Kwiat.

Table of Contents

List of Tables	vii
List of Figures	viii
List of Abbreviations	x
Chapter 1 Introduction	1
1.1 Spontaneous parametric down-conversion	2
1.2 Polarization entanglement	4
1.3 Spatial mode entanglement	5
1.4 Energy-time entanglement	5
1.5 Overview: Hyperentanglement for Quantum Information	6
Chapter 2 Hyperentanglement	8
2.1 Experimental setup	9
2.2 State characterization	10
2.3 Bell-inequality test in every DOF	11
2.4 Quantum state tomography of hyperentangled states	12
Chapter 3 Hyperentanglement-assisted dense coding	17
3.1 Theory	19
3.2 Experiment	20
3.2.1 Experimental details	21
3.3 Results	23
3.4 Conclusions	25
Chapter 4 Hyperentangled Bell-state analysis	27
4.1 Kwiat-Weinfurter scheme for Bell-state analysis	28
4.2 Optimal hyperentangled Bell-state analysis	29
4.2.1 Proof of optimality	29
4.2.2 Unambiguous Bell-state discrimination?	31
4.2.3 More degrees of freedom	32
4.3 Implications for quantum communication	33
4.3.1 Superdense coding	33
4.3.2 Quantum teleportation	33
4.3.3 Quantum fingerprinting	34
4.4 Concluding remarks	35
Chapter 5 Remote Entangled State Preparation	36
5.1 Remote state preparation	36
5.2 Remote entangled-state preparation	38
5.3 Remote preparation of arbitrary single-photon spin-orbit states	39
5.3.1 A 4-parameter family of spin-orbit Bell-states	40
5.3.2 Remote preparation of two-qubit mixed states	45

Chapter 6	Outlook	47
6.1	Bound entanglement	47
6.2	CGLPM Inequality for $d = 4$ with Hyperentanglement	51
6.2.1	Four-outcome measurement scheme	53
6.2.2	Two-outcome measurement scheme	54
Appendix A	Holograms	57
A.1	Chemicals	57
A.1.1	For your chemical safety	57
A.1.2	Mixing the stock solutions	58
A.2	Exposing the hologram	59
A.3	Developing the hologram	60
A.3.1	Preparation	60
A.3.2	Processing procedures	61
Appendix B	Beam pointing stabilization	63
B.1	Feedback circuit	65
Appendix C	Hyperentanglement-assisted dense coding: Supplementary information	67
C.1	Channel capacity as a function of conditional detection average success probability	67
C.2	Effect of experimental imperfections on the channel capacity	68
C.2.1	Modeling imperfections: The input states	68
C.2.2	Modeling imperfections: The spin-orbit gate	69
C.2.3	Estimating the channel capacity	69
C.2.4	Results	70
Appendix D	Spin-orbit entangling gate	72
Appendix E	Quantum state tomography for multidimensional and multiparticle quantum systems	74
E.1	Linear reconstruction	74
E.2	MATLAB code to generate the traceless Hermitian basis of the special unitary group $SU(d)$	75
References		77
Author's Biography		84

List of Tables

2.1	Bell parameter S showing CHSH-Bell inequality violations in every degree of freedom.	13
4.1	Detection signature table for the Kwiat-Weinfurter embedded BSA scheme.	29
4.2	Detection signature for the modified KW scheme.	31
5.1	Visibility for remotely prepared entangled states.	39
5.2	Two-qubit remotely prepared states as a function of Bob's parameters.	42
C.1	Effect of experimental imperfections on the CC	70

List of Figures

1.1	Two-crystal scheme to create polarization entanglement.	4
1.2	Laguerre-Gauss beams as qudits for quantum information processing.	6
2.1	Experimental setup for the creation and analysis of hyperentangled photons.	9
2.2	Basis for the reconstruction of spatial modes.	10
2.3	Experimental setup for the analysis of time-energy entangled states.	11
2.4	Measured density matrix of a $2 \times 2 \times 3 \times 3$ -dimensional state of two photons.	14
2.5	Measured density matrices (real parts) of $2 \times 2 \times 2 \times 2$ -dimensional states of two photons.	15
3.1	Original quantum dense coding scheme.	18
3.2	Spin-orbit Bell-state Analyzer.	21
3.3	Experimental setup for dense coding with spin-orbit encoded photons.	22
3.4	Experimental results of hyperentanglement-assisted dense coding.	23
3.5	Conditional detection probabilities beating the CC limit for standard dense-coding with linear optics.	24
3.6	Experimentally reported CCs as a function of their conditional detection average success probability.	25
4.1	Kwiat-Weinfurter scheme for the embedded Bell-state analysis.	29
4.2	Modified KW scheme.	31
5.1	Basic quantum communication protocols: Dense coding, teleportation, remote state preparation, and remote entangled-state preparation.	36
5.2	Remotely prepared states on the Poincaré sphere.	37
5.3	Experimental density matrices of remotely prepared entangled states.	39
5.4	Spin-orbit transverse polarization profiles.	43
5.5	Experimental density matrices and transverse polarization profile of remotely prepared “radial-polarization” states.	44
5.6	Experimental density matrices of remotely prepared two-qubit mixed states.	46
6.1	Distillation and formation of entanglement as complementary processes.	47
6.2	Experimental setup to produce and characterize bound entangled states.	50
6.3	Four-outcome measurement scheme for testing a CGLPM-inequality.	54
6.4	Two-outcome measurement scheme for testing a CGLPM-inequality.	54
6.5	CGLPM-parameter (I_4) contours in the plane of state quality and measurement precision.	56
A.1	Hologram processing chain with the JD-2 developer.	61
B.1	Schematic of laser beam pointing control device.	64
B.2	Scopes traces showing the effect of beam pointing stabilization.	64
B.3	Eagle schematic for the pointing stabilization circuit.	66

C.1 Experimentally achieved and simulated CCs as a function of conditional detection average success probability.	71
D.1 Spin-orbit entangling gate and measured intensity profiles.	73

List of Abbreviations

BBO	β -barium borate.
BE	Bound entangled.
BS	Beam splitter.
BSA	Bell-state analysis.
CC	Channel capacity.
CHSH	Clauser-Horne-Shimony-Holt.
CGLMP	Collins-Gisin-Linden-Massar-Popescu.
CNOT	Controlled-NOT.
DC	Direct Current.
DOF	Degree of freedom.
F	Fidelity.
GND	Ground.
HBSA	Hyperentangled Bell-state analysis.
HG	Hermite-Gauss.
HWP	Half-wave plate.
LC	Liquid crystal.
LG	Laguerre-Gauss.
OA	Optic axis.
OAM	Orbital angular momentum.
PBS	Polarizing beamsplitter.
PI	Proportional-Integral.
POVM	Positive Operator-Valued Measure.
RESP	Remote entangled-state preparation.
RSP	Remote state preparation.
QIP	Quantum information processing.

QWP	Quarter-wave plate.
S_L	Linear entropy.
SNR	Signal-to-noise ratio.
SPDC	Spontaneous parametric down-conversion.
T	Tangle.

Chapter 1

Introduction

Recent interest in the fundamentals and applications of quantum mechanics has given rise to the field of quantum information, which utilizes various quantum mechanical phenomena to enable tasks difficult or impossible with classical systems, e.g., provably secure encryption [1, 2], Shor’s factoring algorithm [3] and Grover’s search algorithm [4, 5]. One such quantum resource is entanglement, the peculiar non-classical correlations that are possible between separated quantum systems. It is potentially a physical resource that, like energy, can be measured and transformed.

In standard quantum computation, where sequences of unitary quantum logic gates process qubits, entanglement is not required as an *initial* resource, because it can be generated. Nonetheless, the promising model of one-way quantum computing, recently proposed [6] and realized [7], requires qubits to be initialized in a highly entangled “cluster” state. Quantum communication applications, including teleportation, superdense coding and secure cryptography, benefit from multi-particle and multi-dimensional entanglement as well.

Entangled states, with many particles and dimensions, have been generated in a number of physical systems, including, spins in diamond [8], superconductors [9], ions [10], atomic ensembles [11], and photons [12]. However, the photon is the quintessential information carrier for quantum communication and a promising contender as a resource for the ultimate goal of a large-scale quantum computer. Several physical processes have been proposed as sources of pairs of entangled photons: e.g., quantum dots [13], atoms [14], and ions [15] (the last two have thus far only achieved interference between single photons). Particularly successful, however, is the nonlinear optical process of spontaneous parametric down-conversion (SPDC), which has enabled the entanglement of up to 6 photons [16].

Photon pairs produced via SPDC also have many accessible degrees of freedom (DOFs) that can be used to carry entanglement. This was first demonstrated using polarization [17, 18], but the list expanded rapidly to include momentum (linear [19], orbital [20], and transverse [21] spatial modes), energy-time [22] and time-bin [23], simultaneous polarization and energy-time [24], and

recently, simultaneous polarization and linear momentum entanglement [25, 26]. In our work, we produce and characterize pairs of single photons that are “hyperentangled” [27, 28]—simultaneously entangled in *every* DOF: polarization, spatial mode, and energy-time. An immediate advantage of hyperentanglement is a larger Hilbert space for quantum information processing (QIP).

Moreover, encoding qubits in different DOF facilitates the implementation of qubit-qubit interactions, such as the CNOT gate [29], which otherwise can only be carried out probabilistically. Performing such gates with 100% efficiency is impossible using only a single DOF with linear optics; thus, hyperentanglement enables the realization of novel quantum protocols. For example, the primary gate for quantum communication, complete Bell-state analysis (BSA), is possible with 100% efficiency. Such BSA enables, for example, full dense coding in one degree of freedom and an even higher channel capacity by encoding in multiple degrees of freedom. In addition to quantum communication benefits from hyperentanglement, one-way quantum computation has been demonstrated as well [30, 31].

Hyperentanglement can also deepen our understanding of fundamental aspects of quantum phenomena. For example, an all-versus-nothing non-locality test was performed with hyperentanglement recently [25, 26]. Other more provocative examples involve the creation of exceptional states, e.g., “bound entangled” states (entangled mixed states from which no pure entanglement is distillable) and surprising “CGLMP-Bell states” (nonmaximally entangled states that can violate a suitable Bell’s inequality more than any maximally entangled state).

Both practical and fundamental aspects of hyperentanglement will be explored in this thesis. To start, the following sections will briefly describe the nonlinear process of spontaneous parametric down-conversion and how entanglement arises in each degree of freedom. The last section of this chapter will give an overview of the rest of the thesis.

1.1 Spontaneous parametric down-conversion

Pairs of entangled photons can be generated through the nonlinear process of spontaneous parametric down-conversion. In nonlinear optical processes, an intense optical field applied to a nonlinear material induces polarization components $P_j(t)$ with a power-series response to the field strength

components $E_m(t)$ [32]:

$$\begin{aligned} P_j(t) &= \chi_{jk}^{(1)} E_k(t) + \chi_{jkl}^{(2)} E_k(t) E_l(t) + \dots \\ &\equiv P_j^{(1)}(t) + P_j^{(2)}(t) + \dots , \end{aligned}$$

where the constants of proportionality $\chi^{(n)}$ are the n th-order optical susceptibilities. The time-varying polarization acts as a source of new components of the electromagnetic field.

As an example, spontaneous parametric down-conversion [33] results from the second-order nonlinear polarization $P_j^{(2)}(t)$. In this process, a pump photon with frequency ω_p interacts with a nonlinear crystal to generate a pair of daughter photons (labeled “signal” and “idler”) with frequencies ω_s and ω_i , prescribed by energy conservation:

$$\hbar\omega_p = \hbar\omega_s + \hbar\omega_i .$$

Similarly, momentum conservation inside the crystal prescribes the phase-matching condition:

$$\mathbf{k}_p = \mathbf{k}_s + \mathbf{k}_i ,$$

where \mathbf{k} are the in-crystal wave vectors corresponding to the waves with frequencies ω and refractive index $n(\omega)$ ($\omega = \omega_s, \omega_i, \omega_p$): $|\mathbf{k}| = k = \omega n(\omega)/c$. Quantum mechanically, the process (which we consider to be very weak) may be described by the Hamiltonian:

$$\begin{aligned} \mathcal{H} &= A \int_V d^3r \chi^{(2)} E_p^{(+)} E_s^{(-)} E_i^{(-)} + \text{H.c.} \\ &= A \int_V d^3r \chi^{(2)} \mathbf{E}_0 e^{i(\mathbf{k}_p \cdot \mathbf{r} - \omega_p t)} \sum_{\mathbf{s}} E_{\mathbf{s}} a_{\mathbf{s}}^\dagger e^{i(\mathbf{k}_s \cdot \mathbf{r} - \omega_s t)} \sum_{\mathbf{i}} E_{\mathbf{i}} a_{\mathbf{i}}^\dagger e^{i(\mathbf{k}_i \cdot \mathbf{r} - \omega_i t)} + \text{H.c.}, \end{aligned}$$

where the integral is taken over the interaction volume V , the index \mathbf{s} (\mathbf{i}) runs over polarization λ_s (λ_i) and momentum \mathbf{k}_s (\mathbf{k}_i), and we treat the pump field classically. Every DOF of the photon becomes explicit in the last expression: polarization (λ), momentum (\mathbf{k}) and energy ($\hbar\omega$). Next we discuss the production of entanglement in each DOF.

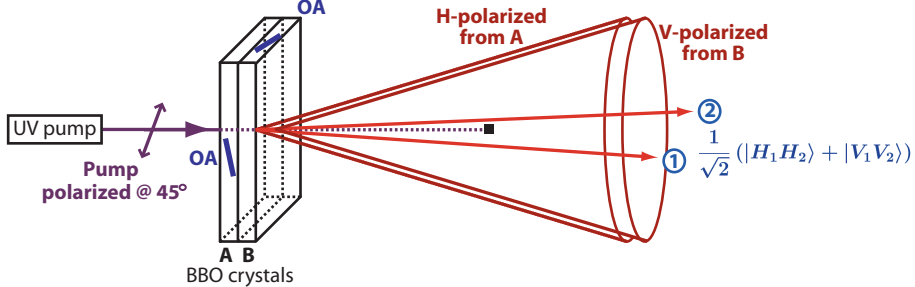


Figure 1.1: Two-crystal scheme to create polarization entanglement. The two BBO (β -barium borate) crystals A and B have their optic axes oriented as shown. By pumping the crystals with light polarized at 45° , we generate a superposition of horizontally and vertically polarized photons in approximately the maximally entangled state $\frac{1}{\sqrt{2}}(|HH\rangle + |VV\rangle)$.

1.2 Polarization entanglement

In type-I phase matching, a pump photon polarized in the plane defined by its propagation direction and the crystal optic axis (e.g., horizontal) generates a pair of photons polarized in the perpendicular plane (vertical) (see Fig. 1.1). By symmetry, the photons are emitted in a cone centered around the pump propagation direction; from transverse momentum conservation, the photons must be emitted on opposite sides of the cone. Now, consider *two* contiguous thin crystals with their optic axes aligned in perpendicular planes, pumped by photons polarized at an angle θ_p with respect to the laboratory (horizontal). The down-conversion processes in each crystal are coherent with one another, provided the spatial modes emitted from each crystal overlap. From a simple argument based on the divergence of the daughter photons, the spatial overlap will be high if $D/L \gg \theta_{dc}$, with cone opening angle θ_{dc} , crystal thickness L , and pump beam diameter D . This constraint can be satisfied by using a combination of thin crystals and beam waists that are “large” relative to the mismatch in the overlap of the down-conversion cones from each crystal [34]. Consequently, the photons will automatically be generated in an arbitrary superposition of horizontally (H) and vertically (V) polarized pairs [34]:

$$\cos \theta_p |H_1 H_2\rangle + e^{i\gamma} \sin \theta_p |V_1 V_2\rangle,$$

where θ_p is the pump linear polarization angle, and γ is the phase between the photons emitted in different crystals.

1.3 Spatial mode entanglement

A complete basis for describing the paraxial propagation of light is provided by the Gaussian spatial mode families, Hermite-Gauss (HG_{rs}) and Laguerre-Gauss (LG_{pl}). In the case of SPDC, the daughter photons were shown to be entangled in either basis [20, 35, 36]. Laguerre-Gauss beams, however, can be used naturally as qudits, where the amount of their orbital angular momentum (OAM) encodes a d-level quantum system, or qudit (see Fig. 1.2). Since LG_{pl} modes carry $l\hbar$ OAM, the entanglement in SPDC results evidently from conservation of OAM. Explicitly, a down-conversion source generates a biphoton state described by:

$$\sum_{l_1, p_1} \sum_{l_2, p_2} C_{p_1, p_2}^{l_1, l_2} |l_1, p_1; l_2, p_2\rangle,$$

where l_1, p_1 (l_2, p_2) corresponds to the mode of photon 1 (2) [37]. The probability amplitudes $C_{p_1, p_2}^{l_1, l_2}$ depend only on the radial profile of the $(l_1 + l_2)$ -th angular harmonic of the pump beam. For a gaussian 0-th OAM pump beam, the significant contributions come from the low-order OAM daughter photons [38]: including only the 0th and 1st orders, the state is

$$\frac{1}{\sqrt{2 + |\alpha|^2}} (|r_1 l_2\rangle + \alpha |g_1 g_2\rangle + |l_1 r_2\rangle),$$

where $|l\rangle$, $|g\rangle$ and $|r\rangle$ represent the paraxial spatial modes (Laguerre-Gauss) carrying $-\hbar$, 0, and $+\hbar$ OAM, respectively [39]; α describes the balance of amplitudes of the OAM spatial mode states prescribed by the source [40] and selected via the mode-matching conditions. The OAM entanglement is maximized by balancing the relative populations of the low-valued OAM-eigenstates [38], which requires focusing the pump beam to smaller beam waists at the crystal and imaging a large area of the down-conversion cones.

1.4 Energy-time entanglement

In down-conversion, due to the many ways to partition the energy of the parent photon, each daughter photon has a broad spectrum. However, for a continuous-wave pump, the pump energy E_p is well defined, and hence the *sum* of the daughter photons' energies is also well defined. Therefore, each pair of photons is entangled in energy. Equivalently, each pair is coherently emitted over a range of times within the coherence time of the pump, but the *difference* in emission times can be

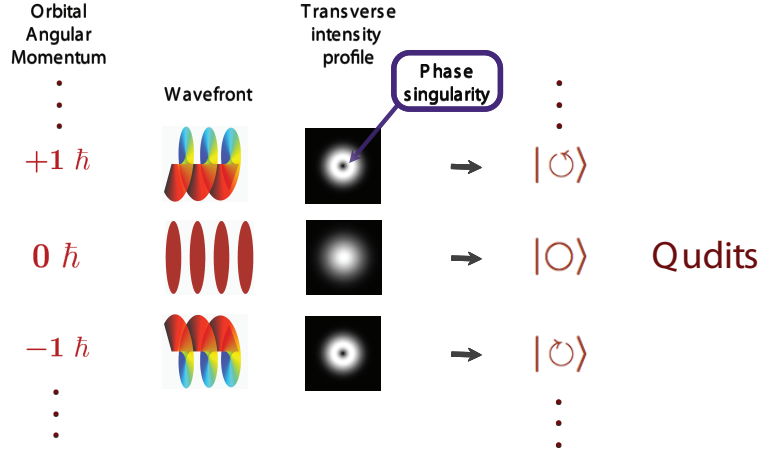


Figure 1.2: Laguerre-Gauss beams as qudits for QIP. The set of Laguerre-Gauss beams $\text{LG}_{0,p}$ carrying $\pm p\hbar$ OAM (shown here are the $0\hbar$ - and $\pm 1\hbar$ -OAM beams) have a characteristic helical wavefront. At the propagation axis, the phase has a phase singularity and the intensity is zero. Any subset of $\text{LG}_{0,p}$ can be used to encode qudits.

very small (hundreds of femtoseconds). This correlation is represented by the state:

$$\int_0^{E_p} dE A(E) |E\rangle_1 |E_p - E\rangle_2 \sim \int dt |t\rangle_1 |t\rangle_2,$$

where $A(E)$ is the spectral distribution of the collected down-conversion light. Two-time entanglement can be verified through interferometric schemes [22] in which the postselected state is

$$\frac{1}{2} (|s_1 s_2\rangle + |f_1 f_2\rangle),$$

where the slow (s) and fast (f) labels, respectively, represent the relative early and late emission times of a pair of energy anticorrelated photons [22]. Similar energy-time entangled states can be prepared by sending a pulsed pump through imbalanced interferometers, giving rise to entanglement in time bins [23].

1.5 Overview: Hyperentanglement for Quantum Information

This dissertation will describe how hyperentanglement is created and manipulated for QIP. The next chapter will describe our source of hyperentangled photons and its characterization. The remaining chapters will describe applications for QIP, encoding the qubits primarily in the polarization and

OAM DOF of the photons.

Using hyperentanglement, we enhanced a number of protocols for QIP, starting with dense coding, the first quantum communication protocol proposed. Chapter 3 describes how hyperentanglement enabled us to beat a fundamental limit on the channel capacity of the conventional dense-coding scheme. By further manipulating the polarization and spin-orbit control-gate, we can remotely prepare single-photon entangled and radial polarization states; preliminary efforts will be described in chapter 4.

In chapter 5, we will discuss the characterization of quantum “black-boxes”, or quantum process tomography. Again, full BSA will enable the reconstruction of quantum processes with fewer measurements, a technique known as Direct Characterization of Quantum Dynamics (DCQD). In particular, we will discuss our current efforts to characterize 1-qubit processes. In this case, DCQD requires only 4 measurements while the standard scheme needs 16.

Finally, in chapter 6, preliminary studies of further applications will be discussed, including the generation of bound-entangled states and CGLPM states. The experiments involve a significant effort of automated control and precision alignment to achieve high-quality states and protocols. These and other details are described in a number of appendices included at the end of the thesis.

Chapter 2

Hyperentanglement

Reproduced in part with permission from J. T. Barreiro, N. K. Langford, N. A. Peters, and P. G. Kwiat. Generation of Hyperentangled Photon Pairs. *Phys. Rev. Lett.* **95**, 260501 (2005). Copyright 2005 American Physical Society, U.S.A.

In this chapter, we describe the production and characterization of pairs of single photons simultaneously entangled in *every* DOF [28] –polarization, spatial mode and energy-time. As reported by Mair et al. [20], photon pairs from a *single* nonlinear crystal are entangled in OAM. Moreover, polarization entangled states can be created by coherently pumping *two* contiguous thin crystals [34], provided the spatial modes emitted from each crystal are indistinguishable. Finally, the pump distributes energy to the daughter photons in many ways, entangling each pair in energy; equivalently, each pair is coherently emitted over a range of times (within the coherence of the continuous wave pump). We showed that our two-crystal source can generate a $2 \times 2 \times 3 \times 3 \times 2 \times 2$ -dimensional hyperentangled state¹ [28], approximately

$$\underbrace{(|HH\rangle + |VV\rangle)}_{\text{polarization}} \otimes \underbrace{(|rl\rangle + \alpha|gg\rangle + |lr\rangle)}_{\text{spatial modes}} \otimes \underbrace{(|ss\rangle + |ff\rangle)}_{\text{energy-time}}. \quad (2.1)$$

The most common maximally entangled states are the 2-qubit Bell states: $\Phi^\pm = (|00\rangle \pm |11\rangle)/\sqrt{2}$ and $\Psi^\pm = (|01\rangle \pm |10\rangle)/\sqrt{2}$, in the logical basis $|0\rangle$ and $|1\rangle$. By collecting only the $\pm \hbar$ OAM state of the spatial subspace, the state (2.1) becomes a tensor product of three Bell states $\Phi_{\text{poln}}^+ \otimes \Phi_{\text{spa}}^+ \otimes \Phi_{\text{t-e}}^+$.

As a preliminary test of the hyperentanglement, we characterized the polarization and spatial mode

¹In addition, we note that the pairwise mechanism of the $\chi^{(2)}$ -down-conversion process inherently produces entanglement in photon number [41], according to:

$$|\Psi_{\text{down-conversion}}\rangle = |00\rangle + \epsilon|11\rangle + \epsilon^2|22\rangle + \dots,$$

where $|nn\rangle$ is the creation of n photons in each of two different modes. The parameter ϵ is determined by the effective nonlinearity, the crystal length and the pump laser intensity. For our continuous wave pump, ϵ is very small, and we postselect the $|11\rangle$ term by detecting one photon in each of two detectors.

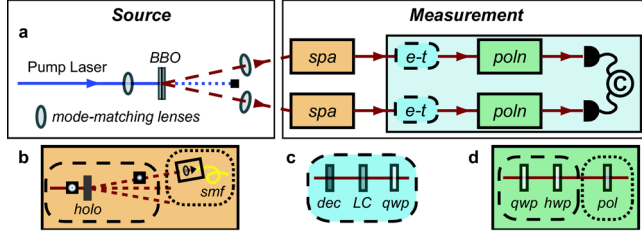


Figure 2.1: Experimental setup for the creation and analysis of hyperentangled photons. (a) The photons, produced using adjacent nonlinear crystals (BBO), pass through a state filtration process for each DOF before coincidence detection. The measurement insets show the filtration processes as a transformation of the target state (dashed box) and a filtering step to discard the other components of the state (dotted box). (b) *Spatial Filtration (spa)*: hologram (holo) and single-mode fiber (smf). (c) *Energy-Time Transformation (e-t)*: thick quartz decoherer (dec) and liquid crystal (LC). (d) *Polarization Filtration (poln)*: quarter-wave plate (qwp), half-wave plate (hwp) and polarizer (pol).

subspaces by measuring the entanglement (characterized by tangle T^2), the mixture (characterized by linear entropy $S_L(\rho) = \frac{4}{3}[1 - \text{Tr}(\rho^2)]$ [43]), and the fidelity $F(\rho, \rho_t) \equiv (\text{Tr}(\sqrt{\sqrt{\rho_t}\rho\sqrt{\rho_t}}))^2$ of the measured state ρ with the target state $\rho_t = |\psi_t\rangle\langle\psi_t|$. We consistently measured high-quality states with tangle, linear entropy, and fidelity with Φ^+ of $T = 0.99(1)$, $S_L = 0.01(1)$ and $F = 0.99(1)$ for polarization; and $T = 0.96(1)$, $S_L = 0.03(1)$ and $F = 0.95(1)$ for spatial mode, significantly higher than earlier results [21].

2.1 Experimental setup

The experiment is illustrated in Fig. 2.1. A 120-mW 351-nm continuous-wave Ar⁺ laser pumps two contiguous β -barium borate (BBO) nonlinear crystals with optic axes aligned in perpendicular planes [34]. Each 0.6-mm thick crystal is phasematched to produce Type-I degenerate photons at 702 nm into a cone of 3.0° half-opening angle. The first (second) crystal produce pairs of horizontally (vertically) polarized photons and these two possible down-conversion processes are coherent, provided the spatial modes emitted from each crystal are indistinguishable. With the pump focused to a waist of $\sim 90 \mu\text{m}$ at the crystals, this constraint can be satisfied by using thin crystals and “large” beam waists (large relative to the mismatch in the overlap of the down-conversion cones from each crystal [34]). Mode-matching lenses were used to optimize the coupling of the rapidly diverging down-conversion modes into single-mode collection fibers.

²The tangle of the state ρ is

$$T(\rho) = [\max 0, \lambda_1 - \lambda_2 - \lambda_3 - \lambda_4]^2,$$

where the λ_i 's are the square roots of the eigenvalues of $\rho(\sigma_2 \otimes \sigma_2)\rho^*(\sigma_2 \otimes \sigma_2)$, in non-increasing order by magnitude, with $\sigma_2 = \begin{pmatrix} 0 & -i \\ i & 0 \end{pmatrix}$. The tangle ranges from 0 for an unentangled state (e.g., $|HH\rangle$), to 1 for a maximally entangled state (e.g., Φ^+) [42].

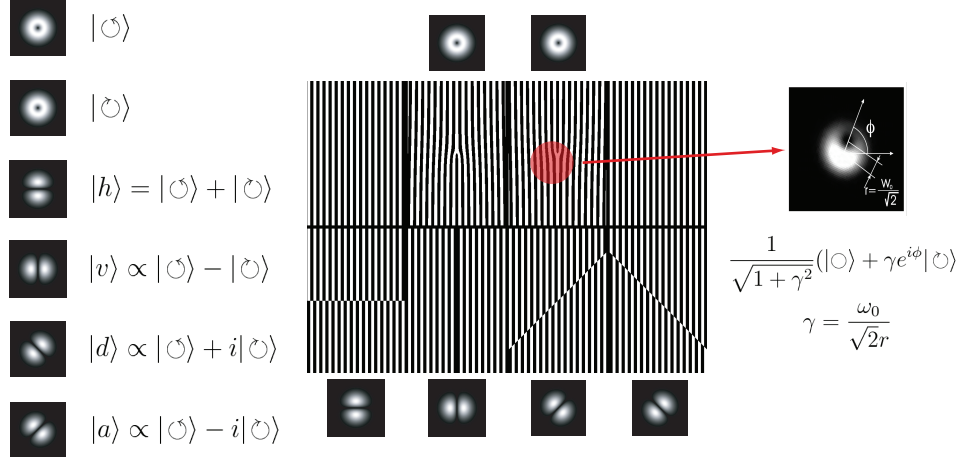


Figure 2.2: Basis for the reconstruction of spatial modes. Left: Overcomplete basis for the reconstruction of $\pm \hbar$ -OAM states with $|\odot\rangle = |l\rangle$, $|\circlearrowleft\rangle = |r\rangle$, and $|\circlearrowright\rangle = |g\rangle$. Center: Binary plane-wave gratings [39] ($\sim 40\%$ diffraction efficiency) project the states shown. Right: By displacing the holograms for $|\odot\rangle$ ($|\circlearrowleft\rangle$) we can project arbitrary linear combinations of $|g\rangle$ and $|l\rangle$ ($|r\rangle$) [20]. The projection is a function of the displacement (radius r and angle γ) and the beam waist ω_0 .

2.2 State characterization

The measurement process consists of three stages of local state projection, one for each DOF. At each stage, the target state is transformed into a state that can be discriminated from the other states with high accuracy. Specifically, computer-generated phase holograms transform the target spatial mode into the pure gaussian (or 0-OAM) mode (see Fig. 2.2), which is then filtered by the single-mode fiber [20] (Fig. 2.1b). After a polarization controller to compensate for the fiber birefringence, wave plates transform the target polarization state into horizontal, which is filtered by a polarizer (Fig. 2.1d). The analysis of the energy-time state is realized by a Franson-type [22] polarization interferometer without detection post-selection [24]. The matched unbalanced interferometers give each photon a fast $|f\rangle$ and slow $|s\rangle$ route to its detector (see Fig. 2.3). Our interferometers consisted of $L \sim 11$ -mm quartz birefringent elements, which longitudinally separated the horizontal and vertical polarization components by $\Delta n_{\text{quartz}} L \sim 100 \mu\text{m}$, more than the single-photon coherence length ($\lambda^2/\Delta\lambda \sim 50 \mu\text{m}$ with $\Delta\lambda = 10 \text{ nm}$ from the interference filters) but much less than the pump-photon coherence length ($\sim 10 \text{ cm}$). We rely on the photons' polarization entanglement $|HH\rangle + |VV\rangle$ to thus project onto a two-time state ($|Hs, Hs\rangle + e^{i(\delta_1 + \delta_2)}|Vf, Vf\rangle$), where δ_1 and δ_2 are controlled by birefringent elements (liquid crystals and quarter-wave plates) in the path of each photon [24]. Finally, by analyzing the polarization in the $\pm 45^\circ$ basis, we erase the distinguishing polarization labels and can directly measure the coherence between the $|ss\rangle$ and $|ff\rangle$

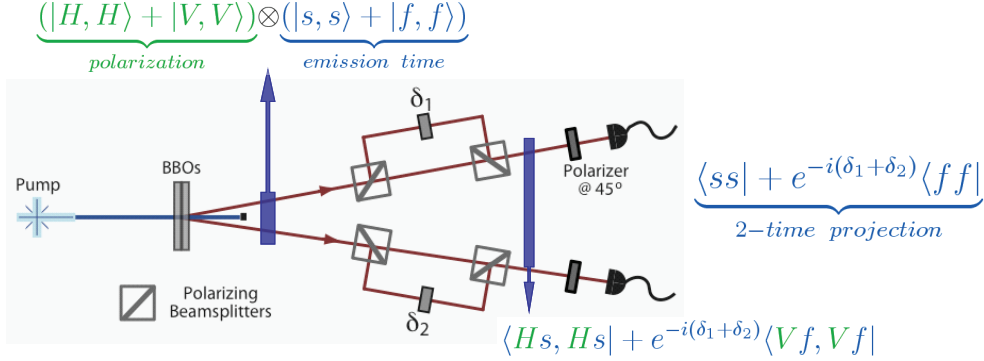


Figure 2.3: Experimental setup for the analysis of time-energy entangled states (see text). For clarity, the birefringent elements are shown as unbalanced interferometers. In our actual setup, we employ thick birefringent elements, which leads to a much more stable interferometer.

terms, arising from the energy-time entanglement. Our measurement, effectively applies the 2-time projector $\langle ss| + e^{-i(\delta_1+\delta_2)}\langle ff|$ to the input state.

2.3 Bell-inequality test in every DOF

To verify quantum mechanical correlations, we tested every DOF against a Clauser-Horne-Shimony-Holt (CHSH) Bell inequality [44]. The CHSH inequality places constraints ($S \leq 2$) on the value of the Bell parameter S , a combination of four two-particle correlation probabilities using two possible analysis settings for each photon. If $S > 2$, no separable quantum system (or local hidden variable theory) can explain the correlations; in this sense, a Bell inequality acts as an “entanglement witness” [45]. The Bell parameter is given by $S = |E(\theta_1, \theta_2) + E(\theta'_1, \theta_2) + E(\theta_1, \theta'_2) - E(\theta'_1, \theta'_2)|$, where $E(\theta_1, \theta_2)$ is a correlation coefficient³, given by

$$E(\theta_1, \theta_2) = \frac{R(\theta_1, \theta_2) - R(\theta_1, \theta_2^\perp) - R(\theta_1^\perp, \theta_2) + R(\theta_1^\perp, \theta_2^\perp)}{R(\theta_1, \theta_2) + R(\theta_1, \theta_2^\perp) + R(\theta_1^\perp, \theta_2) + R(\theta_1^\perp, \theta_2^\perp)},$$

and $R(\theta_1, \theta_2)$ is the measured coincidence counting rate with the analyzer for photon 1 (2) at θ_1 (θ_2)⁴.

To measure the strongest violation for the polarization and spatial-mode DOFs, we determined the optimal measurement settings by first tomographically reconstructing the 2-qubit subspace of

³Ideally, the various coincidence contributions to E would be measured simultaneously, e.g., by using both ports of the analyzing polarizing beam splitters, four detectors and four-fold coincidences. Lacking such apparatus, we approximated this by explicitly measuring the coincidence rate R for each analyzer setting, using θ^\perp to measure states orthogonal to the θ projection.

⁴Note that normalizing to the sum of the coincidence rates effectively amounts to a type of “fair-sampling” assumption, allowing one to perform a test despite low detection efficiencies.

interest; we employ a maximum likelihood technique to identify the density matrix most consistent with the data [43]. A simple optimization routine maximizes the expected violation as a function of the measurement settings and the knowledge of the input state.

Table 2.1 shows the Bell parameters measured for the polarization, spatial mode, and energy-time subspaces, with various projections in the complementary DOF. We see that for every subspace, the Bell parameter exceeded the classical limit of $S = 2$ by more than 20 standard deviations (σ), verifying the hyperentanglement. For both the polarization and spatial-mode measurements, we traced over the energy-time DOF by not projecting in this subspace. We measured the polarization correlations under several separate conditions, *i.e.*, while projecting the spatial modes into the orthogonal basis states ($|l\rangle$, $|g\rangle$, and $|r\rangle$), as well as the superpositions $|h\rangle \equiv (|l\rangle + |r\rangle)/\sqrt{2}$ and $|v\rangle \equiv (|l\rangle - |r\rangle)/\sqrt{2}$). The measured Bell parameters agreed (within $\sim 2\sigma$) with predictions from tomographic reconstruction and violated the inequality by more than 30σ . In the spatial mode DOF, the correlations for the state Φ_{spa}^+ were close to maximal ($S = 2\sqrt{2} \approx 2.83$), also in agreement with predictions from the measured state density matrix. In addition, we tested Bell inequalities for non-maximally entangled states in the OAM-subspace: $\alpha|gg\rangle + |rl\rangle$ and $\alpha|gg\rangle + |lr\rangle$; the measured Bell parameters in this case were slightly smaller (5%, max.) than predictions from tomographic reconstruction⁵, yet still 20σ above the classical limit. Finally, our measured Bell violation for the energy-time DOF using particular phase settings⁶ was in good agreement with the prediction ($S = 2\sqrt{2}V$) from the measured 2-photon interference visibility $V = 0.985(2)$.

2.4 Quantum state tomography of hyperentangled states

The polarization and spatial-mode state was fully characterized via tomography [43]. We performed the 1296 linearly independent state projections required for a full reconstruction in the $(2 \otimes 3) \otimes (2 \otimes 3)$ Hilbert space consisting of two polarization and all three OAM modes for each photon⁷. The measured state (Fig. 2.4) overlapped the anticipated state (polarization and spatial DOFs of Eq. 2.1) with a fidelity of 0.69(1) for $\alpha = 1.88e^{0.16i\pi}$ (numerically fitted), and $S_L = 0.46(1)$, suggesting the difference arises mostly from mixture. Treating the photon pairs as a six-level two-particle system,

⁵Displaced plane-wave holograms allow small leakage of unwanted states into the fiber [21]. This potentially explains the smaller-than-predicted Bell parameter for the non-maximally entangled spatial-mode states (e.g., $S_{\text{exp}} = 2.28(1)$ versus the prediction $S_{\text{pred}} = 2.35$).

⁶In analogy to the standard settings $\theta_1 = 0^\circ$, $\theta'_1 = 45^\circ$, $\theta_2 = 22.5^\circ$, and $\theta'_2 = 67.5^\circ$ for the state $\cos\theta|HH\rangle + \sin\theta|VV\rangle$, we used the same settings with $\phi = \theta/2$ for the time-energy projections $|ss\rangle + e^{i(\phi_1+\phi_2)}|ff\rangle$ (see Fig. 2.3).

⁷The number of measurements required to experimentally reconstruct a state from a Hilbert space of dimension d is d^2 , including normalization. Here, for our Hilbert space of dimension $2 \otimes 2 \otimes 3 \otimes 3$, we need $4 \times 4 \times 9 \times 9 = 1296$ measurements

Table 2.1: Bell parameter S showing CHSH-Bell inequality violations in every degree of freedom. The local realistic limit ($S \leq 2$) is violated by the number of standard deviations shown in brackets, determined by counting statistics. The last two rows describe measurements with non-maximally entangled states.

DOF	Spatial mode projected subspaces				
	$ gg\rangle\langle gg $	$ rl\rangle\langle rl $	$ lr\rangle\langle lr $	$ hh\rangle\langle hh $	$ vv\rangle\langle vv $
Φ_{poln}^+	2.76[76 σ]	2.78[46 σ]	2.75[44 σ]	2.81[40 σ]	2.75[33 σ]
$\Phi_{\text{t-e}}^+$	2.78[77 σ]	2.80[40 σ]	2.80[40 σ]	2.72[30 σ]	2.74[29 σ]
DOF	Polarization projected subspaces				
	no polarizers				
		$ HH\rangle\langle HH $	$ VV\rangle\langle VV $		
$ lr\rangle + rl\rangle$		2.78[78 σ]	2.80[36 σ]	2.79[37 σ]	
$\alpha gg\rangle + rl\rangle$		2.33[55 σ]	2.30[25 σ]	2.38[30 σ]	
$\alpha gg\rangle + lr\rangle$		2.28[47 σ]	2.26[20 σ]	2.31[26 σ]	

we can quantify the entanglement using the negativity N [46]. In this $6 \otimes 6$ Hilbert space, N ranges from 0 (for separable states) to 5 (for maximally-entangled states). Our measured partially mixed state had $N = 2.96(4)$, indicating strong entanglement, though somewhat less than the $N \approx 4.44$ predicted for the theoretically closest fit state $|\Psi_p\rangle$ (see Fig. 2.4). The spatial mode alone has $N = 1.14(2)$, greater than the maximum ($N = 1$) of any two-qubit system. Thus, our large state possessed 2-qubit and 2-qutrit entanglement.

We also selected a state (neglecting the $|gg\rangle$ component, Fig. 2.5a) maximally entangled in both polarization and spatial mode, that had $F = 0.974(1)$ with the target $\Phi_{\text{poln}}^+ \otimes \Phi_{\text{spa}}^+$. By tracing over polarization (spatial mode), we look at the measured state in the spatial mode (polarization) subspaces. The reduced states in both DOFs were pure ($S_L < 0.04$) and highly entangled ($T > 0.94$).

With this precise source of hyperentanglement, we have the flexibility to prepare nearly arbitrary polarization states [47], and to select arbitrary spatial-mode encoding. For example, we also generated a different maximally entangled state: $\Psi_{\text{poln}}^+ \otimes \Phi_{\text{spa}}^+$ (Fig. 2.5b). By coupling to and tracing over the energy-time DOF using quartz decoherers [47], we can add mixture to the polarization subspace, allowing us to prepare a previously unrealized state that simultaneously displays *classical correlations* in polarization and maximal *quantum correlations* between spatial modes (Fig. 2.5c): $\rho \approx \frac{1}{2}(|HH\rangle\langle HH| + |VV\rangle\langle VV|) \otimes |\Phi_{\text{spa}}^+\rangle\langle\Phi_{\text{spa}}^+|$. We were also able to accurately prepare the state $\rho_t = \frac{1}{4}I_{\text{poln}} \otimes |\Phi_{\text{spa}}^+\rangle\langle\Phi_{\text{spa}}^+|$, with no polarization correlations at all (i.e., completely mixed or unpolarized), while still maintaining near maximal entanglement in the spatial DOF (Fig. 2.5d).

In this chapter, we described the first realization of hyperentanglement of a pair of single photons. The entanglement in each DOF was demonstrated by violations of CHSH-Bell inequalities of greater

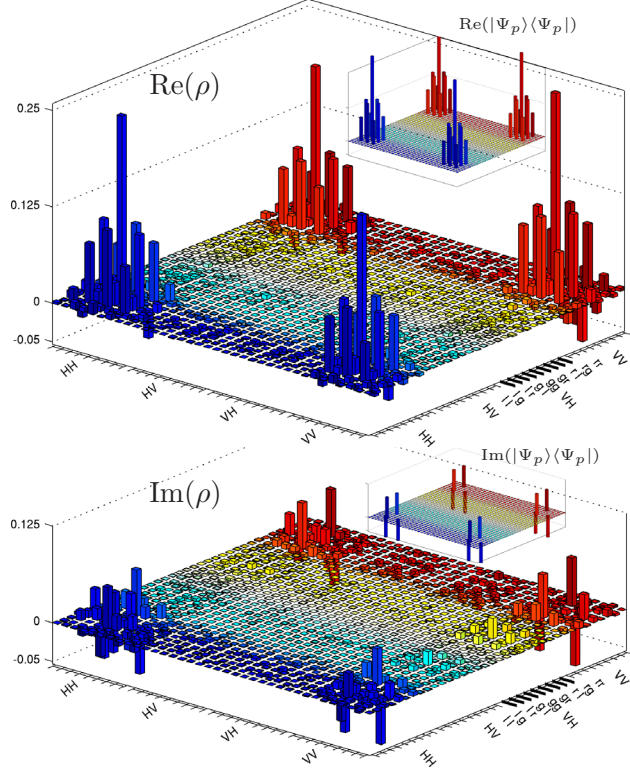


Figure 2.4: Measured density matrix (ρ) and close pure state ($|\Psi_p\rangle \sim \Phi_{\text{poln}}^+ \otimes (|lr\rangle + \alpha|gg\rangle + |rl\rangle)$ with $\alpha = 1.88e^{0.16i\pi}$) of a $2 \times 2 \times 3 \times 3$ -dimensional state of 2-photon polarization and spatial mode. Data were collected for 40s per projection with ~ 600 detected pairs/s.

than 20σ . Also, using tomography we fully characterized a $2 \otimes 2 \otimes 3 \otimes 3$ state, the largest quantum system to date. In a restricted $2 \times 2 \times 2 \times 2$ -dimensional subspace, we prepared a range of target states with unprecedented fidelity for quantum systems of this size, including novel states with a controllable degree of correlation in the polarization subspace. As we discussed in Chapter 1, these hyperentangled states enable 100%-efficient BSA [48], which is important for a variety of quantum information protocols [49, 50]. Because the spatial mode and energy-time DOFs are infinite in size, we envision further research possibilities by examining even larger subspaces, encoding higher-dimensional qudits [51, 52].

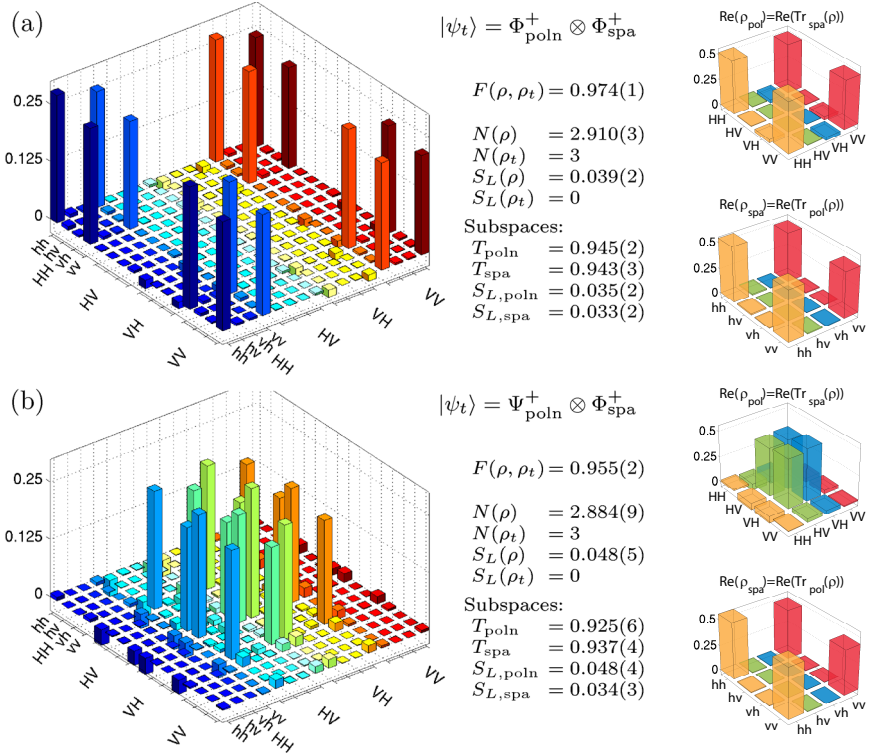


Figure 2.5: Measured density matrices (real parts) of $2 \times 2 \times 2 \times 2$ -dimensional states of 2-photon polarization and $(+1, -1)$ -qubit OAM. For each state, we list: the target state ρ_t , the fidelity $F(\rho, \rho_t)$ of the measured state ρ with the target ρ_t , their negativities and linear entropies, and the tangle and linear entropy for each subspace. On the right of each hyperentangled state, we show the real part of the polarization and spatial-mode subspaces –calculated by tracing the other DOF of the measured density matrix. The negativity for two-qubit states is the square root of the tangle. The magnitudes of all imaginary elements of the hyperentangled states, not shown, are less than 0.03. Data were collected for 20 s per projections with ~ 100 detected pairs/s.

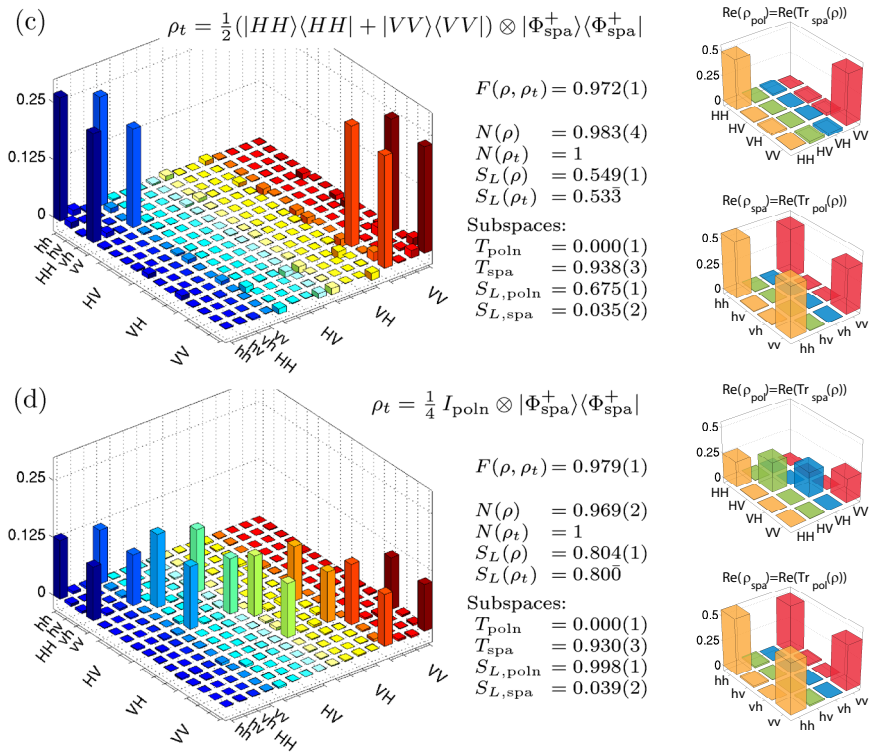


Figure 2.5 (continued).

Chapter 3

Hyperentanglement-assisted dense coding

Reproduced in part with permission from Macmillan Publishers Ltd: Nature Physics. J. T. Barreiro, N.-C. Wei, and P. G. Kwiat. Beating the channel capacity limit for linear photonic superdense coding. *Nature Physics* **4**, 282 (2008). Copyright (2008)

Dense coding is arguably the protocol that launched the field of quantum communication [49]. Until recently, however, more than a decade after its initial experimental realization [53], the channel capacity (CC) remained fundamentally limited as conceived for photons using linear elements. Bob could only send to Alice three of four potential messages due to the impossibility of performing the deterministic discrimination of all four Bell states with linear optics [54, 55], reducing the attainable CC from $\log_2 4 = 2$ to $\log_2 3 \approx 1.585$ bits. However, entanglement in an additional DOF enables the complete and deterministic discrimination of all Bell states [48, 56, 57]. Using pairs of photons simultaneously entangled in spin and orbital angular momentum [28, 58], we demonstrated the quantum advantage of the ancillary entanglement. In this chapter, we describe a dense-coding experiment with the largest reported CC and, to our knowledge, the first to break the conventional linear-optics threshold. Our encoding is suited for quantum communication without alignment [59] and satellite communication.

The first realization of quantum dense coding was optical, using pairs of photons entangled in polarization [53]. Dense coding has since been realized in various physical systems and broadened theoretically to include high-dimension quantum states with multiparties [60], and even coding of quantum states [61]. The protocol extension to continuous variables [62, 63] has also been experimentally explored optically, using superimposed squeezed beams [64]. Other physical approaches include a simulation in nuclear magnetic resonance with temporal averaging [65], and an implementation with atomic qubits on demand without postselection [66]. However, photons remain the optimal carriers of information given their resilience to decoherence and ease of creation and transportation.

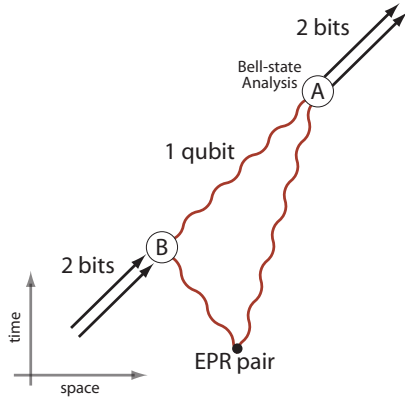


Figure 3.1: Quantum dense coding scheme as proposed by Bennett and Wiesner in 1992 [49]. Bob (B) sends 2 bits to Alice (A) encoded in 1 qubit. Channels transmitting bits (qubits) are shown as black straight (red curvy) lines.

Quantum dense coding was conceived [49] such that Bob could communicate two bits of classical information to Alice with the transmission of a single qubit, as follows (see Fig. 3.1). Initially, each party holds one spin- $\frac{1}{2}$ particle of a maximally entangled pair, in a known Bell state. Bob then encodes his 2-bit message by transforming the global state of the pair to one of the four Bell states, by applying one of four unitary operations on his particle, which he then transmits to Alice. Finally, Alice decodes the 2-bit message by discriminating the Bell state of the pair.

Alice's decoding step, deterministically resolving the four Bell states, is known as Bell State Analysis (BSA). While in principle attainable with nonlinear interactions, such BSA with photons is impossible to achieve with present technology, yielding extremely low efficiencies and low discrimination fidelities [67]. Therefore, current fundamental studies and technological developments demand the use of linear optics. However, for quantum communication, standard BSA with linear optics is also fundamentally impossible [54, 55]. At best only two Bell states can be discriminated; for quantum communication the other two are considered together for a three-message encoding. Consequently, the maximum CC of this conventional optical dense coding is $\log_2 3 \approx 1.585$ bits. Although there are probabilistic approaches that can distinguish all 4 Bell states (which would be necessary to achieve the fundamental CC of 2), these are at best successful 50% of the time [68], so have a net CC of at most 1 per photon. *i.e.*, the same as classical encoding allows.

3.1 Theory

Entanglement in an additional DOF of the pair, hyperentanglement [27], enables full BSA with linear optics [48, 56]. In this case, since Bob only encodes information in one DOF (the auxiliary DOF is unchanged), a dense-coding protocol proceeds under the same encoding conditions as in the original proposal [49]. Although hyperentanglement-assisted BSA (HBSA) on polarization states has been reported with ancillas entangled in energy-time [56] and linear-momentum [57], no advantage for quantum information or fundamental physics was shown before; earlier experiments at best achieved $CC < 1.18(3)$ bits [56], substantially less than is possible even without hyperentangled resources.

Using pairs of photons entangled in their spin and OAM in a HBSA with high stability and high detection fidelity, we realized a dense-coding experiment with a channel capacity that exceeds the threshold to beat conventional linear-optics schemes. In our scheme, Alice and Bob are provided with pairs of photons simultaneously entangled in their spin and ± 1 -OAM, in a state of the form

$$\frac{1}{2}(|HH\rangle + |VV\rangle) \otimes (|lr\rangle + |rl\rangle). \quad (3.1)$$

Bob encodes his message by applying one of four unitary operations on the spin of his photon of this hyperentangled pair: (1) the identity, (2) $V \rightarrow -V$, (3) $H \leftrightarrow V$, or (4) $V \rightarrow -V$ and $H \leftrightarrow V$. Such operations transform the state in equation 3.1 into

$$\Phi_{\text{spin}}^{\pm} \otimes \Psi_{\text{orbit}}^{+}, \text{ and } \Psi_{\text{spin}}^{\pm} \otimes \Psi_{\text{orbit}}^{+}, \quad (3.2)$$

where the spin and orbit Bell-states are defined as

$$\begin{aligned} \Phi_{\text{spin}}^{\pm} &\equiv (|HH\rangle \pm |VV\rangle) / \sqrt{2}, \\ \Psi_{\text{spin}}^{\pm} &\equiv (|HV\rangle \pm |VH\rangle) / \sqrt{2}, \\ \Psi_{\text{orbit}}^{+} &\equiv (|lr\rangle + |rl\rangle) / \sqrt{2}. \end{aligned}$$

We designed a HBSA scheme (inspired by Ref. [69]) enabling Alice to discriminate the four states in equation 3.2. In this scheme, the polarization BSA relies on the observation that the states resulting from Bob's encoding can be rewritten as superpositions of the single-photon Bell-states of

spin and orbital angular momentum, or spin-orbit Bell-states:

$$\begin{aligned}\phi^{\pm} &\equiv \frac{1}{\sqrt{2}}(|Hl\rangle \pm |Vr\rangle), \\ \psi^{\pm} &\equiv \frac{1}{\sqrt{2}}(|Hr\rangle \pm |Vl\rangle).\end{aligned}\quad (3.3)$$

In this basis, the states Alice analyzes have the form

$$\begin{aligned}\Phi_{\text{spin}}^{\pm} \otimes \Psi_{\text{orbit}}^{+} &= \frac{1}{2}(\phi_1^+ \otimes \psi_2^{\pm} + \phi_1^- \otimes \psi_2^{\mp} + \psi_1^+ \otimes \phi_2^{\pm} + \psi_1^- \otimes \phi_2^{\mp}), \\ \Psi_{\text{spin}}^{\pm} \otimes \Psi_{\text{orbit}}^{+} &= \frac{1}{2}(\pm \phi_1^+ \otimes \phi_2^{\pm} \mp \phi_1^- \otimes \phi_2^{\mp} \pm \psi_1^+ \otimes \psi_2^{\pm} \mp \psi_1^- \otimes \psi_2^{\mp}).\end{aligned}\quad (3.4)$$

This arrangement shows that each hyperentangled state is a unique superposition of four of the sixteen possible combinations of 2-photon spin-orbit Bell-states. Therefore, Alice can decode Bob's message by performing spin-orbit BSA locally on each photon.

3.2 Experiment

We implemented the spin-orbit BSA with a novel interferometric apparatus consisting of a ± 1 -OAM splitter and polarizing beam splitters (PBS), as shown in Fig. 3.2. The first splitter combines the action of a binary plane-wave phase grating [39] and single-mode fibers. The grating transforms an incoming photon in the state $|l\rangle$ ($|r\rangle$) into a gaussian beam with no OAM in the $+1$ (-1) diffraction order (for a splitter that preserves the photon's OAM, see Ref. [39]). Subsequently filtering the first diffraction orders with single-mode fibers, we effectively split an incoming photon into its ± 1 -OAM components. By merging these diffraction orders on a PBS we perform a spin-controlled NOT gate over the photon OAM. In Fig. 3.2, the states ψ^{\pm} (ϕ^{\pm}) exit on the top (bottom) output port of the PBS. Followed by measurements in the diagonal basis, shown in Fig. 3.2 as PBS@45°, the desired measurement in the single-photon Bell-state basis is accomplished ¹.

Each step in the dense-coding protocol corresponds to a distinct experimental stage in Fig. 3.3: a hyperentanglement source, Bob's encoding components, and Alice's HBSA. The hyperentanglement source is realized via spontaneous parametric down-conversion in a pair of nonlinear crystals. Although the generated photon pairs are entangled in polarization, OAM, and emission time [28], we used only a subspace of the produced states, which was shown to have a state overlap or fidelity

¹Additional birefringent elements make this device a universal unitary gate for single-photon two-qubit states, in analogy with the device for polarization-linear momentum states in Ref. [70].

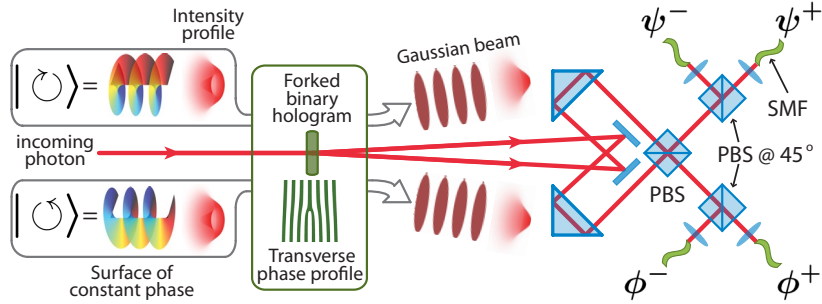


Figure 3.2: Spin-orbit Bell-state Analyzer. A photon in a spin-orbit Bell-state incident from the left is first split according to its ± 1 -OAM content; its ± 1 -OAM components are converted to 0-OAM and combined on a PBS for a spin-controlled orbit-CNOT gate. The photon is then filtered by a single mode fiber (SMF) and finally routed to a unique detector (photon-counting avalanche photodiode).

of 97% with the state in equation 3.1. Next, Bob encodes his message in the polarization state by applying birefringent phase shifts with a pair of liquid crystals, as shown in Fig. 3.3. Finally, Alice performs HBSA using two of the spin-orbit Bell-state analyzers shown in Fig. 3.2, one for each photon.

3.2.1 Experimental details

As in the previous chapter, the hyperentanglement source is realized by directing 120 mW of 351-nm light from a continuous-wave (CW) Ar⁺ laser into two contiguous BBO nonlinear crystals with optic axes aligned in perpendicular planes [28]. Type-I degenerate 702-nm photons in a 3.0° half-opening angle cone are produced by phase-matching each 0.6-mm thick crystal. In the spin and ± 1 OAM subspace, a two-fold coincidence rate of 5 detected pairs/s is determined by a 10-ns coincidence window and interference filters with $\Delta\lambda_{FWHM} = 5$ nm.

In our HBSA implementation each PBS@45° and its two outputs in the spin-orbit BSA (Fig. 3.2) were replaced by a dichroic polarizer oriented at either 45° or -45 ° and a single output; Alice's HBSA thus acquires all spin-orbit BSA outputs from 4 polarizer settings. With the CW source, Alice cycles through the four polarizer settings, and for each polarizer setting Bob encodes the four messages, each for 150 seconds. During the measurement, no active stabilization or realignment was done on the source, spin-orbit BSA interferometers, or coupling optics. The HBSA polarizers and liquid crystals were quickly set with computer-controlled rotation stages and liquid crystal controllers.

The wavelength-dependent voltage applied to each liquid crystal was independently calibrated to produce a birefringent phase difference of 0 or π with a diode laser operated at 699 nm (Hitachi HL-6738MG, driven at 140mA and 80°C); the same laser was used to align the ± 1 -OAM-splitter.

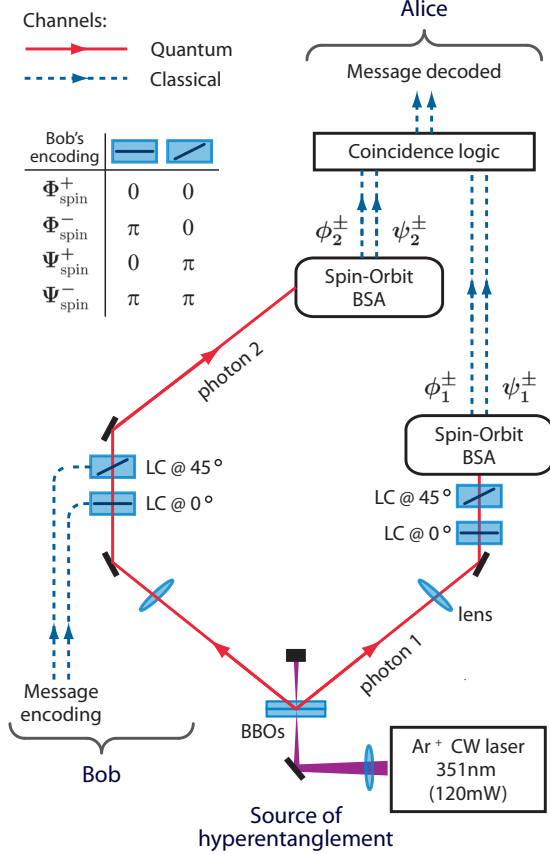


Figure 3.3: Experimental setup for dense coding with spin-orbit encoded photons. Acting on photon 2 of a hyperentangled pair, Bob encodes his message by using the liquid crystals (LC) to apply the phases indicated in the table, while (or earlier) Alice performs spin-orbit BSA on photon 1. Later –the upward direction suggests time progression– Alice uses a spin-orbit BSA on photon 2, and the result from the measurement on photon 1, to decode Bob’s message. The LCs on the path of photon 1 applied no phase during the dense-coding experiment, but were used along with Bob’s LCs to characterize the polarization states of the hyperentangled source by quantum state tomography. The LC optic axes are perpendicular to the incident beams; LC@45° (LC@0°) is oriented at 45° (0°) from the horizontal polarization direction.

The binary forked holograms were silver-halide emulsion gratings with 33%-diffraction efficiency into the first order (more efficient schemes are described in Ref. [39]). The same holographic plate included spatial-mode tomography patterns, which in conjunction with the liquid crystals were used for state reconstruction [28]. The spurious phase upon reflection on the PBS was compensated with a waveplate in each output port of the PBS for both spin-orbit Bell-state analyzers. The state discrimination SNR varied between states due to mode-coupling imbalance in the spin-orbit BSA, PBS crosstalk, and slight offsets in the liquid crystal calibrations.

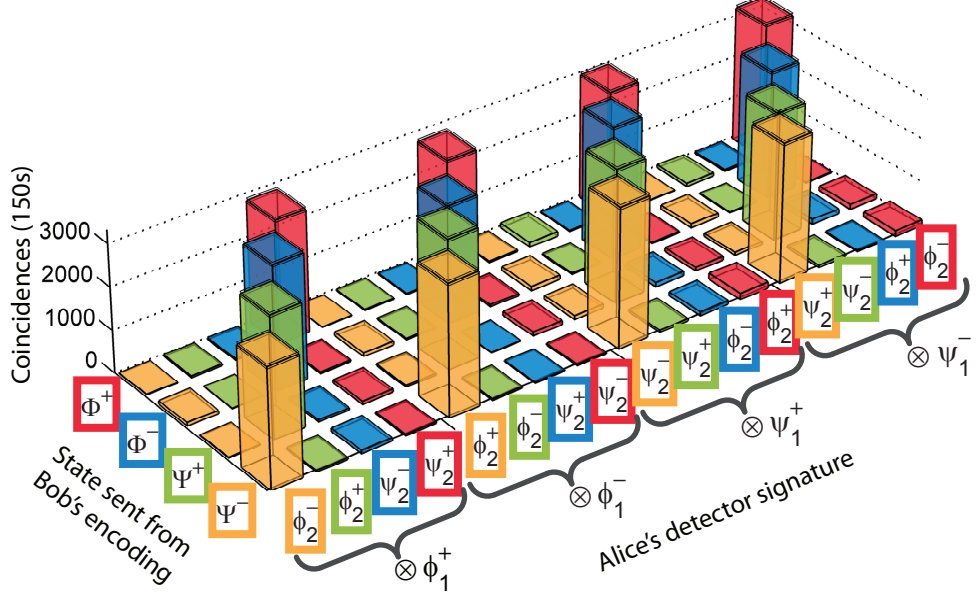


Figure 3.4: Experimental results of hyperentanglement-assisted dense coding. Coincidence counts detected by Alice’s HBSA for each message (state) sent by Bob. The error bars represent ± 1 standard deviations, deduced from poissonian counting statistics. The state-discrimination signal-to-noise ratios (SNR), which compare the sum of the four rates corresponding to the actual state to the sum of the other twelve registered rates, are $SNR_{\Phi^+} = 19.9(8)$, $SNR_{\Phi^-} = 27(1)$, $SNR_{\Psi^+} = 13.7(5)$, and $SNR_{\Psi^-} = 16.4(6)$.

3.3 Results

We characterize our dense-coding implementation by switching between the four states for equal intervals, and measuring all output states of the HBSA. The result of these measurements are coincidence counts for each input state, as shown in Fig. 3.4. From this data we can determine the conditional detection probabilities that Alice detects each message Φ^\pm and Ψ^\pm given that Bob sent, for example, the message Φ^+ . The probabilities shown in Fig. 3.5 were calculated by comparing the sum of the four rates corresponding to each detected message over the sum of all sixteen rates for the sent message. The average probability of success was 94.8(2)% (all reported errors from Monte Carlo simulations).

A better figure of merit for a quantum dense-coding implementation is the channel capacity ², since it characterizes the exponential growth of the maximum number of distinguishable signals for

²The capacity of a noisy channel is given by $CC = \max_{p(x)} H(X : Y)$, where x is in the space of signals that can be transmitted X , $H(X : Y)$ is the mutual information of X and the space of received signals Y , and the maximum is taken over all input distributions $p(x)$. $H(X : Y)$ is a function of $p(x)$ and the conditional detection distribution $p(y|x)$ of receiving y given that x was sent:

$$H(X : Y) = \sum_{y \in Y} \sum_{x \in X} p(x)p(y|x) \log \frac{p(y|x)}{\sum_{x \in X} p(y|x)p(x)}.$$

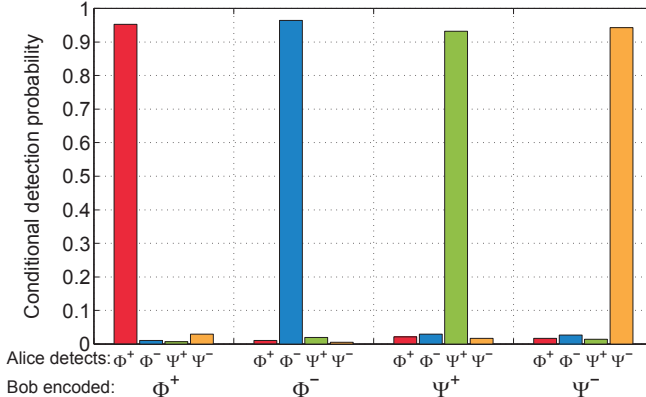


Figure 3.5: Conditional detection probabilities beating the CC limit for standard dense-coding with linear optics. Given that Bob encoded the four states indicated, Alice infers the state transmitted with the probabilities shown (calculated from data in Fig. 3.4). Her average success probability is 94.8(2)%. The statistical uncertainty in each probability is less than 0.2%. These results imply a CC of 1.630(6) bits, above the standard linear-optics limit of 1.585.

a given number of uses of the channel. From the conditional detection probabilities, we obtain a CC of 1.630(6) bits with a probability of sending each state of $P(\Phi^+) = 0.26$, $P(\Phi^-) = 0.26$, $P(\Psi^+) = 0.24$, and $P(\Psi^-) = 0.24$ ³. This exceeds the 1.585 CC threshold for conventional linear-optics implementations. The CC drifted by no more than one standard deviation between experimental runs, demonstrating the high stability of the implementation. To put our results in perspective with earlier implementations, we have plotted the experimentally achieved channel capacities as a function of the conditional detection average success probability in Fig. 3.6.

The experimental CC is nevertheless smaller than the maximum attainable (2 bits), due to imperfections in the alignment, input states and components. By characterizing each imperfection and modeling the gates and measurement, we estimated their effect on the channel capacity (see Appendix C.2). We characterized the source polarization state Φ_{spin}^+ by quantum state tomography in the $|lr\rangle$ and $|rr\rangle$ OAM subspaces [28] (using LCs shown in Fig. 3.3 and PBS of each spin-orbit BSA shown in Fig. 3.2). Considering all combinations of signature detectors, we measured an average degree of entanglement or tangle of $T = 96.7(8)\%$ and a mixture or linear entropy of $S_L = 2.0(4)\%$. If such high-quality polarization state were exactly the same for each combination of signature detectors, the decrease in the CC would only be 0.006 bits. However, small differences in the coupled state between each combination of detectors (expressed above as uncertainty) result in a CC decrease of 0.09(2) (see Appendix C.2). The OAM state was also tomographically reconstructed in the $|HH\rangle$

³In our experiment, a uniform probability of transmission gives a mutual information of 1.629(6) bits, negligibly smaller than the CC due to the nearly balanced conditional probabilities, i.e., there is little to be gained by sending some states more frequently.

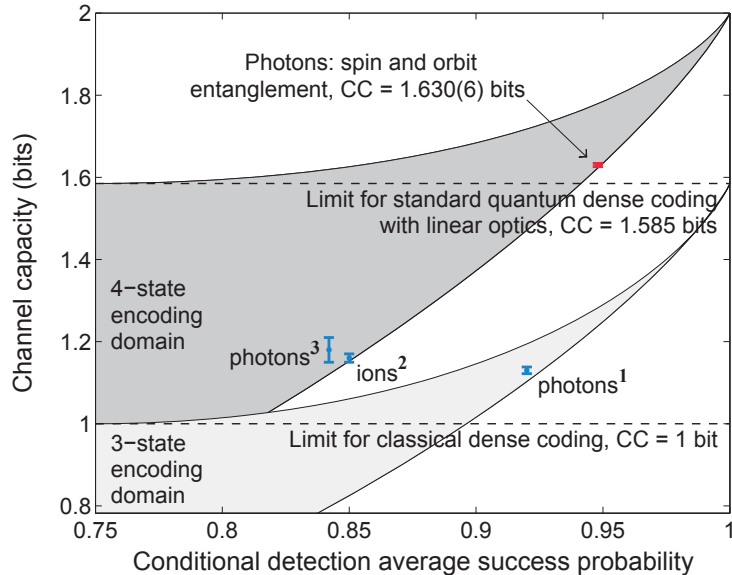


Figure 3.6: Experimentally reported CCs as a function of their conditional detection average success probability, using: **1** photons entangled in polarization [53], **2** trapped atomic ions entangled in their hyperfine levels [66], **3** photons entangled in polarization and energy-time [56]. The error bars represent the statistical error of ± 1 standard deviations. The domains of achievable channel capacity for both 3- and 4-state encodings are shown for reference (see Appendix C.1).

and $|VV\rangle$ polarization subspaces [28], measuring an average $T = 91(3)\%$ and $S_L = 6(2)\%$, yielding a CC decrease of $0.20(3)$ bits. The PBS crosstalk (0.5% for H , 1.0% for V) further decreases the CC by $0.10(1)$ bits. Finally, accidental coincidences (5 in 150s) reduce CC by 0.02 bits. Considering all mentioned imperfections and their spread in a Monte Carlo simulation, the predicted CC of $1.64(2)$ bits agrees with the measured CC of $1.630(6)$ bits.

The polarization and spatial-mode states can be improved by spatially compensating the angle-dependent phase [71], using a forked hologram with a smaller diffraction angle to decrease wavelength dispersion (a potential source of alignment imbalances), and obtaining crystals with a smaller wedge. The deleterious effect of the PBS crosstalk can be reduced by adding extra phase-compensation plates inside the interferometers, and can potentially be eliminated altogether by adding appropriate birefringent beam displacers after each PBS.

3.4 Conclusions

Above, Bob encoded two qubits in the form of spin-orbit Bell-states by acting only on the spin DOF. However, more generally he could also apply one of four unitaries in the ± 1 -OAM subspace and encode four qubits. The state of the pair of photons then becomes a product of Bell states,

16 in total. In principle, if Alice could discriminate all these “hyper-Bell” states, up to 4 bits could be transmitted per photon. In the next chapter, we will discuss the limits for unambiguously distinguishing these Bell-like states. In summary, we found that the optimal one-shot discrimination scheme is to group the 16 states into 7 distinguishable classes [72]. The optimal analysis can be achieved by the Kwiat-Weinfurter scheme [48], with photon-number resolving detectors⁴, giving a maximum CC of $\log_2 7 \approx 2.81$ bits. If we modify the present scheme, we can also implement an unambiguous discrimination of all 16 Bell states with two identical copies [72].

In conclusion, we beat a fundamental limit on the channel capacity for standard dense coding using only linear optics. A number of features make our HBSA efficient and reliable. First, hyperentanglement offers advantages in the source, logic gates and detection side. Quantum logic between qubits encoded on different DOFs is much more easily implemented than when using different photons [29, 73]. From the source side, more quantum information is available per photon, particularly with the energy-time and spatial-mode DOF (e.g., [74]). In the detection side, compared to multi-photon approaches, higher efficiency is achieved because only one pair of photons is detected. Second, since our HBSA requires only local measurements, Alice can measure one of the photons and store the classical result of her measurement until Bob sends his photon (i.e., she does not require a quantum memory). Finally, the photon’s polarization and ± 1 -OAM constitute a robust encoding as they enable quantum communication without alignment [59] as well as other landmark advances for quantum information [58]. Furthermore, by using paraxial beams as the ancillary DOF, the scheme is free of tight source-to-detector requirements such as interferometric stability [57] or perfect indistinguishability for HOM interference [56]. However, OAM single-photon and entangled states easily decohere by atmospheric turbulence [75, 76], limiting their likely communication applications to satellite-to-satellite transmissions.

⁴Without photon-number resolving detectors, at most 6 distinguishable classes can be identified, corresponding to a CC of $\log_2 6 \approx 2.59$ bits.

Chapter 4

Hyperentangled Bell-state analysis

Reproduced in part with permission from T.-C. Wei, J. T. Barreiro, and P. G. Kwiat. Hyperentangled Bell-state analysis. *Phys. Rev. A* **75**, 060305(R) (2007). Copyright 2007 American Physical Society, U.S.A. The work described in this chapter was lead and mostly done by TCW, my contribution lies on working with TCW on analyzing (and finding errors on) the paper that describes the method used and implementing it on MATHEMATICA.

As discussed in the previous chapter, just as the controlled-NOT [77] is one of the most important two-qubit gates in quantum computation, Bell measurement is one of the most important two-qubit measurements, since it enables many applications in quantum information processing, such as superdense coding [49, 53], teleportation [78, 79, 80], quantum fingerprinting [81, 82], and direct characterization of quantum dynamics [83]. However, it was shown that complete Bell-state analysis (BSA) using linear optics is not possible [54, 55], and that the optimal probability of success is only 50% [55, 68, 84], for which the optimal BSA schemes have been realized experimentally [53, 85, 86]. But Kwiat and Weinfurter (KW) [48] showed that with additional degrees of freedom, such as timing or momentum, it is indeed possible to achieve complete BSA for four Bell states, given that the additional degrees are in a fixed entangled state, as shown in the previous chapter. Other similar BSA schemes have also been proposed [69, 87, 88] and implemented [57, 89]. All these hyperentanglement-assisted measurements are termed embedded BSA [48]. The KW scheme for BSA has recently been implemented by Schuck et al. [56]. Nevertheless, adding additional degrees of freedom also enlarges the Hilbert space, and hence the number of Bell-like states (*e.g.*, see Table 4.1); all previous investigations on embedded BSA have focused on a subset of these states (*i.e.*, states where one of the DOF is one Bell state, *e.g.*, $|\phi^+\rangle$). It is therefore important to set theoretical limits on optimal BSA in the enlarged Hilbert space.

In this chapter, we investigate the optimality of hyperentanglement-assisted BSA, with both degrees of freedom being qubit-like, such as polarization (H and V) plus either two momenta (spatial directions) or two OAM or two time bins. The resulting Bell-like states –”hyper-Bell states”– for

two photons thus total sixteen. We show that an unambiguous state discrimination is impossible but that the optimal scheme divides the 16 hyper-Bell states into 7 distinct groups. We also show by construction that two copies of the same state are necessary and sufficient to enable an unambiguous discrimination of any of the sixteen states. Finally, we discuss the implications for superdense coding, teleportation and quantum fingerprinting.

4.1 Kwiat-Weinfurter scheme for Bell-state analysis

KW showed that when the momentum degrees of freedom are in a fixed entangled state, the four polarization Bell states can be unambiguously distinguished [48]. Let us introduce the 16 Bell-like states, constructed from two photons with polarization and momentum (or spatial mode) or timing degrees of freedom: (1) $\{H, V\} \otimes \{a, c\}$ and (2) $\{H, V\} \otimes \{b, d\}$ ¹. These states result from the different combinations of the four polarization Bell states,

$$|\Phi^\pm\rangle \equiv (|H\rangle_1|H\rangle_2 \pm |V\rangle_1|V\rangle_2)/\sqrt{2}, \quad (4.1a)$$

$$|\Psi^\pm\rangle \equiv (|H\rangle_1|V\rangle_2 \pm |V\rangle_1|H\rangle_2)/\sqrt{2}, \quad (4.1b)$$

and the four momentum Bell states,

$$|\phi^\pm\rangle \equiv (|a\rangle_1|b\rangle_2 \pm |c\rangle_1|d\rangle_2)/\sqrt{2} \quad (4.1c)$$

$$|\psi^\pm\rangle \equiv (|a\rangle_1|d\rangle_2 \pm |c\rangle_1|b\rangle_2)/\sqrt{2}. \quad (4.1d)$$

The detection patterns for the KW scheme (Fig. 4.1) are shown in Table 4.1. The 16 states are divided into 7 distinct classes according to the measurement outcome². Except that one class contains 4 states, all others each have 2 states. Thus, no single state can be unambiguously distinguished using this scheme. If the momentum state is ϕ^+ , the four states with distinct polarization Bell states belong to four distinct classes, and hence can be distinguished. Similarly, if the polarization state is Φ^+ , the states with four distinct momentum Bell states can be distinguished. Therefore, the same setup can perform full BSA for either degree of freedom.

¹The basis states for photon 1 are therefore composed of $\{|Ha\rangle_1, |Hc\rangle_1, |Va\rangle_1, |Vc\rangle_1\}$ and those for photon 2, $\{|Hb\rangle_2, |Hd\rangle_2, |Vb\rangle_2, |Vd\rangle_2\}$; see Fig. 4.1.

²There is one class of four detector outcomes missing. However, this class, indicated in the last line of Table 4.1, could be realized, e.g., by the following two states: $(H_1V_2 - V_1H_2)(a_1c_2 - b_1d_2)$ and $(H_1V_2 + V_1H_2)(a_1c_2 - b_1d_2)$, which reside outside the Hilbert space spanned by the 16 Bell states and are composed of photon 1 having spatial modes a and b and photon 2 having c and d .

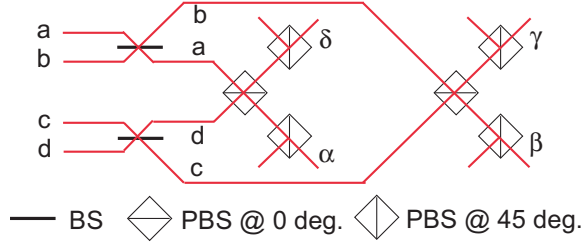


Figure 4.1: Kwiat-Weinfurter scheme for the embedded Bell-state analysis.

Table 4.1: Detection signature table for the Kwiat-Weinfurter embedded BSA scheme. $\Phi^\pm \equiv (H_1 H_2 \pm V_1 V_2)$, $\Psi^\pm \equiv (H_1 V_2 \pm V_1 H_2)$, $\phi^\pm \equiv (a_1 b_2 \pm c_1 d_2)$, and $\psi^\pm \equiv (a_1 d_2 \pm c_1 b_2)$. The subscript 45 indicates the port associated with transmission through the polarizing beam splitter and $\overline{45}$ that with reflection. The final row lists a unique detection signature, corresponding, however, to states outside the Hilbert space spanned by the 16 hyperentangled Bell states.

Class	State	Detector signature
1	$\Phi^+ \otimes \phi^+$, $\Phi^- \otimes \phi^-$ $\Psi^+ \otimes \psi^-$, $\Psi^- \otimes \psi^+$	$\alpha_{45}\alpha_{45}, \alpha_{\overline{45}}\alpha_{\overline{45}}, \beta_{45}\beta_{45}, \beta_{\overline{45}}\beta_{\overline{45}}$ $\delta_{45}\delta_{45}, \delta_{\overline{45}}\delta_{\overline{45}}, \gamma_{45}\gamma_{45}, \gamma_{\overline{45}}\gamma_{\overline{45}}$
2	$\Phi^- \otimes \phi^+$, $\Phi^+ \otimes \phi^-$	$\alpha_{45}\alpha_{\overline{45}}, \beta_{45}\beta_{\overline{45}}, \delta_{45}\delta_{\overline{45}}, \gamma_{45}\gamma_{\overline{45}}$
3	$\Psi^- \otimes \psi^-$, $\Psi^+ \otimes \psi^+$	$\alpha_{45}\beta_{45}, \alpha_{\overline{45}}\beta_{\overline{45}}, \delta_{45}\gamma_{45}, \delta_{\overline{45}}\gamma_{\overline{45}}$
4	$\Psi^+ \otimes \phi^+$, $\Phi^+ \otimes \psi^-$	$\alpha_{45}\delta_{45}, \alpha_{\overline{45}}\delta_{\overline{45}}, \beta_{45}\gamma_{45}, \beta_{\overline{45}}\gamma_{\overline{45}}$
5	$\Psi^+ \otimes \phi^-$, $\Phi^- \otimes \psi^-$	$\alpha_{45}\delta_{\overline{45}}, \alpha_{\overline{45}}\delta_{45}, \beta_{45}\gamma_{\overline{45}}, \beta_{\overline{45}}\gamma_{45}$
6	$\Psi^- \otimes \phi^+$, $\Phi^+ \otimes \psi^+$	$\alpha_{45}\gamma_{45}, \alpha_{\overline{45}}\gamma_{\overline{45}}, \beta_{45}\delta_{45}, \beta_{\overline{45}}\delta_{\overline{45}}$
7	$\Psi^- \otimes \phi^-$, $\Phi^- \otimes \psi^+$	$\alpha_{45}\gamma_{\overline{45}}, \alpha_{\overline{45}}\gamma_{45}, \beta_{45}\delta_{\overline{45}}, \beta_{\overline{45}}\delta_{45}$
*	$\Psi^\pm \otimes (a_1 c_2 - b_1 d_2)$	$\alpha_{45}\beta_{45}, \alpha_{\overline{45}}\beta_{\overline{45}}, \delta_{45}\gamma_{\overline{45}}, \delta_{\overline{45}}\gamma_{45}$

4.2 Optimal hyperentangled Bell-state analysis

4.2.1 Proof of optimality

One may wonder what the optimal Bell-state analysis is. Calsamiglia [84] showed that any element $|u_i\rangle\langle u_i|$ in a generalized measurement (i.e., POVM $\sum_i \lambda_i |u_i\rangle\langle u_i| = \mathbb{1}$, with $\sum_i \lambda_i = 1$) on two qudits (qudits composed of identical particles) of linear optics can have a Schmidt rank ³ at most of 2. As shown in the single-photon decomposition in the previous chapter, our hyperentangled Bell states have Schmidt rank 4. This means that no single state can be distinguished from any other, and so unambiguous and complete BSA for the 16 states is not possible. Thus, the optimal scheme groups the states into classes, in our case, at most 8 distinguishable classes. However, our analysis of the KW scheme (Table 4.1) identifies only 7 classes. Now we shall prove that 7 is in fact the upper limit.

We utilize the method of van Loock and Lütkenhaus [91] to test whether 8 classes can be

³Any pure state can be represented by a sum of biorthogonal terms called the Schmidt decomposition. The Schmidt rank is the number of nonvanishing terms in such an expansion [90].

discriminated. They showed that a necessary condition for the distinguishability of the states ψ_i and ψ_j ($i \neq j$) is [91]

$$\langle \psi_i | c_s^\dagger c_s | \psi_j \rangle = 0 \quad \text{with} \quad c_s = \sum_{i=1}^N \nu_i c_i, \quad (4.2)$$

where c_s is the annihilation operator, linearly composed of N modes (both input and auxiliary) via some unitary transformation, and thus the ν_i 's cannot all be zero. The rationale behind Eq. (4.2) is that in order for ψ_i and ψ_j to be distinguishable, the remaining states should maintain orthogonality after a single-photon detection at mode s . In addition, ancillary photons do not assist state discrimination if either input or auxiliary states have a fixed number of photons. This means that, in Eq. (4.2), N can be set as the number of input modes.

For the setup shown in Fig. 4.1, we relabel the input modes as $|1\rangle \equiv |H\rangle \otimes |a\rangle$, $|2\rangle \equiv |H\rangle \otimes |c\rangle$, $|3\rangle \equiv |V\rangle \otimes |a\rangle$, $|4\rangle \equiv |V\rangle \otimes |c\rangle$, $|5\rangle \equiv |H\rangle \otimes |b\rangle$, $|6\rangle \equiv |H\rangle \otimes |d\rangle$, $|7\rangle \equiv |V\rangle \otimes |b\rangle$ and $|8\rangle \equiv |V\rangle \otimes |d\rangle$, where H and V denote the polarization degree of freedom and a , b , c and d denote the momentum or direction (or angular-momentum) degree of freedom. Thus, the hyper-Bell states can be written as

$$|\Psi^{(\mu)}\rangle = \sum_{i,j=1\dots 8} W_{ij}^{(\mu)} c_i^\dagger c_j^\dagger |0\rangle, \quad (4.3)$$

where the symmetric matrices $W^{(\mu)}$ are 8×8 invertible (i.e., with nonzero determinant) and characterize the sixteen ($\mu = 1 \dots 16$) Bell states. If the optimal BSA groups the 16 Bell states into 8 classes, there must exist sets of 8 states for which the conditions set by Eq. (4.2) are satisfied. On the other hand, if 7 is the optimal number of classes, no set of 8 states can satisfy Eq. (4.2). To see whether the former or the latter is true, we have to check whether Eq. (4.2) can be satisfied for all possible combinations of 8 out of the 16 hyper-Bell states ($C_8^{16} = 12870$, though this number can be reduced by considering the group structure of operations that transform the 16 states onto themselves.)

First, as an example, take two states from class 1 and one from each of the other 6 classes: $\Phi^+ \otimes \phi^+$, $\Phi^- \otimes \phi^-$, $\Phi^- \otimes \phi^+$, $\Psi^- \otimes \psi^-$, $\Psi^+ \otimes \phi^+$, $\Psi^+ \otimes \phi^-$, $\Psi^- \otimes \phi^+$, and $\Psi^- \otimes \phi^-$. Applying Eq. (4.2) to these states, we have, after simplifying the equations,

$$|\nu_1| = |\nu_3|, |\nu_2| = |\nu_4|, |\nu_5| = |\nu_7|, |\nu_6| = |\nu_8| \quad (4.4a)$$

$$|\nu_1|^2 + |\nu_5|^2 = |\nu_2|^2 + |\nu_6|^2 \quad (4.4b)$$

$$\nu_7^* \nu_5 = \nu_2^* \nu_4 = \nu_6^* \nu_8 = \nu_3^* \nu_1 = 0. \quad (4.4c)$$

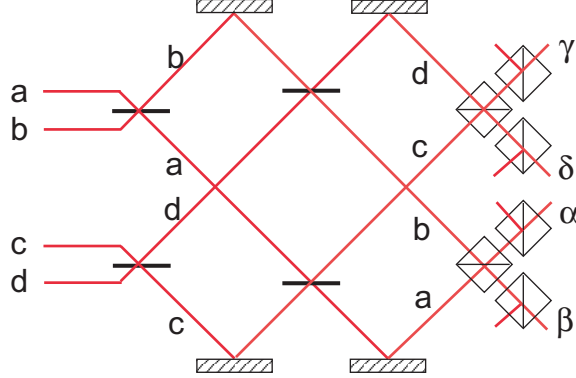


Figure 4.2: Modified KW scheme.

Table 4.2: Detection signature for the modified KW scheme shown in Fig. 4.2.

Class	State	Detector signature
1'	$\Phi^+ \otimes \phi^-$, $\Psi^- \otimes \phi^-$ $\Phi^+ \otimes \psi^+$, $\Psi^- \otimes \psi^+$	$\alpha_{45}\alpha_{45}$, $\alpha_{\overline{45}}\alpha_{\overline{45}}$, $\beta_{45}\beta_{45}$, $\beta_{\overline{45}}\beta_{\overline{45}}$, $\delta_{45}\delta_{45}$, $\delta_{\overline{45}}\delta_{\overline{45}}$, $\gamma_{45}\gamma_{45}$, $\gamma_{\overline{45}}\gamma_{\overline{45}}$
2'	$\Phi^- \otimes \phi^-$, $\Phi^- \otimes \psi^+$	$\alpha_{45}\alpha_{\overline{45}}$, $\beta_{45}\beta_{\overline{45}}$, $\delta_{45}\delta_{\overline{45}}$, $\gamma_{45}\gamma_{\overline{45}}$
3'	$\Psi^+ \otimes \phi^-$, $\Psi^+ \otimes \psi^+$	$\alpha_{45}\beta_{45}$, $\alpha_{\overline{45}}\beta_{\overline{45}}$, $\delta_{45}\gamma_{45}$, $\delta_{\overline{45}}\gamma_{\overline{45}}$
4'	$\Psi^+ \otimes \phi^+$, $\Phi^- \otimes \psi^-$	$\alpha_{45}\delta_{45}$, $\alpha_{\overline{45}}\delta_{\overline{45}}$, $\beta_{45}\gamma_{45}$, $\beta_{\overline{45}}\gamma_{\overline{45}}$
5'	$\Phi^+ \otimes \psi^-$, $\Psi^- \otimes \psi^-$	$\alpha_{45}\delta_{\overline{45}}$, $\alpha_{\overline{45}}\delta_{45}$, $\beta_{45}\gamma_{\overline{45}}$, $\beta_{\overline{45}}\gamma_{45}$
6'	$\Phi^+ \otimes \phi^+$, $\Psi^- \otimes \phi^+$	$\alpha_{45}\gamma_{45}$, $\alpha_{\overline{45}}\gamma_{\overline{45}}$, $\beta_{45}\delta_{45}$, $\beta_{\overline{45}}\delta_{\overline{45}}$
7'	$\Phi^- \otimes \phi^+$, $\Psi^+ \otimes \psi^-$	$\alpha_{45}\gamma_{\overline{45}}$, $\alpha_{\overline{45}}\gamma_{45}$, $\beta_{45}\delta_{\overline{45}}$, $\beta_{\overline{45}}\delta_{45}$

These lead to the only solution $\nu_i = 0$, which is a contradiction. This shows that one cannot discriminate any state from the above eight states.

We checked all 12870 cases by programming MATHEMATICA to examine the conditions derived from Eq. (4.2), supplemented by the normalization condition $\sum_i |\nu_i|^2 = 1$. This was achieved by first enumerating and simplifying equations generated from Eq. (4.2), as well as the normalization condition, and then by using the function `FindInstance[]` to find an instance of solutions. One feature of `FindInstance[]` is that it will *always* find a solution if there is one. For all the 12870 cases, `FindInstance[]` returns an empty set, showing no solution. Therefore, we conclude that it is impossible to reliably distinguish among any set of 8 hyper Bell states, and that 7 is the optimal, as is realized in the KW scheme.

4.2.2 Unambiguous Bell-state discrimination?

Having seen that a one-shot measurement is unable to perfectly discriminate any hyper-Bell state, it seems natural to ask how many copies are necessary to enable such discrimination. We show here by construction that 2 copies are sufficient. First, we introduce a slightly modified measurement

scheme from that of KW, shown in Fig. 4.2. The corresponding detection patterns are shown in Table 4.2. From Tables 4.1 and 4.2 we see that no two states share the same class of detector signature. Therefore, we imagine letting one copy go through the KW scheme and the other through the scheme in Fig. 4.2. Suppose we obtain signatures in 1 and 2'. Combining both outcomes enables us to uniquely determine which of the 16 states was analyzed, e.g., $\Phi^- \otimes \phi^-$ in the example given⁴.

4.2.3 More degrees of freedom

We have shown that with one additional qubit-like degree of freedom for each photon, there exist 7 states (out of 16) that can be distinguished from one another. Next we consider for each photon n qubit-like degrees of freedom in total. In this case there are 4^n Bell-like states. What is the maximum number of distinguishable subsets of these states?

Let us begin by noting that we can express the 4^n Bell-like states in the form of Eq. (4.3), where the upper limit in the sum is now the number of input modes, 2^{n+1} . The matrices $W^{(\mu)}$ are now $(2^{n+1}) \times (2^{n+1})$. If one makes a unitary transformation of the modes (using the fact that one can set the number of modes equal to the number of input modes, ignoring any auxiliary mode), $a_i^\dagger = \sum_j U_{ij} c_j^\dagger$, the necessary condition for discrimination between states $\Psi^{(\mu)}$ and $\Psi^{(\nu)}$ ($\mu \neq \nu$) is

$$\langle \Psi^{(\mu)} | a_i^\dagger a_i | \Psi^{(\nu)} \rangle = 0 \Leftrightarrow \langle \psi_i^{(\mu)} | \psi_i^{(\nu)} \rangle = 0, \quad (4.5)$$

where we have defined $|\psi_i^{(\mu)}\rangle \equiv a_i |\Psi^{(\mu)}\rangle$. Because of the unitarity of W and U , $|\psi_i^{(\mu)}\rangle$ has nonzero norm and is equivalent to a 2^{n+1} -component vector. The above orthogonality condition then implies that there can be at most 2^{n+1} linearly-independent vectors of $\psi_i^{(\mu)}$ for fixed i . Thus, we see that the maximum number of Bell states that can be distinguished is bounded above by 2^{n+1} . This means that the ratio of the maximal number of mutually distinguishable sets of Bell states to the total number of Bell states decreases exponentially with n : $2^{n+1}/4^n = 2^{1-n}$.

We conjecture that $2^{n+1} - 1$ is a good upper bound for the number of distinguishable Bell-like states, as it is true for $n = 1$ (e.g., polarization only) and $n = 2$ (e.g., polarization plus two spatial modes). Generalizing to different dimensions of the degrees of freedom, the absolute upper bound on distinguishable Bell states can be shown to be $2d_1 d_2 d_3 \cdots d_n$.

⁴We found that a modification of the scheme by Walborn *et al.*, [69] also results in complete discrimination with two copies, consistent with the findings of Ghosh *et al.*, [92].

4.3 Implications for quantum communication

4.3.1 Superdense coding

Given that we can choose 7 Bell states such that they can be distinguished from one another, we can then take one of them as a shared entanglement and use 7 operations, taking the state to itself or 6 others, to encode 7 messages. For example, Alice and Bob share $\Psi^- \otimes \psi^-$. She can locally transform the state into 6 other states, $\Phi^+ \otimes \phi^+$, $\Phi^- \otimes \phi^+$, $\Psi^+ \otimes \phi^+$, $\Psi^- \otimes \phi^+$, $\Phi^- \otimes \psi^-$, and $\Phi^- \otimes \psi^+$. As these seven states can be distinguished using the KW scheme, Bob can uniquely determine the message encoded by Alice, giving a superdense coding of $\log_2 7 \approx 2.8$ bits. For two photons entangled only in polarization, a superdense coding encodes only $\log_2 3 \approx 1.58$ bits [53]. Even though its extension to two pairs encodes $\log_2 9 \approx 3.17$ bits, the four-photon detection efficiency η^4 is typically much smaller than the two-photon efficiency η^2 , where η is the single-photon detection efficiency (usually much smaller than 70%). However, the transmission efficiency of the hyperentangled scheme can be compared with the double pair scheme in terms of the average number of bits, or the number of messages [93]. In the former case, the double pair scheme has two contributions; since the information can be transmitted by detecting either photon pairs or all four photons, with an average number of bits of $2\eta^2(1 - \eta)^2 \log_2 3$ and $\eta^4 \log_2 9$, respectively. Therefore, hyperentangled schemes are superior if

$$\eta^2 \log_2 7 > 2\eta^2(1 - \eta)^2 \log_2 3 + \eta^4 \log_2 9,$$

or, if $\eta < 94\%$. On the other hand, if we compare the number of messages, hyperentangled schemes are superior if

$$\eta^2 7 > 2\eta^2(1 - \eta)^2 3 + \eta^4 9,$$

or, if $\eta < 80\%$. Thus, hyperentanglement for superdense coding seems more practical than multi-pair entanglement.

4.3.2 Quantum teleportation

A shared Bell-like state enables the teleportation of an unknown state. However, as complete BSA of a two-photon polarization state alone is not possible, schemes employing additional degrees of freedom have been proposed [48, 69]. The embedded Bell-analysis schemes proposed in Refs. [57, 69, 88], however, cannot be used for teleportation, as their measurements do not require two photons to interfere, and can be performed locally. If these schemes could enable teleportation, it would

imply that entanglement can be created locally by separated parties; but it is well known that local operations and classical communication cannot generate entanglement. Our analysis shows that the KW scheme enables the teleportation of an arbitrary state encoded in either polarization or momentum (not both) with a 50% probability of success, the same probability as the two-photon polarization BSA. Suppose a photon in Alice’s laboratory is in a state with known momentum but arbitrary polarization, $|\psi\rangle = (\alpha|H\rangle_1 + \beta|V\rangle_1) \otimes |h\rangle_1$, where $\{h, v\}$ is used to indicate its momentum degree of freedom. Alice and Bob share the Bell state $(\Phi^+ \otimes \phi^+)_{23}$ of photons 2 and 3. If Alice performs the KW BSA on photons 1 and 2, there is a 50% probability (and she knows whether it succeeds) that Bob can transform his photon into the state $(\alpha|H\rangle_1 + \beta|V\rangle_1)$ by performing the corresponding local operation according to Alice’s measurement outcome, and post-selecting the photon from his momentum modes b or d in $\phi^+ = (a_1 b_2 + c_1 d_2)$. Similarly, an arbitrary momentum state $|H\rangle_1 \otimes (\alpha|h\rangle_1 + \beta|v\rangle_1)$ can be teleported. The use of hyperentanglement of photons, unfortunately, does not seem to offer advantages for teleportation over the conventional polarization-only teleportation [79, 80], both having only 50% probability of success.

4.3.3 Quantum fingerprinting

Fingerprinting is a communication protocol in which two parties, Alice and Bob, want to test whether they receive the same message from a supplier, but as they cannot have direct communication with each other. Therefore, they have to communicate through a third party to test whether the two messages are the same. Instead of sending the whole messages, they send the corresponding “fingerprint” (a much shorter message) of their messages to the third party. A quantum protocol is superior to its classical counterpart because the former allows 100% fingerprinting success. It was shown that shared two-qubit Bell states enable perfect fingerprinting of binary-encoded $\{0, 1\}$ messages [81, 82]. We propose using hyperentanglement of a pair of photons to achieve perfect fingerprinting of $\{0, 1, \dots, 6\}$ encoded messages. Analogously to dense coding with hyperentanglement, Alice and Bob share the state $\Psi^- \otimes \psi^-$, and both parties can locally transform the shared state into the 7 states: $\Psi^- \otimes \psi^-$, $\Phi^+ \otimes \phi^+$, $\Phi^- \otimes \phi^+$, $\Psi^+ \otimes \phi^+$, $\Psi^- \otimes \phi^+$, $\Phi^- \otimes \psi^-$, and $\Phi^- \otimes \psi^+$. Thus, they encode their fingerprints locally by applying the required operations, and a referee can perform the BSA on the resulting two-photon state to determine whether the fingerprints are the same.

4.4 Concluding remarks

We have investigated the optimal Bell-state analysis using projective measurements in linear optics for hyperentangled Bell states. The results are relevant as there has been recent experimental progress in realizing BSA of hyperentangled states [56, 57, 89]. In particular, we have shown that when the additional degrees of freedom are also qubit-like, the resulting 16 Bell-like states can be, at best, divided into 7 distinct classes. Moreover, we have provided a method to unambiguously discriminate any of the 16 Bell states, given two copies of the state. We have also discussed the implications for superdense coding, teleportation, and fingerprinting. We conclude with two open issues for future study: 1) how generalized measurements might be used to help Bell analysis in general; and 2) whether other methods such as that of Eisert [94] may provide alternative approaches to understand the results presented here.

Chapter 5

Remote Entangled State Preparation

5.1 Remote state preparation

As discussed in Chapter 3, to send two bits of information from Bob to Alice using only one qubit, we use quantum dense coding. For a complementary protocol, where a qubit in an *unknown* quantum state needs to be sent using only two bits, we may use teleportation [78] (see Fig. 5.1). However, if the quantum state of the qubit to be send is *known*, it has been shown [95, 96, 97] that the classical communication costs are less than teleportation. This variant of teleportation has been called “remote state preparation” (RSP) by Bennett *et al.* [97]. Similar to the teleportation protocol, RSP relies on the correlations of an entangled pair of qubits to prepare Alice’s qubit in a particular state determined by Bob and conditional on the outcome of a measurement on his qubit. RSP not only requires fewer resources, but escapes the need of Bell-state analysis (unlike teleportation), an experimental challenge for optical implementations.

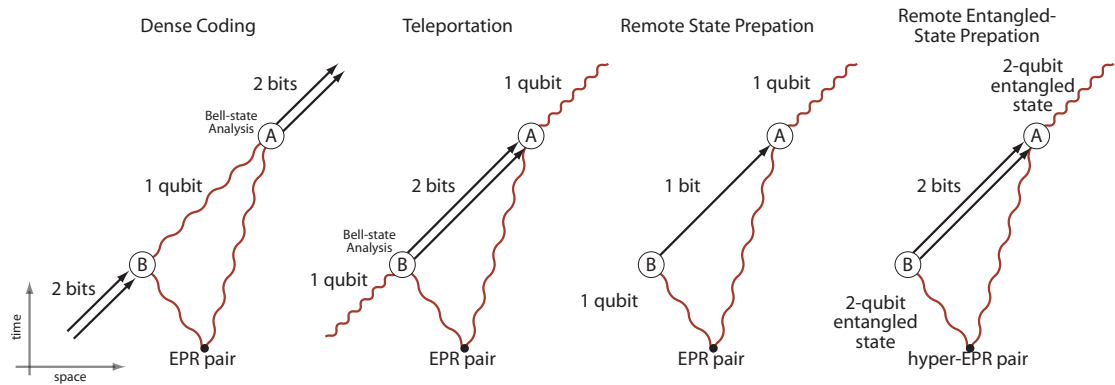


Figure 5.1: Fundamental quantum communication protocols: Dense coding, teleportation, remote state preparation and remote entangled-state preparation. In dense coding, as shown also in Fig. 3.1, Bob (B) sends 2 bits to Alice (A) encoded in 1 qubit. In teleportation, 1 qubit in an *unknown* state is sent encoded in 2 bits. Dense coding and teleportation both require BSA. In remote state preparation, the *known* state of 1 qubit is sent encoded in 1 bit. Finally, in remote entangled-state preparation, the *known* entangled state of 2 qubits is sent encoded in 2 bits. Neither remote preparation protocol requires BSA.

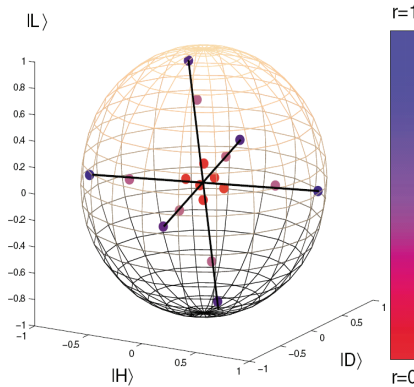


Figure 5.2: Remotely prepared states shown in the Poincaré sphere. The distance of the remotely prepared state from the origin (purity r) is indicated by its color: red —> mixed ($r = 0$), blue —> pure ($r = 1$). Lines are drawn along the data to guide the eye. Figure from Ref. [98].

In a project lead by a former group member, N. A. Peters, we demonstrated RSP with full control of the three parameters required to prepare *arbitrary* single-qubit states [98]. Specifically, arbitrary mixed-state RSP was achieved by measuring arbitrary polarizations of one photon of a polarization-entangled pair. We also derived bounds on the states that may be remotely prepared using arbitrary two-qubit entangled resources.

In detail, for our RSP, Bob (1) and Alice (2) share a two-photon Bell-state: $\Phi^+ \equiv (|H_1 H_2\rangle + |V_1 V_2\rangle)/\sqrt{2} \equiv (|D_1 D_2\rangle + |A_1 A_2\rangle)/\sqrt{2}$, where $|D\rangle \equiv (|H\rangle + |V\rangle)/\sqrt{2}$ and $|A\rangle \equiv (|H\rangle - |V\rangle)/\sqrt{2}$. An arbitrary pure state $\Psi(\theta, \phi) \equiv \cos \theta |D\rangle + e^{i\phi} \sin \theta |A\rangle$ can be prepared if Bob acts on his photon with a unitary transformation followed by a projection into $\langle D|$ [$\langle A|$]. Explicitly, after Bob's unitary

$$|D_1\rangle \rightarrow |\zeta_1(\theta, \phi)\rangle \equiv \cos \theta |D_1\rangle - e^{-i\phi} \sin \theta |A_1\rangle, \quad |A_1\rangle \rightarrow |\zeta_1^\perp(\theta, \phi)\rangle, \text{ with } \langle \zeta^\perp | \zeta \rangle = 0,$$

the joint state becomes

$$\Phi^+ \rightarrow [|\zeta_1(\theta, \phi) D_2\rangle + |\zeta_2^\perp(\theta, \phi) A_2\rangle] / \sqrt{2} \equiv [|D_1 \zeta_2(\theta, \phi)\rangle + |A_1 \zeta_2^\perp(\theta, \phi)\rangle] / \sqrt{2}.$$

Finally, when Bob's outcome is $|D\rangle$ [$|A\rangle$], Alice's qubit is in the state $\Psi(\theta, \phi)$ [$\Psi^\perp(\theta, \phi)$]. Any state lying on a predetermined great circle on the Poincaré sphere can be prepared with 100% efficiency by Bob, if he tells Alice when to perform $\Psi^\perp(\theta, \phi) \rightarrow \Psi(\theta, \phi)$ (in one bit). However, arbitrary states can only be prepared with 50% efficiency (*e.g.*, only when the outcome is $|D\rangle$) because of the impossibility of a universal NOT operation on arbitrary qubit states [99]. Figure 5.2 shows the

states we remotely prepared experimentally, including mixed states.

5.2 Remote entangled-state preparation

RSP can be extended to remotely prepare two-qubit states, even entangled states. Here, we will show how we can remotely prepare single-photon two-qubit states using hyperentanglement. Specifically, spin-orbit Bell-states (locally “entangled” states) will be remotely prepared in a protocol we call remote entangled-state preparation (RESP). In RESP, Alice and Bob share a hyperentangled pair, for example, in the state $\Phi_{\text{pol}}^+ \otimes \Psi_{\text{spa}}^+$. As shown before (Eq. 3.4), this state can be written in the single-photon basis as

$$\Phi_{\text{spin}}^+ \otimes \Psi_{\text{orbit}}^+ = \frac{1}{2} (\phi_1^+ \otimes \psi_2^+ + \phi_1^- \otimes \psi_2^- + \psi_1^+ \otimes \phi_2^+ + \psi_1^- \otimes \phi_2^-). \quad (5.1)$$

Now, if Bob measures his photon (1) with a spin-orbit BSA (Fig. 3.2), the state of Alice’s photon (2) is one of the four spin-orbit Bell states ψ_2^\pm, ϕ_2^\pm (Eq. 3.3) according to Bob’s outcome ϕ_1^\pm, ψ_1^\pm . Any of Alice’s Bell states can then be transformed to any other by one of four unitary transformations on one DOF¹, *e.g.*, ϕ_2^+ , using polarization,

$$\phi_2^+ \xrightarrow{\mathbb{1}} \phi_2^+, \quad \phi_2^+ \xrightarrow{V \leftrightarrow -V} \phi_2^-, \quad \phi_2^+ \xrightarrow{H \leftrightarrow V} \psi_2^+, \quad \text{and} \quad \phi_2^+ \xrightarrow{H \leftrightarrow V, V \leftrightarrow -V} \psi_2^-.$$

Therefore, Bob can turn Alice’s outcome into the desired state by letting her know the required unitary transformation in 2 bits (as illustrated in Fig. 5.1). Bob thus remotely prepares Alice’s single-photon in a predetermined spin-orbit Bell-state.

Experimentally, we have implemented RESP using our spin-orbit BSA, and tomographically reconstructed the remotely prepared states. The tomographic measurements are similar to those used for hyperentangled states, but in this case applied only to Alice’s photon, *e.g.*, $|Dh\rangle_2$, and $|Al\rangle_2$. Figure 5.3 shows the calculated density matrices of the four, remotely prepared, spin-orbit Bell-states. To quantify the quality of the process, we indicate the calculated tangle, linear entropy and fidelity with the target state for each remotely prepared entangled state.

Note that our protocol is essentially entanglement swapping. However, instead of swapping the entanglement between two pairs of particles, here the swapping occurs between degrees of freedom. The spin and orbit DOF of one particle become entangled without local interaction. The high quality

¹Essentially, this is the idea behind hyperentanglement-assisted dense coding.

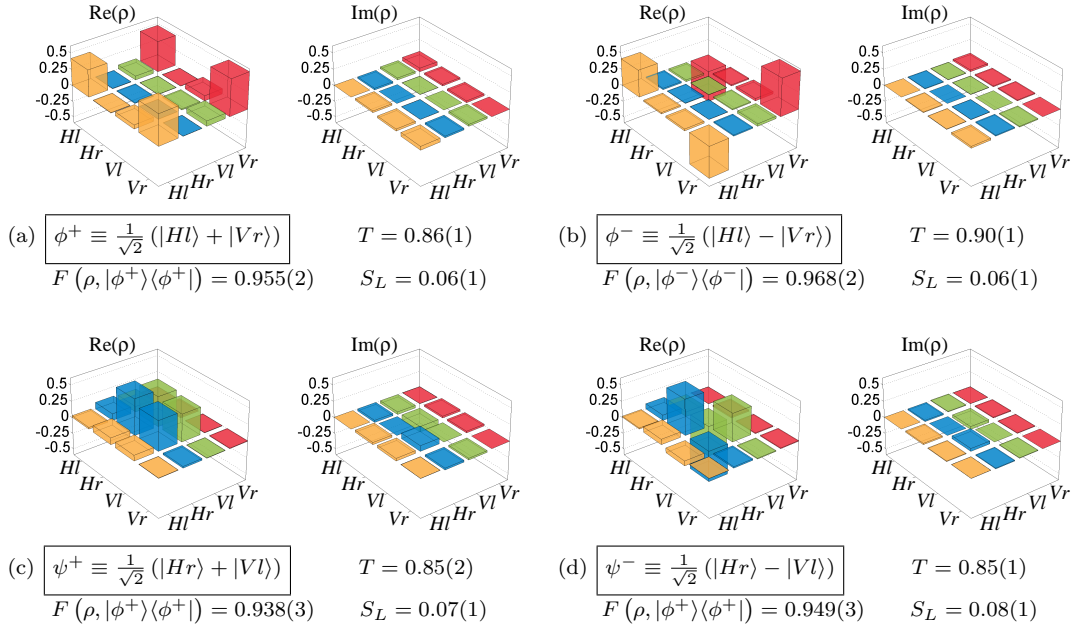


Figure 5.3: Experimental density matrices of remotely prepared entangled states.

Table 5.1: Visibility in the D/A basis of remotely prepared spin-orbit Bell-states.

State	Visibility in D/A basis
ϕ^+	0.94(1)
ϕ^-	0.96(1)
ψ^+	0.91(1)
ψ^-	0.93(1)

of our scheme can be appreciated if we compare the previously reported visibility of 82% [100] with ours ², at least to 91% (see Table 5.1).

5.3 Remote preparation of arbitrary single-photon spin-orbit states

In the previous section, we discussed the remote preparation of single-photon entangled states. Now we ask, Can Bob remotely prepare *arbitrary* pure states $\Psi_2(a, b, c, d) = a\phi_2^+ + b\phi_2^- + c\psi_2^+ + d\psi_2^-$?

²The visibility of the state described by the density matrix ρ in the basis of the states $|\lambda\rangle = (|\chi_1\rangle + |\chi_2\rangle)/\sqrt{2}$ and $|\bar{\lambda}\rangle = (|\chi_1\rangle - |\chi_2\rangle)/\sqrt{2}$ is $\mathcal{V} = 2\text{Re}(\langle\chi_1|\rho|\chi_2\rangle)$, see Ref. [101]. Note that the visibility in the D/A basis ($|\chi_1\rangle = |H\rangle$, $|\chi_2\rangle = |V\rangle$) is the same in the L/R basis, where $|\chi_1\rangle = |H\rangle$, $|\chi_2\rangle = i|V\rangle$.

The answer is yes. Consider the POVM constructed by the following Kraus operators [77],

$$\begin{aligned} F_1 &= a|\phi^+\rangle_1\langle\phi^+| + b|\phi^-\rangle_1\langle\phi^-| + c|\psi^+\rangle_1\langle\psi^+| + d|\psi^-\rangle_1\langle\psi^-|, \\ F_2 &= b|\phi^+\rangle_1\langle\phi^+| + c|\phi^-\rangle_1\langle\phi^-| + d|\psi^+\rangle_1\langle\psi^+| + a|\psi^-\rangle_1\langle\psi^-|, \\ F_3 &= c|\phi^+\rangle_1\langle\phi^+| + d|\phi^-\rangle_1\langle\phi^-| + a|\psi^+\rangle_1\langle\psi^+| + b|\psi^-\rangle_1\langle\psi^-|, \\ F_4 &= d|\phi^+\rangle_1\langle\phi^+| + a|\phi^-\rangle_1\langle\phi^-| + b|\psi^+\rangle_1\langle\psi^+| + c|\psi^-\rangle_1\langle\psi^-|. \end{aligned}$$

This set is indeed a POVM: F_i 's are positive by construction, and by normalization of the state $\Psi_2(a, b, c, d)_2$, they satisfy the completeness relation $\sum_i F_i^\dagger F_i = \mathbb{1}$.

Suppose Bob's POVM measurement gives the outcome F_3 –the joint state in Eq. 5.1 then becomes

$$a\phi_1^+ \otimes \phi_2^+ + b\phi_1^- \otimes \phi_2^- + c\psi_1^+ \otimes \psi_2^+ + d\psi_1^- \otimes \psi_2^-.$$

Next, we split F_3 into the four outcomes

$$\textcircled{1} \sim (|H\rangle + V\rangle)|l\rangle_2, \quad \textcircled{2} \sim (|H\rangle - V\rangle)|l\rangle_2, \quad \textcircled{3} \sim (|H\rangle + V\rangle)|r\rangle_2, \quad \text{and} \quad \textcircled{4} \sim (|H\rangle - V\rangle)|r\rangle_2$$

(e.g., with an OAM splitter and a PBS@45°). If the outcome is $\textcircled{1}$, Alice's photon will be projected into the state $\Psi_2(a, b, c, -d) = a\phi_2^+ + b\phi_2^- + c\psi_2^+ - d\psi_2^-$. Similarly, the other outcomes $\textcircled{2}$, $\textcircled{3}$, and $\textcircled{4}$ give $\Psi_2(a, b, c, d)$ with a phase error, which can be corrected with 2 bits (one of four phase errors). Furthermore, for the other POVM outcomes $F_{i \neq 3}$, the state is a permutation of the spin-orbit states, and again, Bob can send 2 bits to Alice to correct the state.

Thus, the protocol can remotely prepare any spin-orbit state $\Psi_2(a, b, c, d)$ with 4 bits of classical communication and two entangled pairs of qubits or e-bits³. We still need to find a linear optical implementation of such a POVM.

5.3.1 A 4-parameter family of spin-orbit Bell-states

We can readily prepare a four-parameter family of states by acting on Bob's photon polarization and implementing a modified spin-orbit BSA. Alice and Bob start sharing the hyperentangled state

³In principle, however, the *asymptotic* classical communication cost is 2 bits according to Ref. [97].

$\Phi_{\text{pol}}^+ \otimes \Psi_{\text{spa}}^+$. Bob then applies to his photon the polarization unitary:

$$\begin{aligned} |H\rangle &\longrightarrow \cos \theta |H\rangle + e^{i\eta} \sin \theta |V\rangle \\ |V\rangle &\longrightarrow e^{i\phi} (\sin \theta |H\rangle - e^{i\eta} \cos \theta |V\rangle) \end{aligned} \quad (5.2)$$

or, $e^{i(\eta+\phi)/2} R_z(\eta) R_y(2\theta) R_z(\phi)$, in terms of the Bloch rotation operators [77]. Next, Bob measures his photon with a “rotated” spin-orbit BSA:

$$\begin{aligned} \phi_1^+(\alpha) &\equiv \cos \alpha |Hr\rangle_1 + \sin \alpha |Vl\rangle_1 \\ \phi_1^-(\alpha) &\equiv \sin \alpha |Hr\rangle_1 - \cos \alpha |Vl\rangle_1 \\ \psi_1^+(\beta) &\equiv \cos \beta |Hl\rangle_1 + \sin \beta |Vr\rangle_1 \\ \psi_1^-(\beta) &\equiv \sin \beta |Hl\rangle_1 - \cos \beta |Vr\rangle_1. \end{aligned}$$

Such a measurement consists of a spin-orbit BSA, as shown in Fig. 3.2, in which the last polarization measurement is done at the angle α (β) instead of 45° for the ϕ^\pm (ψ^\pm) output.

Taking into account the unitary operation on polarization and the “rotated” spin-orbit BSA, we can rewrite the shared state as:

$$\begin{aligned} \Phi_{\text{spin}}^+ \otimes \Psi_{\text{oam}}^+ &\longrightarrow \phi_1^+(\alpha) \otimes \phi_2^+(\alpha, \eta, \theta, \phi) + \\ &\quad \phi_1^-(\alpha) \otimes \phi_2^-(\alpha, \eta, \theta, \phi) + \\ &\quad \psi_1^+(\beta) \otimes \psi_2^+(\beta, \eta, \theta, \phi) + \\ &\quad \psi_1^-(\beta) \otimes \psi_2^-(\beta, \eta, \theta, \phi), \end{aligned}$$

where Bob’s possible outcomes $\phi_1^\pm(\alpha)$ or $\psi_1^\pm(\beta)$ determine Alice’s state:

$$\begin{aligned} \phi_2^+(\alpha, \eta, \theta, \phi) &\equiv \cos \alpha |\Xi, r\rangle + e^{i\eta} \sin \alpha |\Xi^\perp, l\rangle \\ \phi_2^-(\alpha, \eta, \theta, \phi) &\equiv \sin \alpha |\Xi, r\rangle - e^{i\eta} \cos \alpha |\Xi^\perp, l\rangle \\ \psi_2^+(\beta, \eta, \theta, \phi) &\equiv \cos \beta |\Xi, l\rangle + e^{i\eta} \sin \beta |\Xi^\perp, r\rangle \\ \psi_2^-(\beta, \eta, \theta, \phi) &\equiv \sin \beta |\Xi, l\rangle - e^{i\eta} \cos \beta |\Xi^\perp, r\rangle, \end{aligned}$$

with the polarization state $|\Xi\rangle$ given by

$$|\Xi\rangle \equiv \cos \theta |H\rangle - e^{i\phi} \sin \theta |V\rangle$$

$$|\Xi^\perp\rangle \equiv \sin \theta |H\rangle + e^{i\phi} \cos \theta |V\rangle.$$

The states in this 4-parameter family have the remarkable property that their transverse polarization profiles are not uniform. For various parameter values, the states are shown in Table 5.2, and their transverse polarization profiles in Fig. 5.4. We are currently exploring their potential applications.

Table 5.2: Two-qubit remotely prepared states as a function of Bob's parameters.

Bob's parameters				Bob's outcome			
α	η	θ	ϕ	ϕ_1^+	ϕ_1^-	ψ_1^-	ψ_1^+
Alice's remotely prepared state:							
0	*	0	*	$ Hr\rangle$	$ Vl\rangle$	$ Hl\rangle$	$ Vr\rangle$
0	*	$\pi/4$	0	$ Dr\rangle$	$ Al\rangle$	$ Dl\rangle$	$ Ar\rangle$
0	*	$\pi/4$	$\pi/2$	$ Lr\rangle$	$ Rl\rangle$	$ Ll\rangle$	$ Rr\rangle$
$\pi/4$	*	0	0	$ Hr\rangle + Vl\rangle$	$ Hr\rangle - Vl\rangle$	$ Hl\rangle + Vr\rangle$	$ Hl\rangle - Vr\rangle$
$\pi/4$	*	0	$\pi/2$	$ Hr\rangle + i Vl\rangle$	$ Hr\rangle - i Vl\rangle$	$ Hl\rangle + i Vr\rangle$	$ Hl\rangle - i Vr\rangle$
$\pi/4$	0	$\pi/4$	0	$ Ar\rangle + Dl\rangle$	$ Ar\rangle - Dl\rangle$	$ Al\rangle + Dr\rangle$	$ Al\rangle - Dr\rangle$
$\pi/4$	0	$\pi/4$	$\pi/2$	$ Rr\rangle + Ll\rangle$	$ Rr\rangle - Ll\rangle$	$ Rl\rangle + Lr\rangle$	$ Rl\rangle - Lr\rangle$
				$= Hh\rangle - Vv\rangle$	$= Hv\rangle + Vh\rangle$	$= Hh\rangle + Vv\rangle$	$= Hv\rangle - Vh\rangle$
$\pi/4$	$\pi/2$	$\pi/4$	0	$ Ar\rangle + i Dl\rangle$	$ Ar\rangle - i Dl\rangle$	$ Al\rangle + i Dr\rangle$	$ Al\rangle - i Dr\rangle$
$\pi/4$	$\pi/2$	$\pi/4$	$\pi/2$	$ Rr\rangle + i Ll\rangle$	$ Rr\rangle - i Ll\rangle$	$ Rl\rangle + i Lr\rangle$	$ Rl\rangle - i Lr\rangle$

Of outstanding interest is the family of states $\frac{1}{\sqrt{2}}(|Rr\rangle \pm |Ll\rangle)$ and $\frac{1}{\sqrt{2}}(|Rl\rangle \pm |Lr\rangle)$ because of their potentially useful polarization profiles. The state with radial polarization profile $|Rr\rangle - |Ll\rangle = |Hv\rangle + |Vh\rangle$, in particular, was first realized using a setup similar to our spin-orbit BSA in 1990 [102] as a test bed for use in the focusing of electrons using a laser (due to an effect known as inverse Cerenkov effect [103]). A more recent application is the realization of a focused spot size significantly smaller than possible with linear polarization [104]. Theoretically, such states have also been shown to enable the largest possible longitudinal electric field component in the focal point of a lens [105], as well as the most efficient mode converter for light-atom coupling in free space [106, 107] (although with a radial amplitude distribution different from ours and an elaborated temporal pulse shape).

Experimentally, we have remotely prepared this family of states. We sent Bob's photon thru liquid crystals set to implement the required polarization unitary, $|H\rangle \rightarrow |D\rangle$, $|V\rangle \rightarrow i|A\rangle$ (see Eq. 5.3 and Table 5.2). Next, this photon was measured with a spin-orbit BSA as in the previous chapter.

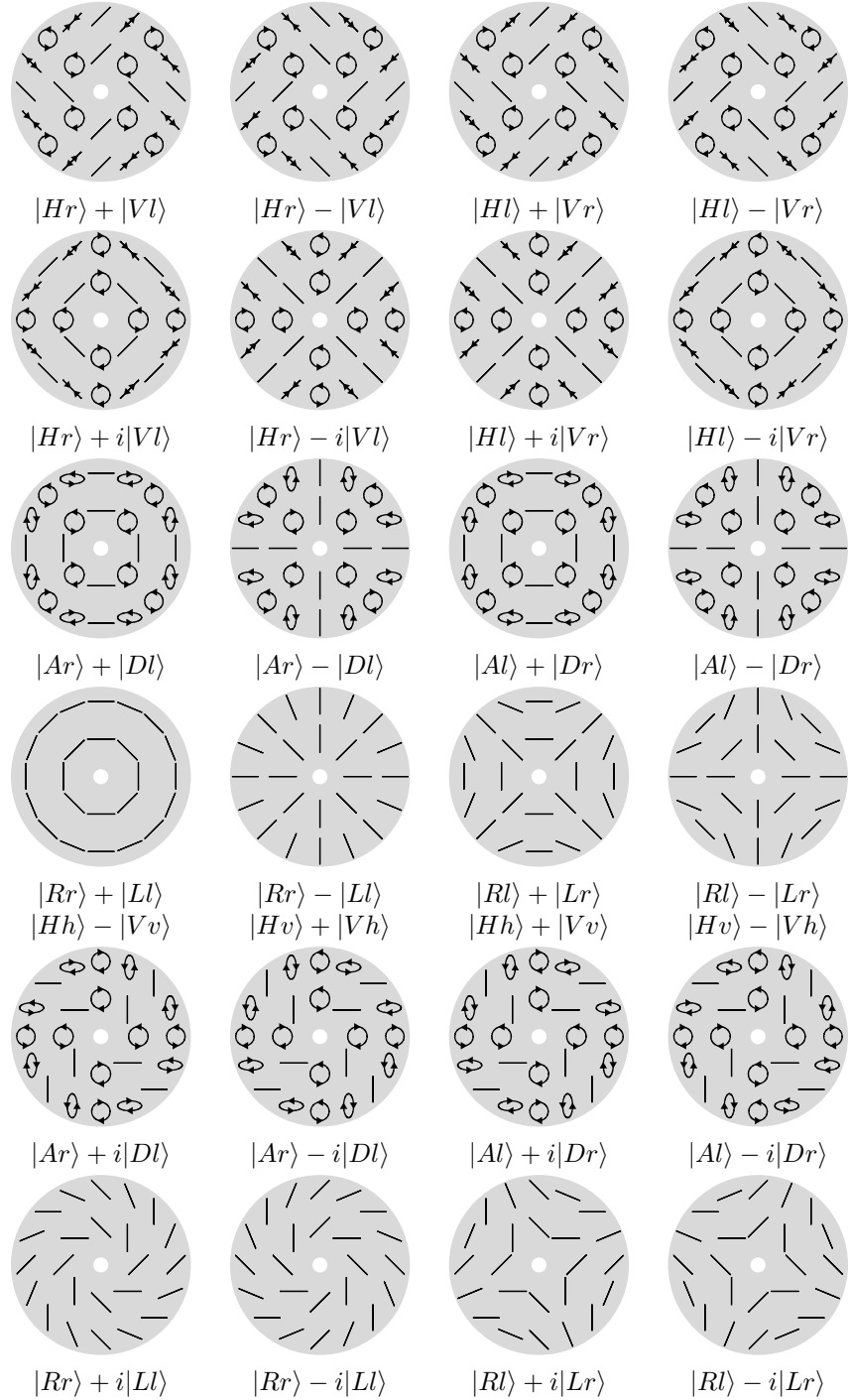


Figure 5.4: Spin-orbit transverse polarization profiles for some of the states shown in Table 5.2.

Finally, to quantify the remote preparation of Alice's photon, we tomographically reconstructed the states and found the density matrices shown in Fig. 5.5.

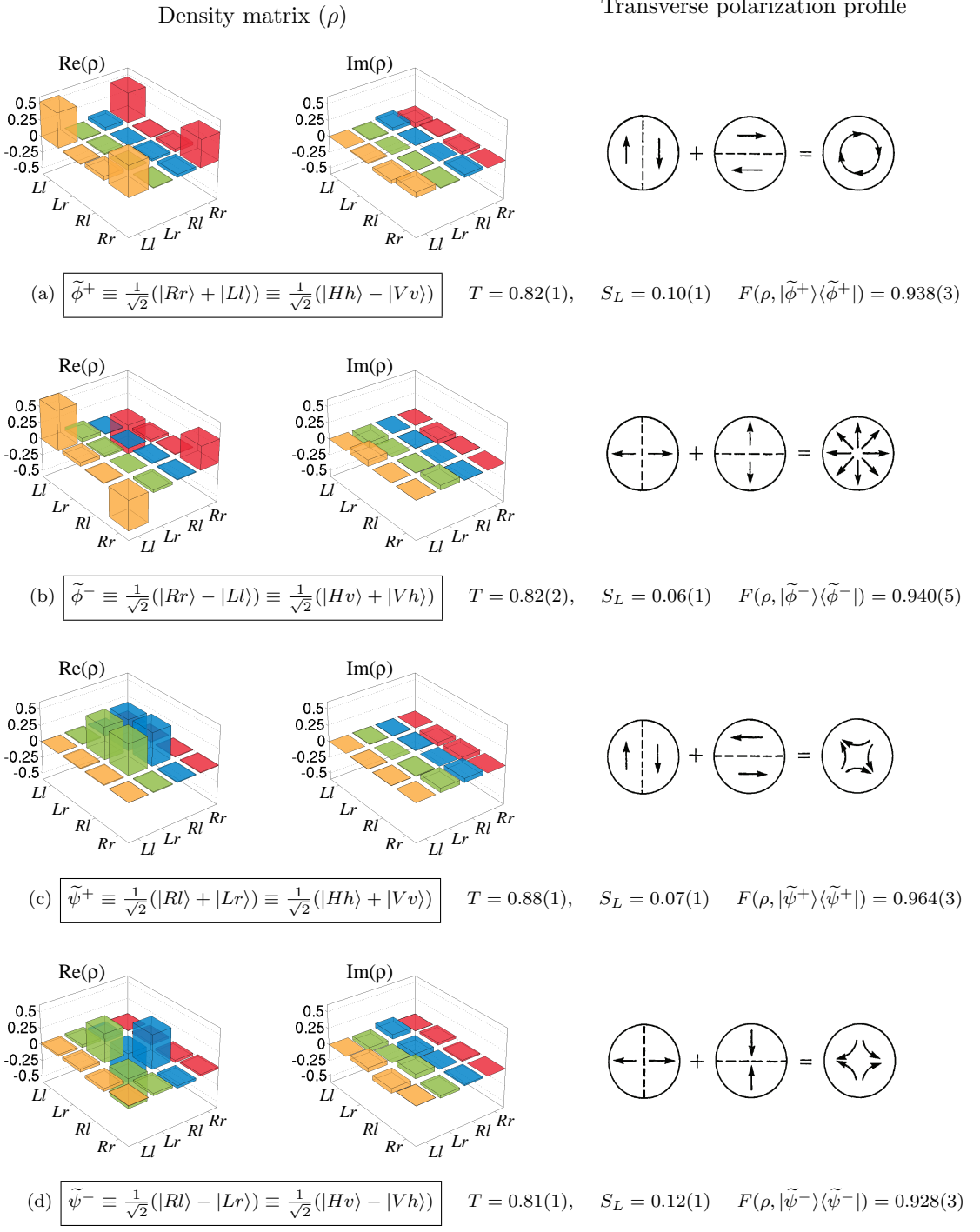


Figure 5.5: Left: Experimental density matrices of remotely prepared “radial-polarization” states. Right: transverse polarization profile of each mode and its components (from Ref. [102]). The π -phase shift between the lobes of the Hermite-Gauss modes is evident in the polarization direction.

5.3.2 Remote preparation of two-qubit mixed states

Further control of the protocol can be shown by remotely preparing *mixed* states. Bob, then, needs to induce decoherence on Alice’s photon. One way to achieve decoherence is by entangling the quantum system to another of its DOFs, which is then traced over. This technique has previously enabled the generation of mixed polarization states [101] and remotely prepared mixed states [98]. In RSP, for example, Bob couples his photon’s polarization and frequency DOFs followed by a frequency-insensitive measurement [98, 101], preparing Alice’s photon in a mixed state. For RESP, similarly, Bob can couple the OAM and frequency DOF by detuning the interferometer in the spin-orbit BSA. After a frequency-insensitive measurement, Bob measures spin-orbit mixed states and prepares Alice’s photon in a mixed spin-orbit mixed state.

Alternatively, we can trace over Bob’s photon spin and/or orbital DOF or a subspace of them. For example, consider the spin-orbit BSA without either PBS@45° (see Fig. 3.2); then, instead of the 4 outcomes ϕ_1^+ , ϕ_1^- , ψ_1^+ , and ψ_1^- , only 2 outcomes will be now possible, ϕ_1 and ψ_1 . Consequently, when a pair in the state of Eq. 5.1 is shared and Bob detects a photon in ϕ_1 (ψ_1), Alice’s photon is in the classically correlated state $\sim |\psi^+\rangle_2\langle\psi^+| + |\psi^-\rangle_2\langle\psi^-|$ ($\sim |\phi^+\rangle_2\langle\phi^+| + |\phi^-\rangle_2\langle\phi^-|$). In addition, using the polarization unitary in Eq. 5.3, we can also prepare classically correlated states in other bases.

Finally, if both spin and OAM of Bob’s photon is ignored, Alice’s photon is left in a completely mixed state. We experimentally prepared such classically correlated and completely mixed states, whose reconstructed density matrices are shown in Fig. 5.6.

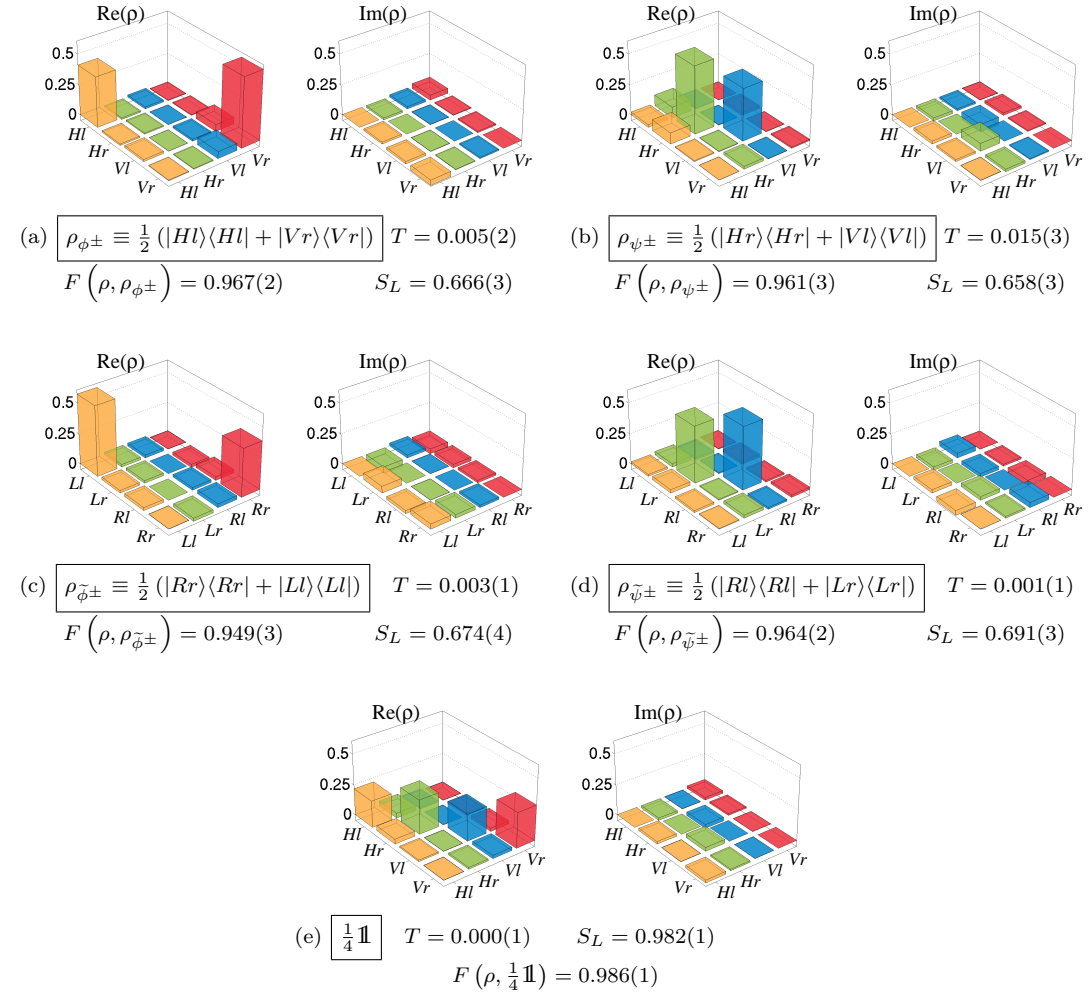


Figure 5.6: Experimental density matrices of remotely prepared two-qubit mixed states: (a-d) Classically correlated states in different bases realized by tracing over Bob's photon spin-orbit Bell states, and (e) Completely mixed state realized by tracing over Bob's photon.

Chapter 6

Outlook

6.1 Bound entanglement

Since the inception of the EPR pair, few quantum states have attracted as much interest as bound entangled states (BE). They offer novel applications and properties that challenge our fundamental understanding of entanglement as a resource in quantum information processing. Most quantum information protocols rely on a source of pure entangled pairs. For example, teleportation and dense coding require them to achieve faithful transmission of information through noisy channels. To this end, distillation was proposed: a process for preparing entangled pairs of arbitrarily high purity by applying only local operations and classical communication to a supply of states that have gone through a noisy channel (mixed states) [108, 109], as schematically shown in Fig. 6.1. Presumably, if a physical resource exists, it can be extracted or distilled; this is certainly true with energy, isotope separation, etc. Surprisingly, for entanglement this is not always the case. There is a class of mixed entangled states, known as bound, from which no pure entanglement can be

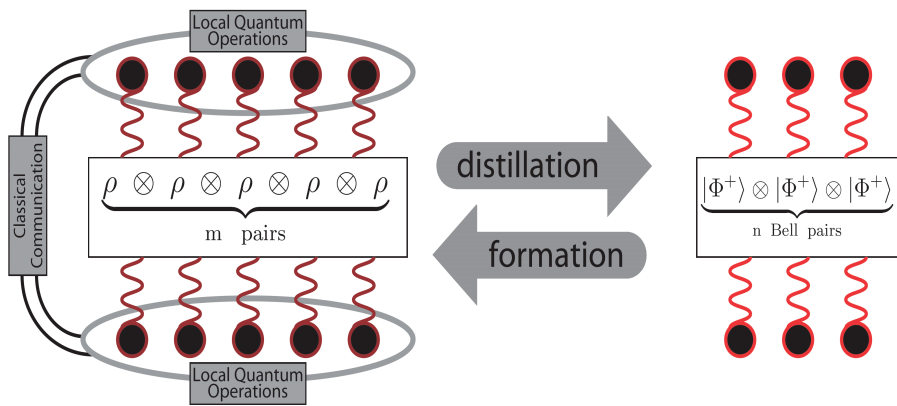


Figure 6.1: Distillation and formation of entanglement as complementary processes. Distillation quantifies how many pure Bell pairs could be extracted from a large number of non-maximally entangled, possibly mixed, states ρ . Entanglement of formation quantifies how many pure Bell states are needed to copy or prepare many copies of ρ using local operations and classical communication.

distilled [110]. Such states have never been observed, and are so intriguing that their existence in nature has been questioned. Their special properties have found several proposed applications in quantum communication, for example, to enable remote quantum information concentration [111], to distill arbitrarily secure keys [112], to improve teleportation fidelity [113], and to enhance quantum secret sharing [114]. Bound entanglement has escaped an experimental realization because a Hilbert space of at least $2 \otimes 4$ or $3 \otimes 3$ dimensions is required, as well as a set of parameters hard to achieve experimentally [115]. For example, one of the smallest BE states in $3 \otimes 3$ has the density matrix

$$\varrho_a = \frac{1}{8a+1} \begin{pmatrix} a & 0 & 0 & 0 & a & 0 & 0 & 0 & a \\ 0 & a & 0 & 0 & 0 & 0 & 0 & 0 & 0 \\ 0 & 0 & a & 0 & 0 & 0 & 0 & 0 & 0 \\ 0 & 0 & 0 & a & 0 & 0 & 0 & 0 & 0 \\ a & 0 & 0 & 0 & a & 0 & 0 & 0 & a \\ 0 & 0 & 0 & 0 & 0 & a & 0 & 0 & 0 \\ 0 & 0 & 0 & 0 & 0 & 0 & \frac{1+a}{2} & 0 & \frac{\sqrt{1-a^2}}{2} \\ 0 & 0 & 0 & 0 & 0 & 0 & 0 & a & 0 \\ a & 0 & 0 & 0 & a & 0 & \frac{\sqrt{1-a^2}}{2} & 0 & \frac{1+a}{2} \end{pmatrix},$$

with $0 < a < 1$ [110].

Increasingly fascinating is a particular class of four-party BE states, from which a pure maximally entangled state can be unlocked [116]: a joint measurement of any two parties enables the other two to become pure maximally entangled without ever coming together. The simplest unlockable state, known as the Smolin state and living in a $2 \times 2 \times 2 \times 2$ -dimensional Hilbert space, is an equally probable mixture of the maximally entangled states:

$$\text{Smolin state} = \frac{1}{2} (| \Phi^+ \rangle_{AB} \langle \Phi^+ | \otimes | \Phi^+ \rangle_{CD} \langle \Phi^+ | + | \Phi^- \rangle_{AB} \langle \Phi^- | \otimes | \Phi^- \rangle_{CD} \langle \Phi^- | + | \Psi^+ \rangle_{AB} \langle \Psi^+ | \otimes | \Psi^+ \rangle_{CD} \langle \Psi^+ | + | \Psi^- \rangle_{AB} \langle \Psi^- | \otimes | \Psi^- \rangle_{CD} \langle \Psi^- |).$$

In contemplating attempting to create such a state, we must question whether it is located at an isolated and unstable point in Hilbert space, which would likely make it impossible to realize in practice. Recent studies [114] and our own simulations, show that the Smolin state lies in fact within a sizeable volume of BE states, and its properties are preserved in the presence of noise; thus, such a state should be realizable in a practical experiment.

The Smolin state can be created with hyperentangled photons, identifying AB with the polarization degrees of freedom and CD with the spatial modes. We have shown in previous chapters how we generated and completely characterized the state $|\Phi^+\rangle \otimes |\Phi^+\rangle$, the first term in the Smolin state composition. Similarly, by using type-I SPDC, we can create the other constituent maximally hyperentangled states [34, 36], allowing us to generate the Smolin state. In our scheme shown in Fig. 6.2, we first prepare a 351-nm continuous-wave laser in a state of diagonal polarization ($|D\rangle$) and Hermite-Gauss ($m = 0, n = 2$) spatial profile at 45° :

$$|D\rangle \otimes |\text{HG}_{02}^{@45^\circ}\rangle = |D\rangle \otimes (|\text{HG}_{02}\rangle + |\text{HG}_{20}\rangle) / \sqrt{2}.$$

Second, we entangle the polarization and spatial mode with a technique previously demonstrated (for $|D\rangle \otimes |\text{HG}_{01}^{@45^\circ}\rangle$, see Appendix D), which will essentially implement a CNOT gate, thereby generating the pump-photon entangled state $(|H, \text{HG}_{02}\rangle + |V, \text{HG}_{20}\rangle) / \sqrt{2}$. At this point, a half-wave plate rotates the state into $(|D, \text{HG}_{02}\rangle + |A, \text{HG}_{20}\rangle) / \sqrt{2}$, where $|A\rangle$ labels anti-diagonal polarization. Third, we decohere in the polarization basis [101, 117], generating the mixed state

$$\frac{1}{2} \left(|H, \text{HG}_{02}^{@45^\circ}\rangle \langle H, \text{HG}_{02}^{@45^\circ}| + |V, \text{HG}_{02}^{@-45^\circ}\rangle \langle V, \text{HG}_{02}^{@-45^\circ}| \right).$$

Just before pumping the crystals the state is rotated into

$$\frac{1}{2} \left(|D, \text{HG}_{02}^{@45^\circ}\rangle \langle D, \text{HG}_{02}^{@45^\circ}| + |A, \text{HG}_{02}^{@-45^\circ}\rangle \langle A, \text{HG}_{02}^{@-45^\circ}| \right).$$

Subsequently, the decohered beam passes through two BBO crystals, creating, respectively, the first two constituents of the Smolin state:

$$\frac{1}{2} \left(|\Phi^+\rangle_{AB} \langle \Phi^+| \otimes |\Phi^+\rangle_{CD} \langle \Phi^+| + |\Phi^-\rangle_{AB} \langle \Phi^-| \otimes |\Phi^-\rangle_{CD} \langle \Phi^-| \right).$$

A second pass back through the same crystals is followed by one-particle transformations in the down-conversion, generating

$$\frac{1}{2} \left(|\Psi^+\rangle_{AB} \langle \Psi^+| \otimes |\Psi^+\rangle_{CD} \langle \Psi^+| + |\Psi^-\rangle_{AB} \langle \Psi^-| \otimes |\Psi^-\rangle_{CD} \langle \Psi^-| \right),$$

which combined with the first constituents, produces the Smolin state. If necessary, a source of white noise can be added to compensate for imperfection in the entanglement balance and lead the

state to the bound region [114]. The density matrix of the state produced in this manner can then be obtained by quantum state tomography.

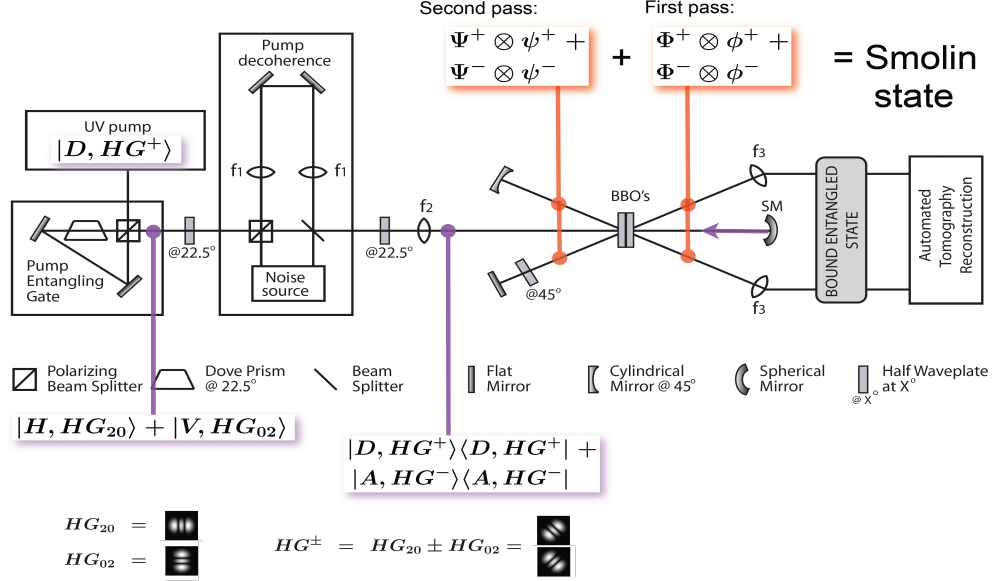


Figure 6.2: Experimental setup to produce and characterize bound entangled states. Lenses labeled f_1 match the modes in the interferometer labeled “pump decoherence”.

Bound entanglement can be characterized by the negativity¹ (N) entanglement measure [46], with a value greater than 0 for entangled and 0 for product and maximally mixed states. For the Smolin state this measure can be considered under two classes of partitions [118]: 2:2 with AC:BD and 1:3 with A:CBD (and permutations). Bound entanglement occurs when the 2:2 partition shows no entanglement, $N = 0$, while the 1:3 partitions are entangled, $N > 0$. From the measured density matrix we can find the negativities and demonstrate that bound entanglement exists. In addition, the entanglement can be unlocked with a spin-orbit BSA acting on AC, leaving BD in an entangled state. A consequence of the fact that permuting parties B and C of the Smolin state leaves the state again in the Smolin form, as shown in Ref. [116],

$$\frac{1}{2}(|\Phi^+\rangle_{AC}\langle\Phi^+| \otimes |\Phi^+\rangle_{BD}\langle\Phi^+| + |\Phi^-\rangle_{AC}\langle\Phi^-| \otimes |\Phi^-\rangle_{BD}\langle\Phi^-| + |\Psi^+\rangle_{AC}\langle\Psi^+| \otimes |\Psi^+\rangle_{BD}\langle\Psi^+| + |\Psi^-\rangle_{AC}\langle\Psi^-| \otimes |\Psi^-\rangle_{BD}\langle\Psi^-|).$$

Bound entanglement, in particular, the Smolin state, has some applications that surpass or are unrealizable with maximally entangled states [114]:

¹The negativity is a value used to quantify the degree of separability of states and defined as twice the absolute sum of negative eigenvalues of the partial transpose of the density matrix with respect to some bipartite partitioning.

- Remote quantum information concentration [111], the reverse of quantum telecloning: Quantum information originally from a single qubit, but now distributed into three separate qubits, is remotely concentrated back to a single qubit via an initially shared BE state, without performing any global operations. Using this protocol a secret shared between spatially separated parties can be remotely transmitted to another party.
- Bipartite activation. Bound entanglement assists teleportation by improving the fidelity of the teleported states beyond what is possible without bound entanglement [113]. Whether the Smolin state enables this activation is unknown at this time.
- Quantum secret sharing, a mechanism for splitting a message into several parts so that no subset of parts is sufficient to read the message, but the entire set is [119]. The intrinsic unlockability property of the Smolin state might surpass the limitations of previous experimental realizations of quantum secret sharing [120, 121, 122].
- Maximal Bell violation [123], enabling an optimal solution for 4-party communication complexity problems [124].

6.2 CGLPM Inequality for $d = 4$ with Hyperentanglement

In 2002, Collins, Gisin, Linden, Massar, and Popescu (CGLPM) presented a Bell-type inequality to study the non-locality of 2 qudits [125]. This inequality is a generalization of a CHSH-inequality using only two settings per particle. A paradoxical feature makes this inequality attractive for experimental realization, namely, the quantum state which gives the maximal violation is *not* the maximally entangled state of two qudits [126].

In particular, we consider the CGLPM inequality for a pair of 4-level qudits shared between Alice and Bob. In this case, each party can carry out two possible measurements on them, labelled A_1, A_2 and B_1, B_2 , and each measurement may have 4 possible outcomes: $A_1, A_2, B_1, B_2 = 0, 1, 2, 3$. The inequality then reads

$$I_4 = \sum_{k=0}^1 \left(1 - \frac{2k}{3}\right) \left\{ [P(A_1 = B_1 + k) - P(A_1 = B_1 - k - 1)] + [P(A_1 = B_1 - k) - P(A_1 = B_2 + k + 1)] - [P(A_2 = B_1 + k) - P(A_2 = B_1 - k - 1)] + [P(A_2 = B_2 + k) - P(A_2 = B_2 - k - 1)] \right\} \leq 2,$$

where the P 's are probabilities, and the sums and differences are modulo 4. The family of states with paradoxical features is

$$\Psi(\theta) = (\cos \theta |HH\rangle + \sin \theta |VV\rangle) \otimes \frac{1}{\sqrt{2}} (|hh\rangle + |vv\rangle). \quad (6.1)$$

If the state is maximally entangled, *i.e.*, $\cos \theta = 1/\sqrt{2}$, the violation is larger than the maximal for qubits ($2\sqrt{2}$),

$$I_4^{\text{me}} = I_4(\Psi(\frac{1}{\sqrt{2}})) = 2.8962 = 2\sqrt{2}(1 + 2.4\%)$$

for the measurement settings described later. Surprisingly, using the same measurement settings, the maximal violation occurs for $\cos \theta \approx 0.8041$, where

$$I_4^{\text{max}} = I_4(\Psi(\cos^{-1} 0.8041)) = 2.9727 = I_4^{\text{me}}(1 + 2.6\%) = 2\sqrt{2}(1 + 5.1\%).$$

The state in Eq. 6.1 can be, in principle, easily realized with our hyperentanglement source by tuning the pump polarization to generate the polarization state. For example, the experimentally achieved state closest to the maximally entangled state $\phi^+ \otimes \Phi^+$, reported in Ref. [28], had a Bell parameter calculated from the measured density matrix of $I_4 = 2.826 \approx 2 * \sqrt{2}(1 - 2.5\%)$ –*low* for the quality of states required.

After creating the desired state, Eq. 6.1, we must implement the necessary measurements. The measurement settings are the same for Alice and Bob and can be considered as the four outcomes of a unitary U . This unitary is the product of two unitaries $U = U_\phi \times U_{\text{FT}}$, which do the following,

1. Add a phase in the computational basis, $|Hh\rangle$, $|Vh\rangle$, $|Vv\rangle$, and $|Hv\rangle$, *i.e.*, apply the unitary

$$U_\phi = \begin{pmatrix} 1 & & & \\ & e^{i\phi_1} & & \\ & & e^{i\phi_2} & \\ & & & e^{i\phi_3} \end{pmatrix},$$

where the settings we consider are

	ϕ_1	ϕ_2	ϕ_3	
A_1	0	0	0	
A_2	$\pi/4$	$\pi/2$	$3\pi/4$	(6.2)
B_1	$\pi/8$	$\pi/4$	$3\pi/8$	
B_2	$-\pi/8$	$-\pi/4$	$-3\pi/8$	

2. Mix the four modes with a discrete Fourier transform,

$$U_{\text{FT}} = \frac{1}{2} \begin{pmatrix} 1 & 1 & 1 & 1 \\ 1 & i & -1 & -i \\ 1 & -1 & 1 & -1 \\ 1 & -i & -1 & i \end{pmatrix}$$

Now we propose two ways of measuring these settings. In the first case, we present a four-outcome measurement consisting of two chained interferometers for each party. In the second case, each measurement gives two of the four outcomes and consists of a simple interferometer for each party.

6.2.1 Four-outcome measurement scheme

In Fig. 6.3, we show the measurement setup that Alice and Bob need (one each) to evaluate the CGLPM parameter I_4 . For this scheme, each row of settings of $\phi_{1,2,3}$ in Eq. 6.2 gives four outcomes for I_4 . This scheme consists of two chained interferometers, the first one is similar to the spin-orbit BSA but with a BS instead of PBS, plus embedded liquid crystals. The components shown perform the unitary transformations described next.

- Liquid crystals (LC) add phase shifts in the polarization basis (H, V) : $LC@V(\phi) = \begin{pmatrix} 1 & 0 \\ 0 & e^{i\phi} \end{pmatrix}$, and $LC@H(\phi) = \begin{pmatrix} e^{i\phi} & 0 \\ 0 & 1 \end{pmatrix}$.
- Three waveplates perform the unitaries, in the polarization basis (H, V) , $HWP@22.5^\circ = \begin{pmatrix} 1 & 1 \\ 1 & -1 \end{pmatrix}$, $HWP@45^\circ = \begin{pmatrix} 0 & 1 \\ 1 & 0 \end{pmatrix}$, $QWP_{\text{Alice}}@22.5^\circ = \begin{pmatrix} -1 & -1 \\ i & -i \end{pmatrix}$, and $QWP_{\text{Bob}}@22.5^\circ = \begin{pmatrix} -1 & -1 \\ -i & i \end{pmatrix}$.
- A beam splitter “mixes” modes h and v , written in the spatial mode basis (h, v) , $BS = \begin{pmatrix} 1 & 1 \\ 1 & -1 \end{pmatrix}$.

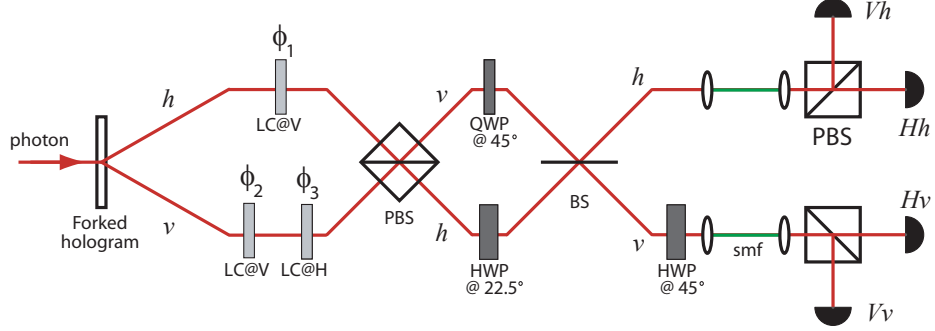


Figure 6.3: Four-outcome measurement scheme for testing a CGLPM-inequality. The label h (v) corresponds to a gaussian mode that was the mode $|l\rangle$ ($|r\rangle$) before the forked hologram (first splitter). LC@X: Liquid crystal applying a phase shift to the X polarization (with respect to the orthogonal polarization), HWP: Half-wave plate, QWP: Quarter-wave plate, BS: Beam splitter, smf: single-mode fiber, and PBS: Polarizing beam-splitter.

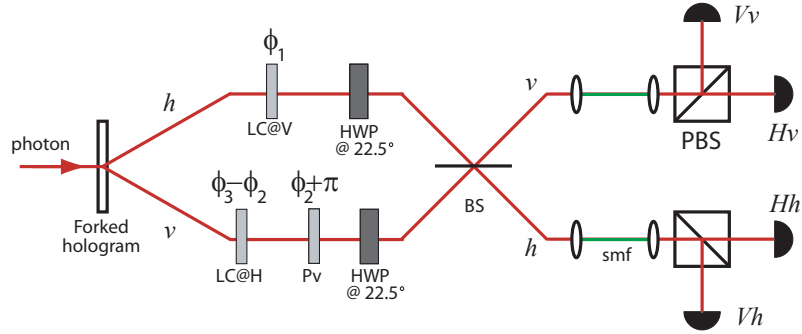


Figure 6.4: Two-outcome measurement scheme for testing a CGLPM-inequality. The label h (v) can be replaced by the \pm -OAM modes $|l\rangle$ ($|r\rangle$) and the first splitter is a forked hologram. LC: Liquid crystal, Pv: interferometer phase (see text), HWP: Half-wave plate, BS: Beam splitter, smf: single-mode fiber, and PBS: Polarizing beam-splitter.

6.2.2 Two-outcome measurement scheme

Since the four-outcome scheme is rather complex, here we propose a simpler scheme that needs two orthogonal measurements for each setting, where each measurement gives two useful outcomes out of four possible. The scheme, shown in Fig. 6.4, consists of an interferometer similar to the spin-orbit BSA, but with a BS instead of PBS, plus embedded liquid crystals and waveplates. Each component performs the following unitary operations.

- Liquid crystals (LC), acting in the polarization basis (H, V), perform a unitary described by $LC@V = \begin{pmatrix} 1 & 0 \\ 0 & e^{i\phi_1} \end{pmatrix}$, and $LC@H = \begin{pmatrix} e^{i(\phi_3-\phi_2)} & 0 \\ 0 & 1 \end{pmatrix}$;

- An interferometer phase on both polarizations in mode v with respect to mode h: $Pv = \begin{pmatrix} e^{i(\phi_2+\pi)} & 0 \\ 0 & e^{i(\phi_2+\pi)} \end{pmatrix}$;
- A pair of half waveplates acts on the polarization of both modes, h and v, before the BS, $HWP@22.5^\circ = \begin{pmatrix} 1 & 1 \\ 1 & -1 \end{pmatrix}$; and
- A beam splitter, which in the spatial mode basis (h, v) is described by $BS = \begin{pmatrix} 1 & 1 \\ 1 & -1 \end{pmatrix}$.

The full transformation $U_{\text{FT}}U_\phi$ is similar to the four-outcome scheme with

$$U_\phi = \begin{pmatrix} 1 & & & \\ & e^{i\phi_1} & & \\ & & e^{i\phi_2} & \\ & & & e^{i\phi_3} \end{pmatrix}, \quad \text{and} \quad U_{\text{FT}} = \begin{pmatrix} 1 & 1 & 1 & 1 \\ 1 & -1 & -1 & 1 \\ 1 & -1 & 1 & -1 \\ 1 & 1 & -1 & -1 \end{pmatrix}. \quad (6.3)$$

The value of the parameters $\phi_{1,2,3}$ for the measurement settings $A_{1,2}, B_{1,2}$ are described in Eq. 6.2. However, looking at all 4 outcomes of this “two-outcome” scheme gives CGLPM parameters lower than desired $I_4^{\text{me}} = 2.483$ and $I_4^{\text{max}} = 2.391$. Notice that both the 2- and 4-outcome schemes measure the same states at the detectors labeled Hh and Vv , corresponding to rows 1 and 3 of $U_{\text{FT}}U_\phi$. However, the measurements differ for detectors Vh and Hv (rows 2 and 4), where the four-outcome scheme has imaginary elements. To detect these outcomes in the two-outcome scheme, Alice does the following phase shifts $\phi_1 \rightarrow \phi_1 + \pi/2$, $\phi_2 \rightarrow \phi_2 + \pi$, and $\phi_3 \rightarrow \phi_3 + 3\pi/2$, while Bob does $\phi_1 \rightarrow \phi_1 + 3\pi/2$, $\phi_2 \rightarrow \phi_2 + \pi$, and $\phi_3 \rightarrow \phi_3 + \pi/2$.

To assess the sensitivity to preparation and measurement of an experimental implementation, we evaluated the CGLPM parameter I_4 as a function of the polarization angle θ of the state $\Psi(\theta)$ (most sensitive preparation parameter) and a phase drift in the interferometer (most sensitive measurement parameter). The results, shown in Fig. 6.5, show a relatively large region of interest, inside the ellipse of $I_4 = 2.896$, where unexpected values of a Bell parameter could be measured. In the model, we assume the drift was the same for both particles. If the drifts are different, they can be compensated by offsetting one interferometer in the opposite direction.

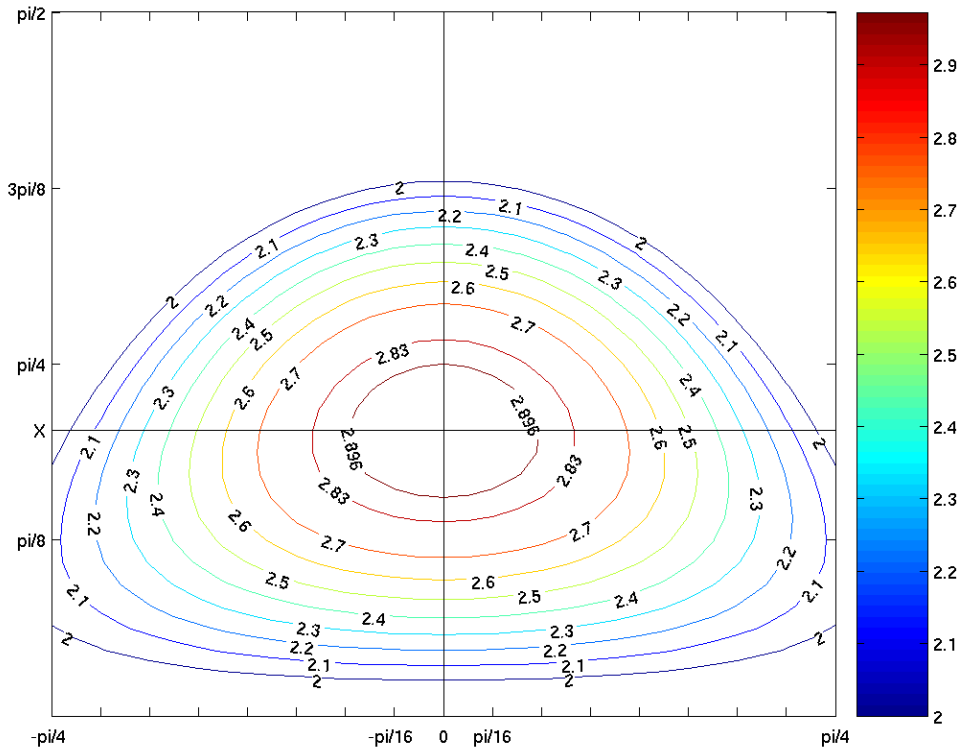


Figure 6.5: CGLPM-parameter (I_4) contours in the plane of the angle θ of Eq. 6.1 (vertical axis) and the interferometer phase drift (horizontal) – a plane of state and measurement precision. Note that the maximum of the CGLMP parameter for a maximally entangled state in 2 dimensions is $2\sqrt{2} \approx 2.828$, and for a maximally entangled state in 4 dimensions $I_4 \approx 2.896$. Unexpectedly, the maximum violation is for the state in Eq. 6.1 with $\cos \theta = 0.8041$, labeled X in the figure.

Appendix A

Holograms

For the characterization of spatial modes and splitting the OAM modes (see Ch. 2), we use binary phase gratings generated by computer. While binary phase gratings have a maximum efficiency of 40.5% into the first diffraction order [127], we experimentally achieved 35%. The best reference for holography is the book by P. Hariharan [127]. Each hologram was a recording of the (binary) interference pattern between the desired field and a reference field. We chose a plane wave as reference field for two reasons, first, its simplicity. Second, since the modes are further filtered by single-mode fibers, which in conjunction with a low in-coincidence population of higher order HG and LG modes of SPDC guarantees good mode projection.

The computer generated holograms were fabricated using silver halide sensitized gelatin on a glass plate¹. The pattern was computer generated [128] and printed on film² using a slide printer at the Beckman Institute.

The following sections are adapted from the original instructions from Photographers formulary (www.photoformulary.com).

A.1 Chemicals

A.1.1 For your chemical safety

Like many household cleaners, chemicals in general should be considered dangerous and must be treated with respect. Please read all the warning labels on each package. It is good practice to use eye goggles, dust mask, apron and rubber gloves when mixing chemicals. While the chemicals have low volatility, working in a ventilated area is recommended.

Although most chemicals in JD-2 are considered non-hazardous by the EPA, the kit does contain small amounts of chemicals that the EPA does consider hazardous.

¹Slavich plates PFG-01, average grain size of 40 nm, spectral sensitivity 600-680 nm, plate dimensions of 63 mm × 63 mm, purchased from www.laserreflections.com

²Kodak Technical Pan, B&W using the standard developing technique with Technidol.

Potassium Dichromate is both toxic and an oxidizer (potential fire hazard). To dispose of excess solid potassium dichromate always washes the solid down the drain with large amounts of water. Never dispose of the solid in a wastebasket. Spillage of a dichromate solution on the skin will cause a chemical burn, which will appear as ulceration. In addition, all chromium compounds are potential carcinogens. In addition, we strongly recommend you use disposable rubber gloves when handling this compound in solutions. Clean all trays and containers thoroughly with water followed by soap and water. Dispose of excess dichromate salts and their solutions down a drain with a large volume of water.

Urea and Ascorbic Acid may irritate the eyes and skin.

Catechol is a toxic central nervous system depressant, methemoglobin former and convulsant; a severe eye, skin, and mucous membrane irritant. It is also a skin sensitizer. Poisoning may affect the liver and kidneys.

Sodium Bisulfate is a skin irritant. Wash skin with lots of running water for 15 minutes. Get immediate medical attention. If swallowed do not induce vomiting. Wear rubber gloves; dust mask, apron, and safety goggles when mixing this solution.

If for any reason you do not wish to assume all risks in using these chemicals, please return them within 30 days for a full refund.

Please contact the University research safety office regarding the proper disposal of darkroom chemicals. Fill a “Request to establish a new waste chemical mixture”, form CWM-TRK-03, for the following mixtures: Mixture #1 Holographic Developer solution, Mixture #2 Holographic bleach solution.

A.1.2 Mixing the stock solutions

The chemicals in the JD-2 kit are used to prepare approximately 1000ml of each of three solutions. You will need to add de-ionized or distilled water, which can be purchased at most local grocery store. It is best to use distilled water that contains no other chemicals although distilled drinking water, which sometimes contains small but negligible amounts of other chemicals, can also be used. Water from your tap generally contains fluoride and other impurities that may reduce the quality of your hologram.

Part A

Chemical	Amount
Cathecol	20 g
Ascorbic Acid	10 g
Sodium Sulfite	10 g
Urea	75 g
ADD Distilled water	1000 ml

Part B

Chemical	Amount
Sodium Carbonate, Anhyd.	60 g
ADD Distilled water	1000 ml

Bleach Solution

Chemical	Amount
Potassium Dichromate	5 g
Sodium Bisulfate	80 g
ADD Distilled water	1000 ml

Use three 1 liter (or larger) size clean glass or plastic bottles with leak-proof caps. Label them

Part A, **Part B**, and **Bleach** respectively. To help dissolve the chemicals, you can heat the water until it is lukewarm. Optionally, you can also prepare each solution in a clean beaker and then pour the solution into the bottle.

PART A. Fill the bottle marked Part A with roughly 1000 ml of warm distilled water. Dissolve each chemical above for Part A one-by-one, in any order. Tightly cap the bottle.

PART B. Follow a similar procedure as above for Part B.

BLEACH. Follow a similar procedure as above for the Bleach.

All solutions last for many months if capped tightly and stored in room temperature. Refrigeration will further increase shelf life, per phone conversation with manufacturers, \sim 6 months for Parts A and B ³, \sim 1 year for Bleach. We have a fridge in the darkroom for these. Store chemicals it in a safe place away from food and children.

A.2 Exposing the hologram

Use the Beseler 23CII enlarger without any lens at the necessary distance such that the power meter reads the values in the laboratory notebook. Set bottom of lens holder height at 20 cm from contact print surface. Place an OD 1 neutral density filter in the lens holder. Make sure the condenser lamp housing is all the way up and the extensible fabric is fully extended. In complete darkness, place

³Solutions A and B are bad when they turn yellowish.

the plate and film on top with the holders provided. Expose for ~ 1 min. Return to a light tight case for later development.

A.3 Developing the hologram

A.3.1 Preparation

Have the following items on hand:

- Your pre-mixed JD-2 Part A, Part B, and Bleach Solution.
- 1 additional gallon (4 liters) of distilled or de-ionized water for best results. Tap water will also work but not as well. Avoid hard water. This will be used to rinse the holograms between each processing step.
- 2 small glass or plastic trays, just large enough so that the hologram you are making can be submerged in a horizontal position.
- 2 large glass or plastic trays to hold 1 liter of distilled water for rinsing. Tap water may also work but not as well.
- 1 (optional, but recommended) large tray to hold 1 liter of distilled water mixed with about 1 ml of photographic wetting agent such as PhotoFlo or Formaflo. You can also use a small tray with less wetting agent, but you should replace the solution after a few holograms.
- 1 rubber glove

Now label one small tray as Developer A&B. Then, mix equal portions of Part A and Part B, enough so that the hologram to be developed can be totally submerged. Once mixed, the combined A&B solution can be used to develop several holograms, and can last several hours.

- Next to the developer tray place a large tray with one liter of distilled water. This will be used as a rinse.
- Next, label another small tray as Bleach. Put enough bleach into it so that the hologram can be totally submerged.
- Next to the bleach place another large tray with one liter of distilled water. This will be used as a rinse.



Figure A.1: Hologram processing chain with the JD-2 developer.

Optionally, place a large tray with the wetting solution in 1 liter of distilled water. Using a wetting solution is optional but recommended. It allows the hologram to dry evenly, thus helping you prevent smudges or streaks. Check the order of the trays: developer A&B, rinse, bleach, rinse, wetting solution.

A.3.2 Processing procedures

After the holographic plate is exposed, hold it by the edges with your glove hand (or tongs). Keep the emulsion (sticky) side facing upwards to protect the emulsion from accidentally scraping the bottom of your developer tray. Complete the following steps in a dark room. You can use the dark green safelight. After the bleaching process, it is safe to turn on all lights.

1. **Develop:** Quickly submerge the plate into the developer so that all parts get wet evenly. Slush it around for about two minutes. The hologram should turn black.
2. **Rinse:** Rinse the developed hologram with agitation for about 20 seconds (or up to three minutes for best results).
3. **Bleach:** Place the rinsed hologram into the bleaching solution; agitate it until the plate is completely clear (approximately two minutes or less).
4. **Rinse again:** Rinse the bleached hologram with agitation for about 20 seconds (or up to three minutes for best results)
5. **Finish in wetting solution:** Optionally, place the finished hologram in the wetting solution for about 20-60 seconds. For best results, avoid streaks or runs as you remove the hologram from the solution. You can actually do this step under light so you observe if the wetting solution is evenly coated. (After the bleaching process, the hologram is safe to process under regular indoor lighting).

A good way to dry the hologram is to stand it against a vertical surface with the bottom edge resting on a hand-towel or tissue paper. Best results are obtained when it dries naturally in clean,

dust-free air.

Transmission holograms can be viewed with a laser even when wet but the diffraction efficiency *will* differ from later tests when dry.

Appendix B

Beam pointing stabilization

The experiments described in this thesis involved fiber coupling down-converted photons at about 10 meters away from the pump laser cavity. Fluctuations and drift of the pump beam pointing affect the amplitude and polarization phase of the coupled state. The laser's built-in BeamLok system is insufficient, since it is specified to position offsets up to $0.5 \mu\text{m}/^\circ\text{C}$ and angular drifts up to $5 \mu\text{rad}/^\circ\text{C}$. This angular offset corresponds to $50 \mu\text{m}$ at the fiber location; moreover, it was actually measured to fluctuate within $\sim 18 \mu\text{rad}$ over a period of 4 hours (see Fig. B.2). The drift and fluctuations observed are described below with the current solutions.

1. Every time the laser is turned on, the pointing changes if the cavity knobs are adjusted to get lasing (not compensated by built-in BeamLok system). Solution: Once lasing is achieved and the laser BeamLok is enabled, use the cavity knobs (piezo mirrors) to realign the beam with the zero of the quad-segmented photodiodes for small (big) adjustments.
2. Once lasing is achieved and the BeamLok is enabled, the pointing fluctuates around a central position in a time scale of hours, and drifts away over a scale of 5 hours. Solution: beam pointing stabilization feedback setup (described below).

To compensate for lateral and angular displacements, we designed and constructed a beam-pointing stabilization system (later found to be similar to Ref. [129]) consisting of two units with the following elements (see Fig. B.1):

1. Quad segmented photodiodes (“quad-cells”). For our UV-laser, we chose quad-cells with quartz windows (“UV-enhanced” from UDT Sensors, Inc. model SPOT-4DUV) to improve the detection efficiency and increase their lifetime. The quad-cell was mounted on a sum/difference amplifier circuit (Pacific Silicon Sensors model QP50SD).
2. Feedback proportional-integral (PI) circuit, designed and built in-house (described below). The signal from the quad-cells was fed into this circuit, which controlled the mirrors on kinematic mounts.

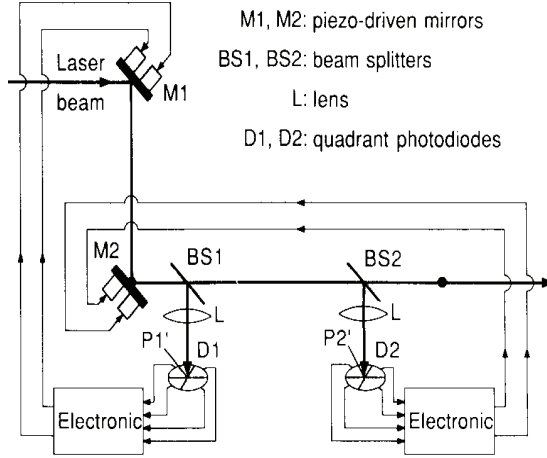


Figure B.1: Schematic of laser beam pointing control device (based on Fig. 1 of Ref. [129]).

3. Piezo-controlled kinematic mounts (Thorlabs model KC1-PZ) and voltage amplifier or controller (Thorlabs model MDT693A).

Beam size and power at the quad-cell was optimized for higher SNR and sensitivity as described in Ref. [129]. Figure B.2 illustrates the quality of the stabilization.

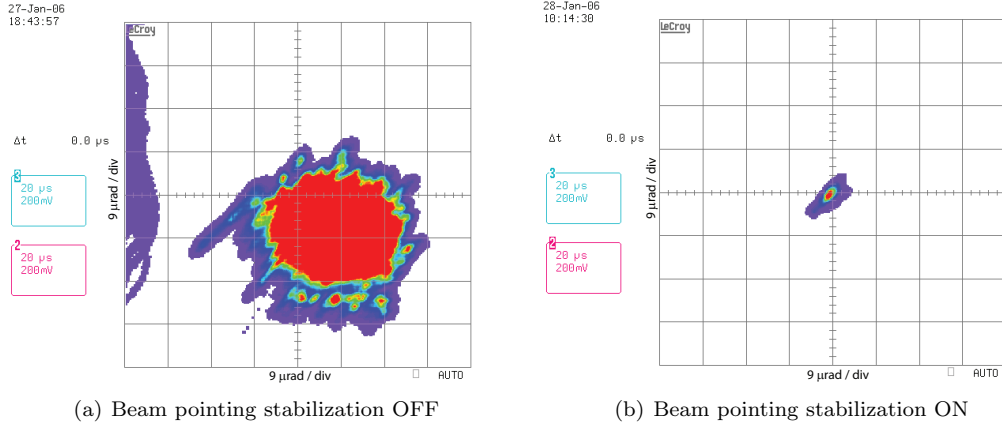


Figure B.2: Effect of beam pointing stabilization. Scope traces on persistent mode (4 hours) of the beam position at the last quad-cell. Residual purple trace on the far left is due to blocking/unblocking the beam. The diagonal trace on the right of $\sim 4 \mu\text{rad}$ is due to noise from the power supplies of the beam pointing circuit (power switchers Artesyn Model NLP40-7610, peak-to-peak ripple voltage $V_{\text{ripple}} \sim 150 \text{ mV}$ at 65(5) kHz). Currently we have power supplies with smaller amplitude voltage ripples (GW Instek GPS-4303, $V_{\text{ripple}} < 2 \text{ mV}$ at 5 Hz $\sim 1 \text{ MHz}$) giving a pointing stability $< 1 \mu\text{rad}$.

B.1 Feedback circuit

Figure B.3 shows the EAGLE schematic¹ of the feedback circuit. The input from the sensor is in the upper left. There are three power lines shared with the sensor board: +15 V, GND (ground), and -15 V. The power connector is right below the sensor connector, it powers the board and the photodiode.

The three signal lines from the sensor are $V_{\text{top-bottom}}$, $V_{\text{left-right}}$, and V_{sum} . These signals are amplified with an op-amp (OP27Z). This is particularly necessary when the signals are low. The amplifiers are all variable and can be adjusted with a potentiometer. A DC signal can be used to set all three amplifiers to the same value. During testing we found that a factor of about 10 was good with the UV laser. Both axes, top-bottom and left-right, are processed in the same way, as follows.

1. After amplification, the signal is normalized by the sum with an analog divider (Analog Devices model AD538AD). The output of the AD538 is equal to $10 * V_{\text{axis}} / V_{\text{sum}}$, and will always be in the range -10 V to 10 V. A value of 0 means that the laser is centered on the quad-cell.
2. The signal goes next into an analog integrator. The output is the error from 0 integrated over time and multiplied by the constant $1/RC$ which in this case is $1/10 k\Omega * 1\mu\text{F} = 100\text{Hz}$. This can be changed to make it more sensitive. Note that the integrator maximum is $\pm 14 \text{ V}$. This op-amp and three more are on the same chip (LM324N).
3. Next, the signal from the op-amp can be inverted. For example, for a positive error, the voltage on the piezo could be increased or decreased; if the latter, the signal must be inverted. This can be set with a switch located outside the box and currently labeled accordingly.
4. Two more op-amps will convert the signal to a range that can be given to the piezo controller as input. The first one scales the output of the integrator. This is set by allowing the integrator to accumulate to one extreme ($\pm 14 \text{ V}$, then scale the output to $\pm 10 \text{ V}$ with the potentiometer. The second op-amp averages the signal with a 10 V reference DC signal, making the output of the integrator go from a range of -10 V to 10 V to a range of 0-10 V, as required by the piezo controller. All four op-amps in steps 2-X are on the same chip (LM324N).
5. The final output is an analog signal in the range of 0-10 V moving to compensate the error from the quad-cell signal.

¹Eagle is a free software for the design of printed circuit boards (PCB): www.cadsoft.de .

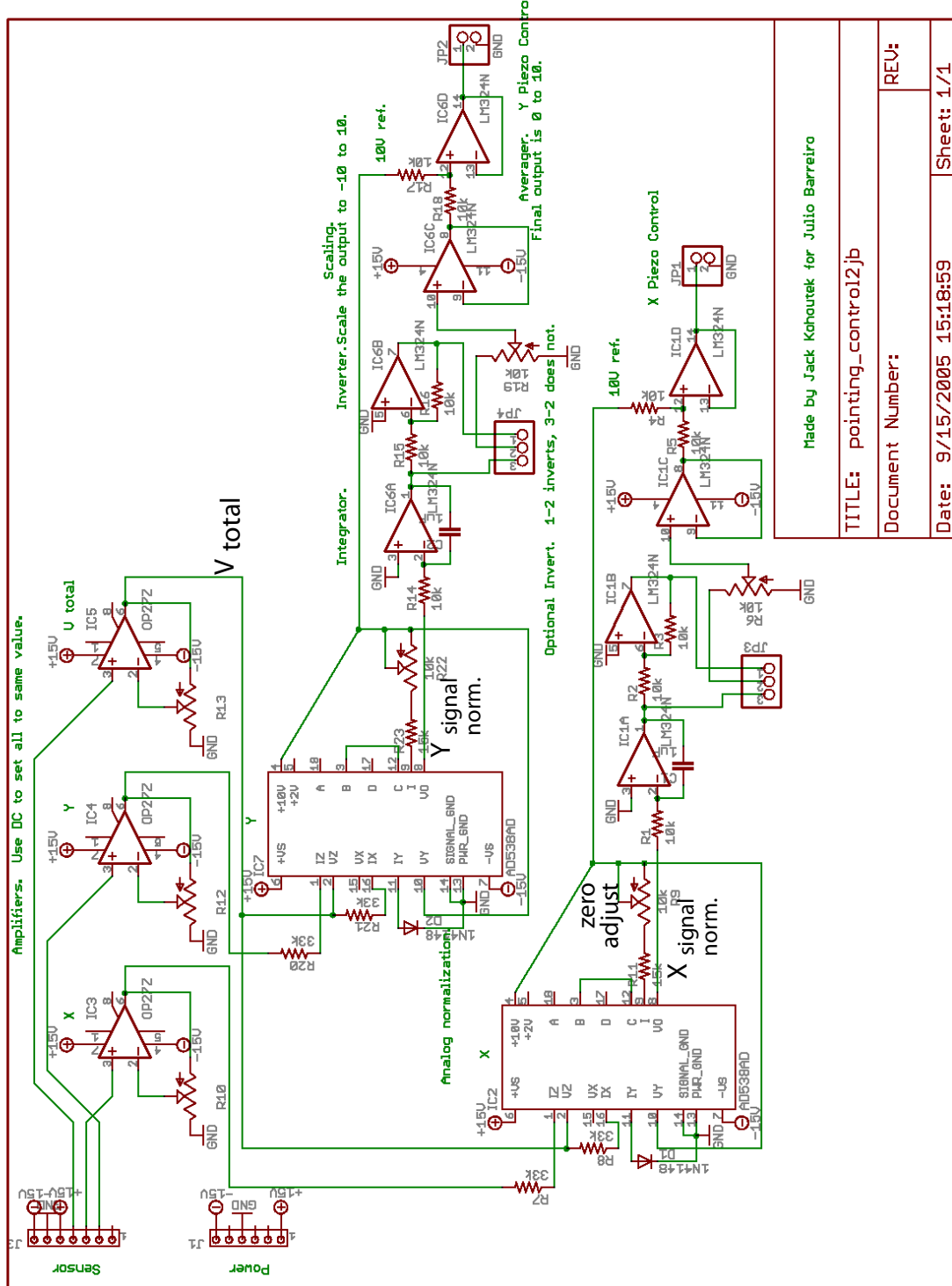


Figure B.3: Eagle schematic for the pointing stabilization circuit.

Appendix C

Hyperentanglement-assisted dense coding: Supplementary information

C.1 Channel capacity as a function of conditional detection average success probability

In Fig. 3.6, the CC upper bound for the 4-state encoding domain occurs when two of the four states are faithfully transmitted and the other two mixed, corresponding to a transfer matrix of conditional probabilities $p(y|x)$ of receiving the state y given that the state x was sent,

$$\begin{pmatrix} p(\Phi^+|\Phi^+) & p(\Phi^+|\Phi^-) & p(\Phi^+|\Psi^+) & p(\Phi^+|\Psi^-) \\ p(\Phi^-|\Phi^+) & p(\Phi^-|\Phi^-) & p(\Phi^-|\Psi^+) & p(\Phi^-|\Psi^-) \\ p(\Psi^+|\Phi^+) & p(\Psi^+|\Phi^-) & p(\Psi^+|\Psi^+) & p(\Psi^+|\Psi^-) \\ p(\Psi^-|\Phi^+) & p(\Psi^-|\Phi^-) & p(\Psi^-|\Psi^+) & p(\Psi^-|\Psi^-) \end{pmatrix} = \begin{pmatrix} 2p_s - 1 & 2(1-p_s) & 0 & 0 \\ 2(1-p_s) & 2p_s - 1 & 0 & 0 \\ 0 & 0 & 1 & 0 \\ 0 & 0 & 0 & 1 \end{pmatrix} \quad (\text{C.1})$$

with an input distribution $p(x)$ maximized for each conditional detection average success probability p_s . The lower bound is set by a uniform noise over the failed transmissions, resulting in a transfer matrix:

$$\begin{pmatrix} p_s & f & f & f \\ f & p_s & f & f \\ f & f & p_s & f \\ f & f & f & p_s \end{pmatrix}, \quad (\text{C.2})$$

where $f = (1-p_s)/3$ and the input distribution that maximizes the mutual information is $p(x) = 1/4$, i.e., all messages x are equally likely to be sent.

C.2 Effect of experimental imperfections on the channel capacity

In our scheme, the major detriments to the CC were the input polarization and spatial-mode states and the PBS crosstalk; accidental coincidences led to only a minor CC reduction. We model each imperfection as a function of relevant parameters, which were estimated by quantum state tomography or measured. Then we feed these parameters into a Monte Carlo simulation of the expected CC, as described below.

C.2.1 Modeling imperfections: The input states

The imperfections in the hyperentangled state generated by spontaneous parametric down-conversion, $|\Phi_{\text{spin}}^-\rangle \otimes |\Psi_{\text{orbit}}^+\rangle$ in our case, can be modeled with high fidelity by uniform-noise decoherence, a population imbalance angle ϵ_θ and a relative phase ϵ_ϕ . The deviations from the ideal pure state $|\Phi_{\text{spin}}^-\rangle \otimes |\Psi_{\text{orbit}}^+\rangle$ have the following form

$$|\Phi_{\text{spin}}^-(\epsilon_{\theta,\text{spin}}, \epsilon_{\phi,\text{spin}})\rangle = \cos(\pi/4 + \epsilon_{\theta,\text{spin}})|HH\rangle - e^{i\epsilon_{\phi,\text{spin}}} \sin(\pi/4 + \epsilon_{\theta,\text{spin}})|VV\rangle, \quad (\text{C.3})$$

$$|\Psi_{\text{orbit}}^+(\epsilon_{\theta,\text{orbit}}, \epsilon_{\phi,\text{orbit}})\rangle = \cos(\pi/4 + \epsilon_{\theta,\text{orbit}})|lr\rangle + e^{i\epsilon_{\phi,\text{orbit}}} \sin(\pi/4 + \epsilon_{\theta,\text{orbit}})|rl\rangle. \quad (\text{C.4})$$

The uniform-noise decoherence is characterized by a parameter λ and it adds mixture to each spin and orbital density matrices in the form $\rho(\lambda) = (1 - \lambda)\rho + \lambda\mathbf{I}_4$, where \mathbf{I}_4 is the 4-dimensional identity matrix. Since the imperfections also affect the messages encoded, the four states in the dense-coding protocol have a functional dependence on the source parameters ϵ_θ , ϵ_ϕ and λ :

$$\begin{aligned} &\Phi_{\text{spin}}^\pm(\epsilon_{\theta,\text{spin}}, \epsilon_{\phi,\text{spin}}, \lambda_{\text{spin}}) \otimes \Psi_{\text{orbit}}^+(\epsilon_{\theta,\text{orbit}}, \epsilon_{\phi,\text{orbit}}, \lambda_{\text{orbit}}) \\ &\Phi_{\text{spin}}^\pm(\epsilon_{\theta,\text{spin}}, \epsilon_{\phi,\text{spin}}, \lambda_{\text{spin}}) \otimes \Psi_{\text{orbit}}^+(\epsilon_{\theta,\text{orbit}}, \epsilon_{\phi,\text{orbit}}, \lambda_{\text{orbit}}). \end{aligned} \quad (\text{C.5})$$

Moreover, since these parameters vary slightly due to alignment¹ and component imperfections among the different combinations of signature detectors, we performed a quantum state tomography in each combination and determined the spread in the parameters. To estimate the CC, we performed

¹For example, the input polarization state phase ϕ depends on the collection angle [71], resulting in small but different phases for each coupling combination.

Monte Carlo simulations where the above parameters are the random variables following a normal distribution with a standard deviation given by the spread of the estimated parameters.

C.2.2 Modeling imperfections: The spin-orbit gate

The forked hologram maps the OAM states $|l\rangle$ and $|r\rangle$ into distinct propagation modes a and b with no OAM, respectively corresponding to the +1 and -1 diffraction orders (with a π phase shift difference):

$$\begin{pmatrix} |Hl\rangle \\ |Hr\rangle \\ |Vl\rangle \\ |Vr\rangle \end{pmatrix} \xrightarrow{\text{forked hologram}} \begin{pmatrix} |H_a\rangle \\ -|H_b\rangle \\ |V_a\rangle \\ -|V_b\rangle \end{pmatrix}. \quad (\text{C.6})$$

The PBS is modeled with a crosstalk parameter for each polarization, ϵ_H and ϵ_V , and a relative phase shift between H and V polarizations for each output mode, ϕ_1 and ϕ_2 . In the basis of Eq. C.6,

$$PBS(\epsilon_H, \epsilon_V, \phi_1, \phi_2) = \begin{pmatrix} \sqrt{1-\epsilon_H} & -\sqrt{\epsilon_H} & 0 & 0 \\ \sqrt{\epsilon_H} & \sqrt{1-\epsilon_H} & 0 & 0 \\ 0 & 0 & e^{\frac{1}{2}i(\phi_1+\phi_2)}\sqrt{\epsilon_V} & -e^{i\phi_2}\sqrt{1-\epsilon_V} \\ 0 & 0 & e^{i\phi_1}\sqrt{1-\epsilon_V} & e^{\frac{1}{2}i(\phi_1+\phi_2)}\sqrt{\epsilon_V} \end{pmatrix}. \quad (\text{C.7})$$

The phase shifts ϕ_1 and ϕ_2 were corrected with tilted birefringent plates (quarter-wave plates, in particular) with their optic axes aligned parallel to the direction of horizontal polarization. Therefore, for the model we can set $\phi_1 = \phi_2 = 0$, and the PBS depends only on the crosstalk, $PBS(\epsilon_H, \epsilon_V)$.

The gate for the pair of photons is therefore

$$U(\epsilon_H, \epsilon_V) = (PBS(\epsilon_H, \epsilon_V) \cdot \text{Hologram})_{\text{photon 1}} \otimes (PBS(\epsilon_H, \epsilon_V) \cdot \text{Hologram})_{\text{photon 2}}. \quad (\text{C.8})$$

C.2.3 Estimating the channel capacity

Using the above input states and spin-orbit gates we can estimate the conditional detection probabilities; for example, the probability of inferring Φ^+ given that Φ^- was sent is

$$p(\Phi^+|\Phi^-) = \langle \Phi_{\text{spin}}^+ \otimes \Psi_{\text{orbit}}^+ | U(\epsilon_H, \epsilon_V) \rho_{\Phi_{\text{spin}}^- \otimes \Psi_{\text{orbit}}^+} U(\epsilon_H, \epsilon_V)^\dagger | \Phi_{\text{spin}}^+ \otimes \Psi_{\text{orbit}}^+ \rangle, \quad (\text{C.9})$$

Table C.1: Effect of experimental imperfections on the CC.

Imperfection	Average success probability	Achievable CC (bits)	CC reduction (bits)
Source polarization state ^a $\epsilon_{\theta,\text{spin}} = 1.0(7)^\circ$, $\epsilon_{\phi,\text{spin}} = 0(4)^\circ$, $\lambda_{\text{spin}} = 0.010(2)$ $T = 96.7(8)\%$, $S_L = 2.0(4)\%$	0.991(2)	1.91(2)	0.09(2)
Source spatial-mode state ^a $\epsilon_{\theta,\text{orbit}} = 1.7(6)^\circ$, $\epsilon_{\phi,\text{orbit}} = 0(5)^\circ$, $\lambda_{\text{orbit}} = 0.03(1)$ $T = 91(3)\%$, $S_L = 6(2)\%$	0.971(4)	1.80(3)	0.20(3)
PBS crosstalk ^b $\epsilon_H = 0.005(1)$, $\epsilon_V = 0.010(2)$	0.985(2)	1.90(1)	0.10(2)
Accidentals (5 in 150s) ^c	0.998(1)	1.98(1)	0.02(1)
All the above imperfections in the same simulation	0.953(3)	1.64(2)	0.36(2)

where $\rho_{\Phi_{\text{spin}}^-\otimes\Psi_{\text{orbit}}^+}$ is a function of $\epsilon_{\theta,\text{spin}}$, $\epsilon_{\phi,\text{spin}}$, λ_{spin} , $\epsilon_{\theta,\text{orbit}}$, $\epsilon_{\phi,\text{orbit}}$ and λ_{orbit} . Finally, the CC is obtained by maximizing the mutual information over all the input distributions.

C.2.4 Results

We characterized the source polarization state Φ_{spin}^- by quantum state tomography in the $|lr\rangle$ and $|rr\rangle$ OAM subspaces [28]. Considering all combinations of signature detectors, we measured an average degree of entanglement or tangle of $T = 96.7(8)\%$ and a mixture or linear entropy of $S_L = 2.0(4)\%$. The OAM state was also tomographically reconstructed in the $|HH\rangle$ and $|VV\rangle$ polarization subspaces [28], measuring an average $T = 91(3)\%$ and $S_L = 6(2)\%$. We calculated the states of the form of Eq. C.3 and C.4 closest to the reconstructed density matrices. The fidelity between the reconstructed and closest estimated states is 99% for polarization and 97% for spatial-mode states. The estimated parameters and their spread are shown in the Table C.1. The achievable CC under only one imperfection is quoted as well (see also Fig. C.1). The Monte Carlo simulations used 100 iterations, enough to display stable values in the first digit of the uncertainty.

The subtle and convoluted character of the imperfections is evident upon directly adding the independently modeled CC reductions of each imperfection, which would predict an anomalously low CC=1.59 bits, compared to the full Monte-Carlo simulation resulting from simultaneously modeling all the effects, which predicts CC=1.64(2) bits.

Finally, we stress that the reported conditional distribution was *not* normalized by the statistical detection probabilities to account for detection imbalances over the different states. As these detection probabilities were well balanced in our case, only 3% off for the states Φ^- and Ψ^+ , such

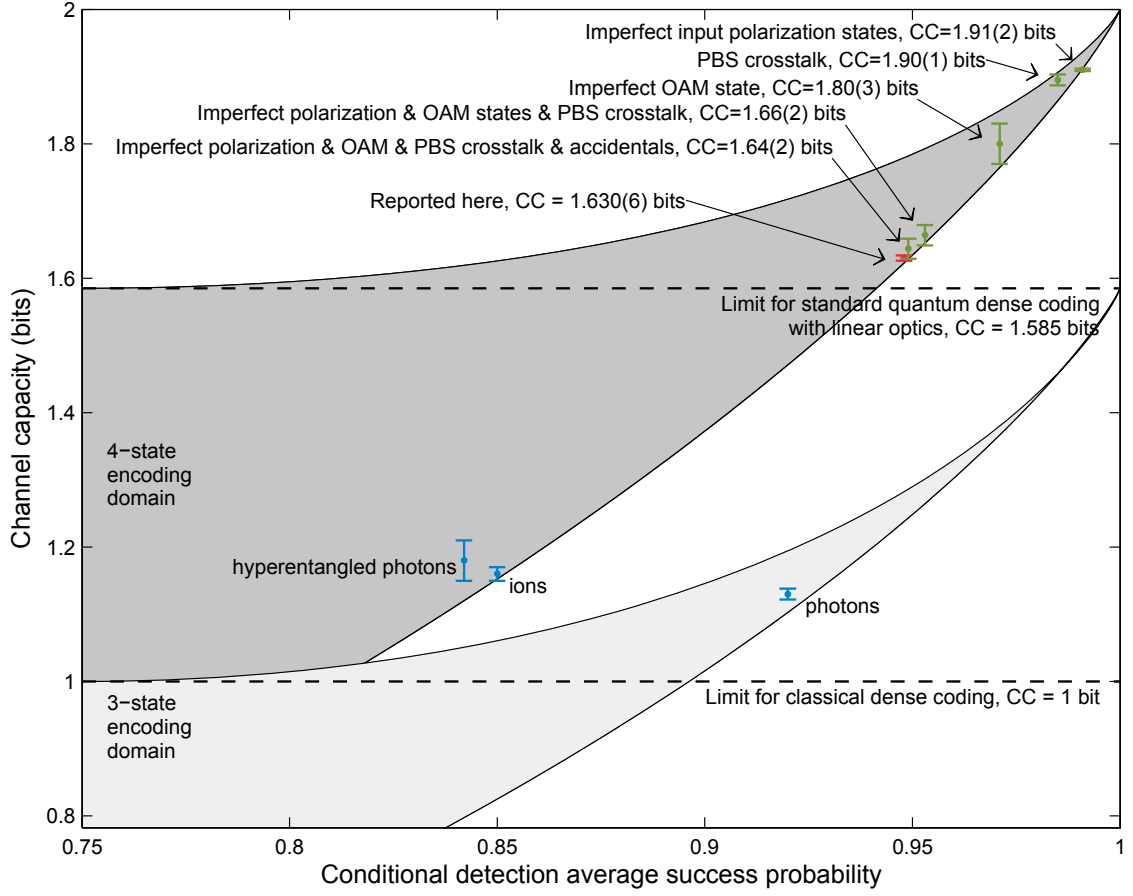


Figure C.1: Experimentally achieved and simulated CCs as a function of conditional detection average success probability. The simulated CC for our hyperentanglement-assisted dense-coding protocol, when affected by only the experimental imperfections indicated, are shown in green. The CC reported in the accompanying article is shown in red. Previously reported CCs are shown in blue for photons with [56] and without hyperentanglement [53] and for ions [66].

normalization would only slightly increase our reported CC to 1.634(6) bits.

Appendix D

Spin-orbit entangling gate

Some of the single-photon states entangled in the spatial modes $\text{HG}_{01/10}$ and polarization described in Chapter 5 can be produced with the gate shown in Fig. D.1. An input photon in the state

$$|\text{HG}_{01}^{\otimes 45^\circ}\rangle \otimes (\cos \theta |H\rangle + e^{i\phi} \sin \theta |V\rangle)$$

is sent into a Sagnac interferometer consisting of PBS and an embedded Dove Prism rotated at an angle of 22.5° with respect to the horizontal. A spatial mode $|\text{HG}_{01}^{\otimes 45^\circ}\rangle$ coming into the Dove prism from the left (right) in the polarization state $|V\rangle$ ($|H\rangle$) is rotated by 45° (-45°) to become $|\text{HG}_{10}\rangle$ ($|\text{HG}_{01}\rangle$). At the output of the interferometer the photon is in the tunable entangled state

$$\cos \theta |\text{HG}_{10}H\rangle + e^{i\phi} \sin \theta |\text{HG}_{01}V\rangle.$$

We setup this gate and characterized it with the input state $|\text{HG}_{01}^{\otimes 45^\circ}\rangle \otimes \frac{1}{\sqrt{2}}(|H\rangle + |V\rangle)$ (see Fig. D.1). This gate was also a test bed for the generation of the states entangled in the spatial modes $\text{HG}_{02/20}$ and polarization needed for bound entanglement (see Section 6.1).

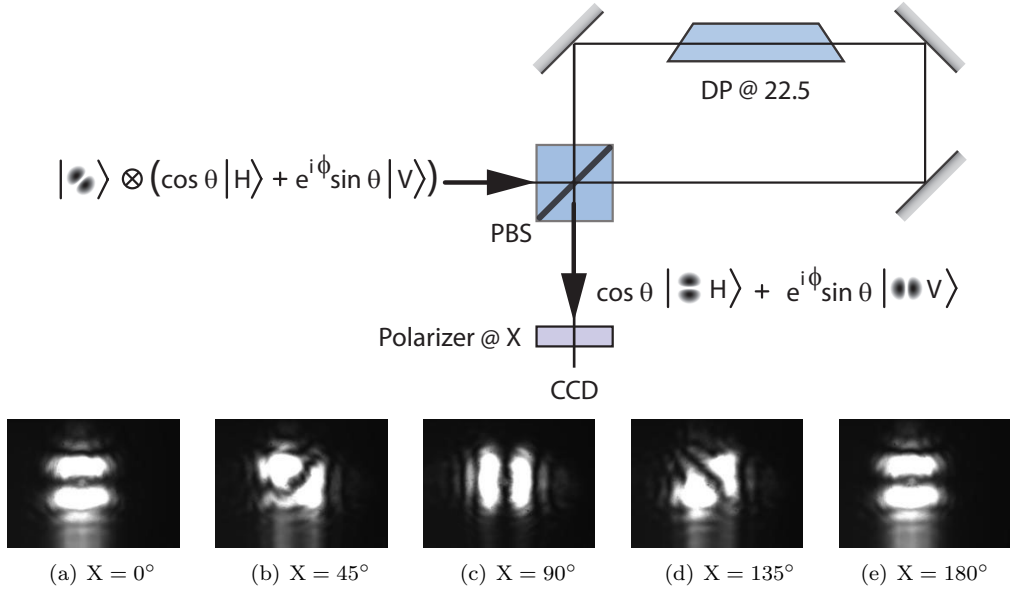


Figure D.1: Spin-orbit entangling gate and measured intensity profiles. Top: Scheme to controllably generate an entangled state of the polarization and spatial-mode of a single photon. The spatial mode states are represented by their transverse intensity profile, *e.g.*, the $|HG_{01}^{@45^\circ}\rangle$ input spatial mode. The input spatial mode was prepared with a binary phase grating as shown in Fig. 2.2. (a-e): Experimental intensity profiles measured with a charge-coupled device (CCD) after a polarizer at the indicated angle. The input beam was in the particular separable state ($\theta = 45^\circ, \phi = 0$) $|HG_{01}^{@45^\circ}\rangle \otimes \frac{1}{\sqrt{2}}(|H\rangle + |V\rangle)$. Notice how the orientation of the Hermite-Gauss profile follows the polarization angle, highlighting the entanglement between the spatial mode and the polarization. PBS: Polarizing beamsplitter, DP@22.5: Dove prism rotated at an angle of 22.5° from the horizontal.

Appendix E

Quantum state tomography for multidimensional and multiparticle quantum systems

We followed a procedure analogous to Ref. [43] for the reconstruction of density matrices, supplemented to handle arbitrary dimensions. Given a source that produces N particles in the same unknown state ρ from a space of dimensions $d_1 \otimes d_2 \otimes \cdots \otimes d_N$, we can experimentally reconstruct the state ρ by performing at least $d_1^2 \times d_2^2 \times \cdots \times d_N^2$ linearly independent measurements (including normalization).

As described in detail by James *et al.* [43], the statistics of the source (“noise”) can give unphysical density matrices if calculated from a linear transformation. This problem is avoided by estimating the density matrix with maximum likelihood techniques. The idea of such techniques is to parametrize the density matrix, and optimize the parameters to increase the likelihood that the estimated density matrix reproduces the measured data. However, a good initial guess must be provided to achieve fast convergence of the optimization routine¹. Such starting point is given by a linear reconstruction, described below.

E.1 Linear reconstruction

For the tomographic reconstruction, as in Ref. [43], assume that the set of projection measurements $\{|\psi_\nu\rangle\langle\psi_\nu|\}$ acts on the experimentally produced states and gives the measured counts n_ν . It is useful to consider a basis of the tensor product of generators of the special unitary group (SU), *i.e.*, $SU(d_1) \otimes SU(d_2) \otimes \cdots \otimes SU(d_N)$ with the following properties

$$\text{Tr} \left\{ \hat{\Gamma}_\nu \cdot \hat{\Gamma}_\mu \right\} = \delta_{\nu,\mu}$$

$$\hat{A} = \sum_{\nu=1}^D \hat{\Gamma}_\nu \left\{ \hat{\Gamma}_\nu \cdot \hat{A} \right\} \quad \forall \hat{A}$$

¹We use MATLAB’s optimization package: www.mathworks.com

where \hat{A} is an arbitrary $(d_1 \times d_2 \times \cdots \times d_N) \times (d_1 \times d_2 \times \cdots \times d_N)$ matrix, and $D = d_1^2 \times d_2^2 \times \cdots \times d_N^2$. This set can be constructed with the tensor product of the basis of $SU(d)$. The explicit construction of the basis of $SU(d)$ is shown in the MATLAB code in Section E.2.

Using this basis we can write the density matrix describing our states as:

$$\rho = \frac{1}{\mathcal{N}} \sum_{\nu=1}^D \hat{M}_\nu n_\nu$$

where \mathcal{N} is the source intensity and

$$\hat{M}_\nu = \sum_{\mu=1}^D (B^{-1})_{\nu,\mu} \hat{\Gamma}_\mu, \quad B_{\nu,\mu} = \langle \psi_\nu | \hat{\Gamma}_\mu | \psi_\nu \rangle.$$

E.2 MATLAB code to generate the traceless Hermitian basis of the special unitary group $SU(d)$

```

function ans = generatorsSU(d)
    % GENERATORSSU return an array of cell with the generators of SU(d)
    % GENERATORSSU(D)
    % D dimensions

    % off-diagonal generators
    for j = 2:1:d;
        for k = 1:1:j-1;
            i1 = (j-1)^2 + 2*(k-1);
            i2 = (j-1)^2 + 2*k - 1;
            ans {i1} = ejk(d,j,k) + ejk(d,k,j);
            ans {i2} = - i * (ejk(d,j,k) - ejk(d,k,j));
        end
    end

    % diagonal generators
    for j = 2:1:d
        i3 = j^2 - 1;

```

```

ans {i3} = etarr(d,j-1);

end

% identity matrix
ans{d^2} = eye(d);

function ans = ejk(d,j,k)
% EJK e_j^k elementary matrices of the SU(d) algebra
% EJK(D,J,K)
ans = zeros(d);
ans (k, j) = 1;

function ans = etarr(d,r)

ans = sqrt(2/(r*(r+1)));
tmp = zeros(d);
for j = 1:1:r
    tmp = tmp + ejk(d,j,j);
end
ans = ans * (tmp - r*ejk(d,r+1,r+1));

```

References

- [1] Bennett, C. H. & Brassard, G. Quantum cryptography: Public key distribution and coin tossing. In *Proc. of the IEEE Int. Conf. on Computers, Systems, and Signal Processing*, Proc. IEEE, 175 (New York, 1984).
- [2] Ekert, A. Quantum cryptography based on Bell's theorem. *Phys. Rev. Lett.* **67**, 661–663 (1991).
- [3] Shor, P. W. In *Proc. of the 35th annual symp. of Found. of Comp. Science*, 124–134 (1994).
- [4] Grover, L. K. Quantum mechanics helps in searching for a needle in a haystack. *Phys. Rev. Lett.* **79**, 325–328 (1997).
- [5] Grover, L. K. Quantum computers can search rapidly by using almost any transformation. *Phys. Rev. Lett.* **80**, 4329–4332 (1998).
- [6] Raussendorf, R. & Briegel, H. J. A one-way quantum computer. *Phys. Rev. Lett.* **86**, 5188–5191 (2001).
- [7] Walther, P. *et al.* Experimental one-way quantum computing. *Nature* **434**, 169–176 (2005).
- [8] Neumann, P. *et al.* Multipartite entanglement among single spins in diamond. *Science* **320**, 1326–1329 (2008).
- [9] Steffen, M. *et al.* Measurement of the entanglement of two superconducting qubits via state tomography. *Science* **313**, 1423–1425 (2006).
- [10] Blatt, R. & Wineland, D. Entangled states of trapped atomic ions. *Nature* **453**, 1008–1015 (2008).
- [11] Julsgaard, B., Kozhekin, A. & Polzik, E. S. Experimental long-lived entanglement of two macroscopic objects. *Nature* **413**, 400–403 (2001).
- [12] O'Brien, J. L. Optical quantum computing. *Science* **318**, 1567–1570 (2007).
- [13] Stevenson, R. M. *et al.* A semiconductor source of triggered entangled photon pairs. *Nature* **439**, 179–182 (2006).
- [14] Beugnon, J. *et al.* Quantum interference between two single photons emitted by independently trapped atoms. *Nature* **440**, 779–782 (2006).
- [15] Maunz, P. *et al.* Quantum interference of photon pairs from two remote trapped atomic ions. *Nature Physics* **3**, 538–541 (2007).
- [16] Lu, C.-Y. *et al.* Experimental entanglement of six photons in graph states. *Nature Physics* **3**, 91–95 (2007).
- [17] Ou, Z. Y. & Mandel, L. Violation of Bell's inequality and classical probability in a two-photon correlation experiment. *Phys. Rev. Lett.* **61**, 50–53 (1988).

- [18] Shih, Y. H. & Alley, C. O. New type of Einstein-Podolsky-Rosen-Bohm experiment using pairs of light quanta produced by optical parametric down conversion. *Phys. Rev. Lett.* **61**, 2921–2924 (1988).
- [19] Rarity, J. G. & Tapster, P. R. Experimental violation of Bell's inequality based on phase and momentum. *Phys. Rev. Lett.* **64**, 2495–2498 (1990).
- [20] Mair, A., Vaziri, A., Weihs, G. & Zeilinger, A. Entanglement of the orbital angular momentum states of photons. *Nature* **412**, 313–316 (2001).
- [21] Langford, N. K. *et al.* Measuring entangled qutrits and their use for quantum bit commitment. *Phys. Rev. Lett.* **93**, 53601 (2004).
- [22] Franson, J. D. Bell inequality for position and time. *Phys. Rev. Lett.* **62**, 2205–2208 (1989).
- [23] Brendel, J., Gisin, N., Tittel, W. & Zbinden, H. Pulsed energy-time entangled twin-photon source for quantum communication. *Phys. Rev. Lett.* **82**, 2594–2597 (1999).
- [24] Strekalov, D. V., Pitman, T. B., Sergienko, A. V., Shih, Y. H. & Kwiat, P. G. Postselection-free energy-time entanglement. *Phys. Rev. A* **54**, R1–R4 (1996).
- [25] Cinelli, C., Barbieri, M., Perris, R., Mataloni, P. & Martini, F. D. All-versus-nothing non-locality test of quantum mechanics by two-photon hyperentanglement. *Phys. Rev. Lett.* **95**, 240405 (2005).
- [26] Yang, T. *et al.* All-versus-nothing violation of local realism by two-photon, four-dimensional entanglement. *Phys. Rev. Lett.* **95**, 240406 (2005).
- [27] Kwiat, P. G. Hyper-entangled states. *J. Mod. Opt.* **44**, 2173–2184 (1997).
- [28] Barreiro, J. T., Langford, N. K., Peters, N. A. & Kwiat, P. G. Generation of hyperentangled photon pairs. *Phys. Rev. Lett.* **95**, 260501 (2005).
- [29] Cerf, N. J., Adami, C. & Kwiat, P. G. Optical simulation of quantum logic. *Phys. Rev. A* **57**, R1477–R1480 (1998).
- [30] Vallone, G., Pomarico, E., Mataloni, P., Martini, F. D. & Berardi, V. Realization and characterization of a two-photon four-qubit linear cluster state. *Phys. Rev. Lett.* **98**, 180502 (2007).
- [31] Vallone, G., Pomarico, E., Martini, F. D. & Mataloni, P. Active one-way quantum computation with two-photon four-qubit cluster states. *Phys. Rev. Lett.* **100**, 160502 (2008).
- [32] Boyd, R. W. *Nonlinear optics* (Academic Press, San Diego, 2003).
- [33] Burnham, D. C. & Weinberg, D. L. Observation of simultaneity in parametric production of optical photon pairs. *Phys. Rev. Lett.* **25**, 84–87 (1970).
- [34] Kwiat, P. G., Waks, E., White, A. G., Appelbaum, I. & Eberhard, P. H. Ultrabright source of polarization-entangled photons. *Phys. Rev. A* **60**, R773–R776 (1999).
- [35] Walborn, S. P., de Oliveira, A. N., Thebaldi, R. S. & Monken, C. H. Entanglement and conservation of orbital angular momentum in spontaneous parametric down-conversion. *Phys. Rev. A* **69**, 023811 (2004).
- [36] Walborn, S. P., Pádua, S. & Monken, C. H. Conservation and entanglement of Hermite-Gaussian modes in parametric down-conversion. *Phys. Rev. A* **71**, 053812 (2005).
- [37] Torres, J. P., Deyanova, Y., Torner, L. & Molina-Terriza, G. Preparation of engineered two-photon entangled states for multidimensional quantum information. *Phys. Rev. A* **67**, 052313 (2003).

- [38] Torres, J. P., Alexandrescu, A. & Torner, L. Quantum spiral bandwidth of entangled two-photon states. *Phys. Rev. A* **68**, 50301 (2003).
- [39] Allen, L., Barnett, S. M. & Padgett, M. J. (eds.) *Optical Angular Momentum* (Institute of Physics Publishing, Bristol, 2003).
- [40] Molina-Terriza, G., Torres, J. P. & Torner, L. Management of the angular momentum of light: Preparation of photons in multidimensional vector states of angular momentum. *Phys. Rev. Lett.* **88**, 13601 (2002).
- [41] Eisenberg, H. S., Khoury, G., Durkin, G. A., Simon, C. & Bouwmeester, D. Quantum entanglement of a large number of photons. *Phys. Rev. Lett.* **93**, 193901 (2004).
- [42] Wootters, W. K. Entanglement of formation of an arbitrary state of two qubits. *Phys. Rev. Lett.* **80**, 2245–2248 (1998).
- [43] James, D. F. V. *et al.* Measurement of qubits. *Phys. Rev. A* **64**, 052312 (2001).
- [44] Clauser, J. F., Horne, M. A., Shimony, A. & Holt, R. A. Proposed experiment to test local hidden-variable theories. *Phys. Rev. Lett.* **23**, 880–884 (1969). Erratum is just an acknowledgement update.
- [45] Terhal, B. M. Bell inequalities and the separability criterion. *Phys. Lett. A* **271**, 319–326 (2000).
- [46] Zyczkowski, K., Horodecki, P., Sanpera, A. & Lewenstein, M. Volume of the set of separable states. *Phys. Rev. A* **58**, 883–892 (1998).
- [47] White, A. G., James, D. F. V., Munro, W. J. & Kwiat, P. G. Exploring Hilbert space: accurate characterization of quantum information. *Phys. Rev. A* **65**, 12301 (2002).
- [48] Kwiat, P. G. & Weinfurter, H. Embedded Bell-state analysis. *Phys. Rev. A* **58**, R2623–R2626 (1998).
- [49] Bennett, C. H. & Wiesner, S. J. Communication via one- and two-particle operators on Einstein-Podolsky-Rosen states. *Phys. Rev. Lett.* **69**, 2881–2884 (1992).
- [50] Wang, C., Deng, F.-G., Li, Y.-S., Liu, X.-S. & Long, G. L. Quantum secure direct communication with high-dimension quantum superdense coding. *Phys. Rev. A* **71**, 044305 (2005).
- [51] Thew, R. T., Ací, A., Zbinden, H. & Gisin, N. Bell-type test of energy-time entangled qudits. *Phys. Rev. Lett.* **93**, 10503 (2004).
- [52] O’Sullivan-Hale, M. N., Khan, I. A., Boyd, R. W. & Howell, J. C. Pixel entanglement: Experimental realization of optically entangled d=3 and d=6 qudits. *Phys. Rev. Lett.* **94**, 220501 (2005).
- [53] Mattle, K. *et al.* Dense coding in experimental quantum communication. *Phys. Rev. Lett.* **76**, 4656–4659 (1996).
- [54] Vaidman, L. & Yoran, N. Methods for reliable teleportation. *Phys. Rev. A* **59**, 116–125 (1999).
- [55] Lütkenhaus, N., Calsamiglia, J. & Suominen, K. A. Bell measurements for teleportation. *Phys. Rev. A* **59**, 3295–3300 (1999).
- [56] Schuck, C., Huber, G., Kurtsiefer, C. & Weinfurter, H. Complete deterministic linear optics Bell state analysis. *Phys. Rev. Lett.* **96**, 190501 (2006).
- [57] Barbieri, M., Vallone, G., Mataloni, P. & Martini, F. D. Complete and deterministic discrimination of polarization Bell states assisted by momentum entanglement. *Phys. Rev. A* **75**, 042317 (2007).

- [58] Molina-Terriza, G., Torres, J. P. & Torner, L. Twisted photons. *Nature Physics* **3**, 305–310 (2007).
- [59] Aolita, L. & Walborn, S. P. Quantum communication without alignment using multiple-qubit single-photon states. *Phys. Rev. Lett.* **98**, 100501 (2007).
- [60] Liu, X. S., Long, G. L., Tong, D. M. & Li, F. General scheme for superdense coding between multiparties. *Phys. Rev. A* **65**, 022304 (2002).
- [61] Harrow, A., Hayden, P. & Leung, D. Superdense coding of quantum states. *Phys. Rev. Lett.* **92**, 187901 (2004).
- [62] Braunstein, S. L. & Kimble, H. J. Dense coding for continuous variables. *Phys. Rev. A* **61**, 042302 (2000).
- [63] Ban, M. Quantum dense coding via a two-mode squeezed-vacuum state. *J. Opt. B: Quantum Semiclass. Opt.* **1**, L9 (1999).
- [64] Li, X. *et al.* Quantum dense coding exploiting a bright Einstein-Podolsky-Rosen beam. *Phys. Rev. Lett.* **88**, 047904 (2002).
- [65] Fang, X., Zhu, X., Feng, M., M, X. & Du, F. Experimental implementation of dense coding using nuclear magnetic resonance. *Phys. Rev. A* **61**, 022307 (2000).
- [66] Schaetz, T. *et al.* Quantum dense coding with atomic qubits. *Phys. Rev. Lett.* **93**, 040505 (2004).
- [67] Kim, Y.-H., Kulik, S. P. & Shih, Y. Quantum teleportation of a polarization state with a complete Bell state measurement. *Phys. Rev. Lett.* **86**, 1370–1373 (2001).
- [68] Calsamiglia, J. & Lutkenhaus, N. Maximum efficiency of a linear-optical Bell-state analyzer. *Appl. Phys. B: Lasers Opt.* **B72**, 67–71 (1999).
- [69] Walborn, S. P., Pádua, S. & Monken, C. H. Hyperentanglement-assisted Bell-state analysis. *Phys. Rev. A* **68**, 042313 (2003).
- [70] Englert, B.-G., Kurtsiefer, C. & Weinfurter, H. Universal unitary gate for single-photon two-qubit states. *Phys. Rev. A* **63**, 032303 (2001).
- [71] Altepeter, J. B., Jeffrey, E. R. & Kwiat, P. G. Phase-compensated ultra-bright source of entangled photons. *Opt. Express* **13**, 8951–8959 (2005).
- [72] Wei, T.-C., Barreiro, J. T. & Kwiat, P. G. Hyperentangled Bell-state analysis. *Phys. Rev. A* **75**, 060305(R) (2007).
- [73] Fiorentino, M. & Wong, F. N. C. Deterministic controlled-not gate for single-photon two-qubit quantum logic. *Phys. Rev. Lett.* **93**, 070502 (2004).
- [74] Ali-Khan, I., Broadbent, C. J. & Howell, J. C. Large-alphabet quantum key distribution using energy-time entangled bipartite states. *Phys. Rev. Lett.* **98**, 060503 (2007).
- [75] Paterson, C. Atmospheric turbulence and orbital angular momentum of single photons for optical communication. *Phys. Rev. Lett.* **94**, 153901 (2005).
- [76] Smith, B. J. & Raymer, M. G. Two-photon wave mechanics. *Phys. Rev. A* **74**, 062104 (2006).
- [77] Nielsen, M. A. & Chuang, I. L. *Quantum Computation and Quantum Information* (Cambridge University Press, Cambridge, 2000), 1st edn.
- [78] Bennett, C. H. *et al.* Teleporting an unknown quantum state via dual classical and einstein-podolsky-rosen channels. *Phys. Rev. Lett.* **70**, 1895–1899 (1993).

- [79] Bouwmeester, D. *et al.* Experimental quantum teleportation. *Nature* **390**, 575–579 (1997).
- [80] Boschi, D. *et al.* Experimental realization of teleporting an unknown pure quantum state via dual classical and einstein-podolsky-rosen channels. *Phys. Rev. Lett.* **80**, 1121–1125 (1998).
- [81] Buhrman, H., Cleve, R., Watrous, J. & de Wolf, R. Quantum fingerprinting. *Phys. Rev. Lett.* **87**, 167902 (2001).
- [82] Horn, R. T., Babichev, S. A., Marzlin, K.-P., Lvovsky, A. I. & Sanders, B. C. Single-qubit optical quantum fingerprinting. *Phys. Rev. Lett.* **95**, 150502 (2005).
- [83] Mohseni, M. & Lidar, D. A. Direct characterization of quantum dynamics. *Phys. Rev. Lett.* **97**, 170501 (2006).
- [84] Calsamiglia, J. Generalized measurements by linear elements. *Phys. Rev. A* **65**, 030301(R) (2002).
- [85] van Houwelingen, J. A. W., Brunner, N., Beveratos, A., Zbinden, H. & Gisin, N. Quantum teleportation with a three-bell-state analyzer. *Phys. Rev. Lett.* **96**, 130502 (2006).
- [86] Ursin, R. *et al.* Communications: Quantum teleportation across the danube. *Nature* **430**, 849 (2004).
- [87] Walborn, S. P., Nogueira, W. A. T., Pádua, S. & Monken, C. H. Optical Bell-state analysis in the coincidence basis. *Europhys. Lett.* **62**, 161–167 (2003).
- [88] Ren, X.-F., Guo, G.-P. & Guo, G.-C. Complete Bell-states analysis using hyper-entanglement. *Phys. Lett. A* **343**, 8–11 (2005).
- [89] Barreiro, J. T., Wei, T.-C. & Kwiat, P. G. Beating the channel capacity limit for linear photonic superdense coding. *Nature Physics* **4**, 282–286 (2008).
- [90] Ekert, A. & Knight, P. L. Entangled quantum systems and the schmidt decomposition. *Am. J. Phys.* **63**, 415–423 (1995).
- [91] van Loock, P. & Ltkenhaus, N. Simple criteria for the implementation of projective measurements with linear optics. *Phys. Rev. A* **69**, 012302 (2004).
- [92] Ghosh, S., Kar, G., Roy, A. & Sarkar, D. Distinguishability of maximally entangled states. *Phys. Rev. A* **70**, 022304 (2004).
- [93] Wei, T.-C. Private communication.
- [94] Eisert, J. Optimizing linear optics quantum gates. *Phys. Rev. Lett.* **95**, 040502 (2005).
- [95] Lo, H.-K. Classical-communication cost in distributed quantum-information processing: A generalization of quantum-communication complexity. *Phys. Rev. A* **62**, 012313 (2000).
- [96] Pati, A. K. Minimum classical bit for remote preparation and measurement of a qubit. *Phys. Rev. A* **63**, 014302 (2000).
- [97] Bennett, C. H. *et al.* Remote state preparation. *Phys. Rev. Lett.* **87**, 077902 (2001).
- [98] Peters, N. A., Barreiro, J. T., Goggin, M. E., Wei, T.-C. & Kwiat, P. G. Remote state preparation: arbitrary remote control of photon polarization. *Phys. Rev. Lett.* **94**, 150502 (2005).
- [99] Bužek, V., Hillery, M. & Werner, R. F. Optimal manipulations with qubits: Universal-not gate. *Phys. Rev. A* **60**, R2626–R2629 (1999).

- [100] Yang, T. *et al.* Experimental synchronization of independent entangled photon sources. *Phys. Rev. Lett.* **96**, 110501 (2006).
- [101] Berglund, A. J. Quantum coherence an control in one- and two-photon optical systems. arXiv:quant-ph/0010001 (2000).
- [102] Tidwell, S. C., Ford, D. H. & Kimura, W. D. Generating radially polarized beams interferometrically. *Appl. Optics* **29**, 2234–2239 (1990).
- [103] Edighoffer, J. A., Kimura, W. D., Pantell, R. H., Piestrup, M. A. & Wang, D. Y. Observation of inverse Cerenkov interaction between free electrons and laser light. *Phys. Rev. A* **23**, 1848–1854 (1980).
- [104] Dorn, R., Quabis, S. & Leuchs, G. Sharper focus for a radially polarized light beam. *Phys. Rev. Lett.* **91**, 233901 (2003).
- [105] Urbach, H. P. & Pereira, S. F. Field in focus with a maximum longitudinal electric component. *Phys. Rev. Lett.* **100**, 123904 (2008).
- [106] Sondermann, M. *et al.* Design of a mode converter for efficient light-atom coupling in free space. *Appl. Phys. B: Lasers Opt.* **89**, 489–492 (2007).
- [107] Lindlein, N. *et al.* A new 4π geometry optimized for focusing on an atom with a dipole-like radiation pattern. *Laser Physics* **17**, 927–934 (2007).
- [108] Bennett, C. H. *et al.* Purification of noisy entanglement and faithful teleportation via noisy channels. *Phys. Rev. Lett.* **76**, 722–725 (1996).
- [109] Kwiat, P. G., Barraza-Lopez, S., Stefanov, A. & Gisin, N. Experimental entanglement distillation and 'hidden' non-locality. *Nature* **409**, 1014–1017 (2001).
- [110] Horodecki, M., Horodecki, P. & Horodecki, R. Mixed-state entanglement and distillation: Is there a "bound" entanglement in nature? *Phys. Rev. Lett.* **80**, 5239–5242 (1998).
- [111] Murao, M. & Vedral, V. Remote information concentration using a bound entangled state. *Phys. Rev. Lett.* **86**, 352–355 (2001).
- [112] Horodecki, K., Horodecki, M., Horodecki, P. & Oppenheim, J. Secure key from bound entanglement. *Phys. Rev. Lett.* **94**, 160502 (2005).
- [113] Horodecki, P., Horodecki, M. & Horodecki, R. Bound entanglement can be activated. *Phys. Rev. Lett.* **82**, 1056–1059 (1999).
- [114] Augusiak, R. & Horodecki, P. Generalized Smolin states and their properties. *Phys. Rev. A* **73**, 012318 (2006).
- [115] Horodecki, M., Horodecki, P. & Horodecki, R. Separability of mixed states: necessary and sufficient conditions. *Phys. Lett. A* **223**, 1–8 (1996).
- [116] Smolin, J. A. Four-party unlockable bound entangled state. *Phys. Rev. A* **63**, 032306 (2001).
- [117] Kwiat, P. G., Berglund, A. J., Altepeter, J. B. & White, A. G. Experimental verification of decoherence-free subspaces. *Science* **290**, 498–501 (2000).
- [118] Wei, T.-C., Altepeter, J. B., Goldbart, P. M. & Munro, W. J. Measures of entanglement in multipartite bound entangled states. *Phys. Rev. A* **70**, 022322 (2004).
- [119] Hillery, M., Buzek, V. & Berthiaume, A. Quantum secret sharing. *Phys. Rev. A* **59**, 1829–1834 (1999).

- [120] Gisin, N. Hidden quantum nonlocality revealed by local filters. *Phys. Lett. A* **210**, 151–156 (1996).
- [121] Schmid, C. *et al.* Experimental single qubit quantum secret sharing. *Phys. Rev. Lett.* **95**, 230505 (2005).
- [122] Chen, Y.-A. Experimental quantum secret sharing and third-man quantum cryptography. *Phys. Rev. Lett.* **95**, 200502 (2005).
- [123] Augusiak, R. & Horodecki, P. Bound entanglement maximally violating bell inequalities: Quantum entanglement is not fully equivalent to cryptographic security. *Phys. Rev. A* **74**, 010305 (2006).
- [124] Brukner, C., Zukowski, M., Pan, J.-W. & Zeilinger, A. Bell's inequalities and quantum communication complexity. *Phys. Rev. Lett.* **92**, 127901 (2004).
- [125] Collins, D., Gisin, N., Linden, N., Massar, S. & Popescu, S. Bell inequalities for arbitrarily high-dimensional systems. *Phys. Rev. Lett.* **88**, 040404 (2002).
- [126] Acín, A., Durt, T., Gisin, N. & Latorre, J. I. Quantum nonlocality in two three-level systems. *Phys. Rev. A* **65**, 052325 (2002).
- [127] Hariharan, P. *Optical Holography* (Cambridge University Press, 1996).
- [128] Vaziri, A., Weihs, G. & Zeilinger, A. Superpositions of the orbital angular momentum for applications in quantum experiments. *J. Opt. B: Quantum Semiclass. Opt.* **4**, S47–S51 (2002). [Http://stacks.iop.org/1464-4266/4/S47](http://stacks.iop.org/1464-4266/4/S47).
- [129] Grafströma, S., Harbarth, U., Kowalskia, J., Neumann, R. & Noehtea, S. Fast laser beam position control with submicroradian precision. *Opt. Comm.* **65**, 121–126 (1988).

Author's Biography

Julio T. Barreiro-Guerrero was born in México City to parents Julieta Guerrero Colin and Tomás Barreiro Chacón.

Awards and honors

Donald and Shirley Jones Fellowship (Research Excellence)	2008
Mavis Memorial Fund Award for (Teaching Excellence)	2007
Mexican National Council for Science and Technology Fellowship	2001-2006
Fulbright Scholar, US	2001-2004
“Gabino Barreda” medal, highest GPA Computer Science, UNAM	2000
“Gabino Barreda” medal, highest GPA Physics, UNAM	1998
CERN summer student	1998

Publications

- [1] Barreiro, J. T., Wei, T.-C. & Kwiat, P. G. Remote preparation of single-photon entangled and radial polarization states. In preparation (2008).
- [2] Barreiro, J. T. & Kwiat, P. G. Hyperentanglement for advanced quantum communication. *Proc. SPIE*, In press (2008).
- [3] Barreiro, J. T., Wei, T.-C. & Kwiat, P. G. Beating the channel capacity limit for linear photonic superdense coding (Corrigendum). *Nature Physics*, **4**, 662 (2008).
- [4] Barreiro, J. T., Wei, T.-C. & Kwiat, P. G. Beating the channel capacity limit for linear photonic superdense coding. *Nature Physics*, **4**, 282–286 (2008).
- [5] Wei, T.-C., Barreiro, J. T. & Kwiat, P. G. Hyperentangled Bell-state analysis. *Phys. Rev. A*, **75**, 060305(R) (2007).

- [6] Hosten, O., Rakher, M. T., Barreiro, J. T., Peters, N. A. & Kwiat, P. G. Counterfactual computation revisited. Preprint quant-ph/0607101v2 (2006).
- [7] Hosten, O., Rakher, M. T., Barreiro, J. T., Peters, N. A. & Kwiat, P. G. Counterfactual quantum computation through quantum interrogation. *Nature*, **439**, 949–952 (2006).
- [8] Peters, N. A., Arnold, K. J., VanDevender, A. P., Jeffrey, E. R., Rangarajan, R., Hosten, O., Barreiro, J. T., Altepeter, J. B. & Kwiat, P. G. Towards a quasi-deterministic single-photon source. *Proc. SPIE*, **6305**, 630507 (2006).
- [9] Barreiro, J. T., Langford, N. K., Peters, N. A. & Kwiat, P. G. Generation of hyperentangled photon pairs. *Phys. Rev. Lett.*, **95**, 260501 (2005).
- [10] Peters, N. A., Barreiro, J. T., Goggin, M. E., Wei, T.-C. & Kwiat, P. G. Remote state preparation: arbitrary remote control of photon polarization. *Phys. Rev. Lett.*, **94**, 150502 (2005).
- [11] Peters, N. A., Barreiro, J. T., Goggin, M. E., Wei, T.-C. & Kwiat, P. G. Remote state preparation: arbitrary remote control of photon polarizations for quantum communication. *Proc. SPIE*, **5893**, 589308 (2005).
- [12] Ericsson, M., Achilles, D., Barreiro, J. T., Branning, D., Peters, N. A. & Kwiat, P. G. Measurement of geometric phase for mixed states using single photon interferometry. *Phys. Rev. Lett.*, **94**, 050401 (2005).
- [13] Kwiat, P. G., Altepeter, J. B., Barreiro, J. T., Goggin, M. E., Jeffrey, E., Peters, N. A. & VanDevender, A. The conversion revolution: Down, up and sideways. *AIP Conf. Proc.*, **734**, 337–341 (2004).
- [14] Ericsson, M., Achilles, D., Barreiro, J. T., Branning, D., Peters, N. A. & Kwiat, P. G. Geometric phase for mixed states using single-photon interferometry. *AIP Conf. Proc.*, **734**, 370–373 (2004).
- [15] Kwiat, P. G., Altepeter, J., Barreiro, J. T., Branning, D. A., Jeffrey, E. R., Peters, N. & VanDevender, A. P. Optical technologies for quantum information science. *Proc. SPIE*, **5161**, 87–100 (2004).
- [16] Ayala, A., Barreiro, J. & Montano, L. M. Density and expansion effects on pion spectra in relativistic heavy-ion collisions. *Phys. Rev. C*, **60**, 014904 (1999).